

2007

Kinematically designed flexible skins for morphing aircraft

Christine Marie Pastor
University of Dayton

Follow this and additional works at: https://ecommons.udayton.edu/graduate_theses

Recommended Citation

Pastor, Christine Marie, "Kinematically designed flexible skins for morphing aircraft" (2007). *Graduate Theses and Dissertations*. 4858.
https://ecommons.udayton.edu/graduate_theses/4858

This Thesis is brought to you for free and open access by the Theses and Dissertations at eCommons. It has been accepted for inclusion in Graduate Theses and Dissertations by an authorized administrator of eCommons. For more information, please contact mschlangen1@udayton.edu, ecommons@udayton.edu.

Kinematically Designed Flexible Skins
for Morphing Aircraft

Thesis

Submitted to

The School of Engineering of the
UNIVERSITY OF DAYTON

in Partial Fulfillment of the Requirements for

The Degree

Master of Science in Aerospace Engineering

by

Christine Marie Pastor

UNIVERSITY OF DAYTON

Dayton, Ohio

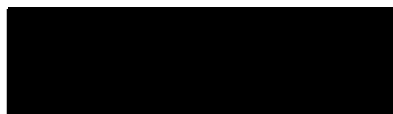
May, 2007

KINEMATICALLY DESIGNED FLEXIBLE SKINS FOR MORPHING AIRCRAFT


APPROVED BY:



Brian Sanders, Ph.D.
Advisory Committee Chairman
Adjunct Professor, Mechanical and
Aerospace Engineering Department



Margaret Pinnell, Ph.D.
Committee member
Assistant Professor, Mechanical
and Aerospace Engineering
Department



Geoff Frank, Ph.D.
Committee member
University of Dayton Research Institute



Donald L. Moon, Ph.D.
Associate Dean
Graduate Engineering Programs &
Research School of Engineering



Joseph E. Saliba, Ph.D., P.E.
Dean, School of Engineering

ABSTRACT

Kinematically Designed Flexible Skins for Morphing Aircraft

Name: Pastor, Christine Marie

University of Dayton, 2007

Advisor: Brian Sanders, Ph.D.

Advisory Committee Chairman

Adjunct Professor, Mechanical and

Aerospace Engineering Department

This investigation targeted the development of flexible materials that, when combined with mechanized structures, can enable large rigid body deformations of aircraft structures while maintaining its aerodynamic shape. The work focused on maximizing in-plane deformation and minimizing in-plane force required to deform the material, while minimizing the out-of-plane deflection. The matrix material selected to complete this research was a representative thermally activated Shape Memory Polymer (SMP), which was embedded with a reinforcing fiber. The fiber plays a dual role; in addition to serving as a reinforcing element it also provides the means to activate the material response via resistive heating. Several resistive heating element candidates were examined and an in depth heat transfer analysis and experiments were conducted to understand power requirements and minimum

spacing of the resistive element to activate the desired material response. Both the analysis and experiments illustrated that a carbon fiber tow was the most effective resistive heating element based on power required and area affected. A two layer structural skin solution is investigated that consisted of a smooth continuous layer and a cellular structure. The cellular structure to improve out-of-plane stiffness was modeled and tested for verification. Fiber tows are integrated into this skin design and experimentally tested. The cellular structure had a minimal effect on the amount of force needed to deform the material in-plane. This solution seems to be a reasonable approach and it meets some of the basic multifunctional skin criteria.

Acknowledgements

First I would like to thank and acknowledge Dr. Brian Sanders who took the leap of faith and took me on as his master's student. Second, I would like to thank Dr. Aaron Altman whom recommended that leap. These two men are the greatest advisors anyone could ask for and I am truly blessed to have had them help me along the path, encouraging me in the pursuit of my dreams.

Additionally, I would like to thank Robin McCarty whom provided great thermodynamic and heat transfer assistance as well as superb moral support; Mr. Brian Smyers who provided the use of his lab and vast experimentation knowledge; Dr. Jennifer Chase-Fielding and Dr. Jeff Bauer who both shared their wealth of materials knowledge; and Dr. David Phillips and Lt. Gabe Jacobs who provided invaluable assistance while making test specimens.

I would also like to thank my family. My father, Joseph J Pastor, who always encouraged me to follow my dreams by showing and teaching me about engineering before I even knew it exist; my mother, Janet Pastor, whom provided me with the motivation, and my brother, Joseph R Pastor, whom always reminded me to keep a sense of humor about life.

Also, I would like to thank my urban family, including but not solely, Mandy Brogdon, Kim Wilhelm, and Marina Stanbery, without whom I would not be the person I am today; the 2004 – 2005 UD SAE Aircraft Design team who taught me

that what I do can be fun; and to Diana Barga and Maria Saliba who helped me to remember during my master's research that life is more than just work.

Contents

Chapter	
1	Introduction 1
2	Background 6
2.1	Historical Skin Concepts 6
2.1.1	Sliding Skin 6
2.1.2	Elastomers 8
2.1.3	Shape Memory Polymers 11
2.2	Structural Concepts 16
2.2.1	Origins of sandwich construction 18
2.2.2	Uses of sandwich construction 19
2.3	Chapter Summary 20
3	Conceptual Designs 21
3.1	Functional Requirements 21
3.2	Design Requirements 21
3.3	Design Criteria 21
3.4	Concepts 23
3.5	Decision Analysis 27
3.6	Chapter Summary 27

4	Activation Strategy	28
4.1	Shape Memory Polymer (SMP)	29
4.1.1	Processing of SMP	30
4.1.2	Dynamic Mechanical Analysis Testing	35
4.2	Thermal Activation Method	37
4.2.1	Nanotubes	38
4.2.2	Embedded Wires	39
4.2.3	Finite Difference Comparison to Thermal Imaging	52
4.3	Chapter Summary	52
5	Structural Skin Concept	54
5.1	Description and characteristics of sandwich	54
5.2	Mechanics of cellular structures	56
5.3	In-Plane Stiffness Model	59
5.4	Specimen Design, Processing, and Testing	63
5.4.1	Test Specimen Design	63
5.4.2	Experimental Setup	67
5.4.3	Results	70
5.5	Chapter Summary	76
6	Summary and Conclusions	77
6.1	Thesis Summary	77
6.2	Future Work	78

Bibliography	80
Appendix	
A DMA Test Data	85
B Finite Difference Figures	88
C Thermal Imaging Results	95
C.1 Infrared Images	95
C.2 Time versus Temperature	102
C.3 Line Profile Plots	109
D Structural Skin Concept	113
D.1 In-Plane Stiffness Model Plots	113
D.2 Tensile Test Data	119

Figures

Figure

1.1	Coefficient of Drag vs Mach Number [1]	2
1.2	Spider Plot Showing Aerodynamic Effectiveness in Different Flight Regimes [5]	4
2.1	(a) MAW in Flight, (b) Structure of the MAW [2]	7
2.2	Diagram of the SAMPSON Inlet Geometry Control [3]	8
2.3	(a)Picture of conformal control surface without elastomer skin (b)Drawing of cross section of Smart Wing construction with skin	9
2.4	(a)Vehicle mounted in the Wind Tunnel (b)conformal control surface	10
2.5	(a) Out-of-Plane Morphing aircraft concept, (b) In-Plane Morphing aircraft concept	11
2.6	Modulus versus Strain Trade Space for Existing Materials [10]	12
2.7	Diagram of the SMP Thermo-Mechanical Cycle	14
2.8	26AWG (left) and 36AWG (right)	15
2.9	SMP auxetic cellular structure in neat resin and with carbon [16]	17
2.10	SMP auxetic effect [11]	17
3.1	Flying Dragon [19]	23
3.2	Earthworm concept	24

3.3	Half Baby Gate Mechanism Concept	25
3.4	(a)Kinematic Chain reinforcement mechanism (b)Carbon Fiber integrated shear concept	25
3.5	(a)Generic SMP layer concept (b)SMP layer concept with Arches . .	26
4.1	Mold Release being Applied to an Exterior Glass Plate	31
4.2	Assembled Mold	32
4.3	Pouring the Resin into the Mold	33
4.4	DMA test machine	36
4.5	Representative DMA Test Results	37
4.6	Rvol test setup (a) Rtt Test Setup (b)	39
4.7	Infrared Carbon Fiber Test Specimen	40
4.8	Infrared Nichrome wire Test Specimen	41
4.9	Infrared SMA Test Specimen	41
4.10	Infrared Imaging Test Setup	43
4.11	Infrared Imaging Test Specimen in Clamps	43
4.12	Infrared Image for the Carbon Fiber Specimen Resistively heated with 0.5 Amps	44
4.13	Carbon Fiber 0.5 Amp Line Profile Comparison Plot	45
4.14	Carbon Fiber 0.5 Amp Maximum Data Point Time versus Temperature Plot	46
4.15	Diagram of the Finite Difference model	48
4.16	Representative Finite Difference Result; Carbon Fiber at 0.5 Amps 32 Ω /m for 300 seconds in Celsius	51
4.17	Surface Finite Difference Result; Carbon Fiber at 0.5 Amps 32 Ω /m for 300 seconds in Celsius	51

4.18 Comparison of Surface Temperature Distributions; Carbon Fiber at 0.5 Amps $32\Omega/\text{m}$ for 300 seconds in Celsius	53
5.1 Cross Section of (a) Sandwich construction and (b) Monocoque con- struction	55
5.2 Diagram of the Undeformed Honeycomb	57
5.3 Plot of E1 and E2 for In-plane stiffness versus angle	57
5.4 Plot of E1 and E2 for In-plane stiffness versus cell wall thickness . .	58
5.5 Plot of E1 and E2 for In-plane stiffness versus cell wall length	58
5.6 Plot of the 1/4 inch hexagonal cell with 1/8 inch cell walls In-Plane Stiffness versus Cell Angle	61
5.7 Plot of the 1/4 inch hexagonal cell In-Plane Stiffness versus Cell Wall Thickness	61
5.8 Plot of the 1/4 inch hexagonal cell Length Change versus Cell Angle Change	62
5.9 Diagram of the 1/4 inch hexagonal cells with 1/8 inch walls Tensile Specimen	64
5.10 Printed template of the 1/4 inch cell with 1/8 inch walls Tensile Spec- imen	64
5.11 Carbon hex mold under construction	65
5.12 Carbon hex mold with Carbon Fiber tow weaved into the mold	66
5.13 Neat resin 1/4 inch hex with 1/8 inch cell walls	67
5.14 Carbon Fiber resistive heating elements woven into resin with 1/4 inch hex with 1/8 cell walls	68
5.15 Tensile Test Setup	69

5.16 Part 2 Stress versus Strain Response of Neat Resin Test Specimen	
above T_g	70
5.17 Tensile Test Data of the Neat Resin Specimen	71
5.18 Neat Resin Test Specimen with Experimental and Analytical Data	
Points	72
5.19 Neat Resin Test Specimen Post-Test	72
5.20 Carbon Fiber Heating Element Tensile Test Specimen Post-Test . . .	73
5.21 Part 3 Stress versus Strain Response of Carbon Fiber Test Specimen	
above T_g	74
5.22 Carbon Fiber Test Specimen Experiment Data Points	75
A.1 Test specimen <i>SMP072905</i> – 2 – 6x6x0.125 – <i>DMA1</i>	85
A.2 Test specimen <i>SMP072905</i> – 2 – 6x6x0.125 – <i>DMA2</i>	86
A.3 Test specimen <i>SMP072905</i> – 2 – 6x6x0.125 – <i>DMA3</i>	86
A.4 Test specimen <i>SMP080505</i> – 2 – 6x6x0.125 – <i>DMA1</i>	87
A.5 Test specimen <i>SMP080505</i> – 2 – 6x6x0.125 – <i>DMA2</i>	87
B.1 Carbon Fiber at 0.4Amps 32 Ω /m for 300 seconds	88
B.2 Carbon Fiber at 0.5Amps 32 Ω /m for 30 seconds	88
B.3 Carbon Fiber at 0.5Amps 32 Ω /m for 60 seconds	89
B.4 Carbon Fiber at 0.5Amps 32 Ω /m for 90 seconds	89
B.5 Carbon Fiber at 0.5Amps 32 Ω /m for 120 seconds	89
B.6 Carbon Fiber at 0.5Amps 32 Ω /m for 150 seconds	90
B.7 Carbon Fiber at 0.5Amps 32 Ω /m for 180 seconds	90
B.8 Carbon Fiber at 0.5Amps 32 Ω /m for 210 seconds	90
B.9 Carbon Fiber at 0.5Amps 32 Ω /m for 240 seconds	91
B.10 Carbon Fiber at 0.5Amps 32 Ω /m for 270 seconds	91

B.11 Carbon Fiber at 0.5 <i>Amps</i> 32 Ω / <i>m</i> for 300 seconds	91
B.12 Carbon Fiber at 0.6 <i>Amps</i> 32 Ω / <i>m</i> for 300 seconds	92
B.13 Carbon Fiber at 0.7 <i>Amps</i> 32 Ω / <i>m</i> for 300 seconds	92
B.14 Nichrome wire at 1.4 <i>Amps</i> 27.95 Ω / <i>m</i> for 300 seconds	92
B.15 Nichrome wire at 1.845 <i>Amps</i> 27.95 Ω / <i>m</i> for 300 seconds	93
B.16 Carbon Fiber at 1.885 <i>Amps</i> 27.95 Ω / <i>m</i> for 300 seconds	93
B.17 Carbon Fiber at 2.255 <i>Amps</i> 27.95 Ω / <i>m</i> for 300 seconds	93
B.18 SMA wire at 0.55 <i>Amps</i> 94.4 Ω / <i>m</i> for 300 seconds	94
B.19 SMA wire at 1.165 <i>Amps</i> 94.4 Ω / <i>m</i> for 300 seconds	94
C.1 Test 3 Short Carbon 1 0.5 <i>Amps</i>	95
C.2 Test 4 Short Carbon 1 0.4 <i>Amps</i>	96
C.3 Test 5 Short Carbon 1 0.6 <i>Amps</i>	96
C.4 Test 6 Short Carbon 1 0.7 <i>Amps</i>	97
C.5 Test1 SMA3 2 <i>Volts</i>	97
C.6 Test1 SMA3 2.3 <i>Volts</i>	98
C.7 Test1 SMA3 2.5 <i>Volts</i>	98
C.8 Test1 SMA3 2.7 <i>Volts</i>	99
C.9 Test1 Nichrome Specimen 2 2.0 <i>Volts</i>	99
C.10 Test3 Nichrome Specimen 2 2.3 <i>Volts</i>	100
C.11 Test2 Nichrome Specimen 2 2.5 <i>Volts</i>	100
C.12 Test4 Nichrome Specimen 2 2.7 <i>Volts</i>	101
C.13 Test 4 Short Carbon 1 0.4 <i>Amps</i> Average Temperature Plot	102
C.14 Test 4 Short Carbon 1 0.4 <i>Amps</i> Maximum Temperature Plot	102
C.15 Test 5 Short Carbon 1 0.6 <i>Amps</i> Average Temperature Plot	103
C.16 Test 5 Short Carbon 1 0.6 <i>Amps</i> Maximum Temperature Plot	103

C.17 Test 6 Short Carbon 1 0.7Amps Average Temperature Plot	104
C.18 Test 6 Short Carbon 1 0.7Amps Maximum Temperature Plot	104
C.19 Nichrome 2 2.0Volts Average Temperature Plot	105
C.20 Nichrome 2 2.0Volts Maximum Temperature Plot	105
C.21 Nichrome 2 2.3Volts Average Temperature Plot	106
C.22 Nichrome 2 2.3Volts Maximum Temperature Plot	106
C.23 Nichrome 2 2.5Volts Average Temperature Plot	107
C.24 Nichrome 2 2.5Volts Maximum Temperature Plot	107
C.25 Nichrome 2 2.7Volts Average Temperature Plot	108
C.26 Nichrome 2 2.7Volts Maximum Temperature Plot	108
C.27 Test 4 Short Carbon 1 0.4Amps Line Profile Plot	109
C.28 Test 5 Short Carbon 1 0.6Amps Line Profile Plot	109
C.29 Test 6 Short Carbon 1 0.7Amps Line Profile Plot	110
C.30 Nichrome 2 2.0volts Line Profile Plot	110
C.31 Nichrome 2 2.3volts Line Profile Plot	111
C.32 Nichrome 2 2.5volts Line Profile Plot	111
C.33 Nichrome 2 2.7volts Line Profile Plot	112
D.1 Plot of the 1/4 hexagonal cell with 1/8 cell walls In-Plane Stiffness versus Cell Angle	113
D.2 Plot of the 1/4 hexagonal cell with 1/4 cell walls In-Plane Stiffness versus Cell Angle	114
D.3 Plot of the 1/4 hexagonal cell with 3/8 cell walls In-Plane Stiffness versus Cell Angle	114
D.4 Plot of the 1/4 hexagonal cell In-Plane Stiffness versus Cell Wall Thickness	115

D.5	Plot of the 1/4 hexagonal cell Length Change versus Cell Angle Change	115
D.6	Plot of the 1/2 hexagonal cell with 1/8 cell walls In-Plane Stiffness versus Cell Angle	116
D.7	Plot of the 1/2 hexagonal cell with 1/4 cell walls In-Plane Stiffness versus Cell Angle	116
D.8	Plot of the 1/2 hexagonal cell with 3/8 cell walls In-Plane Stiffness versus Cell Angle	117
D.9	Plot of the 1/2 hexagonal cell In-Plane Stiffness versus Cell Wall Thickness	117
D.10	Plot of the 1/2 hexagonal cell Length Change versus Cell Angle Change	118
D.11	Part 1 Stress versus Strain Plot of Neat Resin Test Specimen at Room Temperature	119
D.12	Part 2 Stress versus Strain Plot of Neat Resin Test Specimen above Glass Transition Temperature	119
D.13	Part 3 Stress versus Strain Plot of Neat Resin Test Specimen above Glass Transition Temperature	120
D.14	Part 4 Stress versus Strain Plot of Neat Resin Test Specimen at Room Temperature	120
D.15	Part 1 Stress versus Strain Plot of Carbon Fiber Test Specimen at Room Temperature	121
D.16	Part 2 Stress versus Strain Plot of Carbon Fiber Test Specimen above Glass Transition Temperature	121
D.17	Part 3 Stress versus Strain Plot of Carbon Fiber Test Specimen above Glass Transition Temperature	122

Tables

Table

2.1	Basic Material Properties of an SMP	15
3.1	Decision Analysis	27
4.1	Veriflex®manufacturer cure cycle	33
4.2	Veriflex®extended cure cycle	34
4.3	DMA Tests	36
4.4	Rvol and Rtt Test Results	39
4.5	Selected Hexcel Magnamite AS4 Carbon Fiber Properties	41
4.6	Dynalloy Flexinol®Manufacturer given Properties [1]	42
4.7	Predetermined Fiber or Wire resistances and currents	50

Chapter 1

Introduction

Nature utilizes shape change to adapt to ever changing environments. Both birds and sea creatures alter their shape to change from cruise to attack conditions. Birds extend their wings to loiter in the sky and sweep them back to dash while catching food. Sea creatures deform their bodies to provide propulsion. In each case, this requires a combination of mechanized structures, actuators and flexible skins. For example, birds cover their underlying bone structure during shape change with layers of feathers, while fish employ systems of scales to provide external protection.

When aircraft originally came into existence over a hundred years ago, the Wright brothers, inspired by nature, utilized a flight control system called wing warping on their Wright Flyer. Wing warping changed the shape of the wing, allowing for in-flight roll control of the aircraft. However, as airplane performance and speed increased, the structure had to be built stronger and more rigid otherwise the aircraft could not withstand the increasing velocities and in-flight loads. Wing twist as the Wright brothers implemented it was no longer a viable option, thereby creating the requirement for today's stiffer conventional control surfaces, known as ailerons, flaps, rudder and elevator.

These are all examples of small rigid body motions. In the interest of increasing performance capabilities, large rigid body motions such as the swing wing

were developed. The swept configuration of the swing wing was utilized at higher speeds, increasing aircraft control and performance, while the un-swept or straight configuration of the swing wing was employed at lower speeds, providing an increase in endurance and range.

Aircraft such as the F-14, F-111, and the B-1 utilize variable sweep wings. Swing wings are extended for operation in lower subsonic flight regimes and swept back for operation in dash and upper regimes of subsonic and supersonic flight. It is known that as air passes over a straight wing, the chord of the wing is perpendicular to the freestream where there is a large drag rise as the aircraft approaches Mach 1. Therefore, as a wing is swept the freestream airflow sees the airfoil as nearly a third thinner, thereby increasing the critical Mach number (M_{crit}) and reducing drag (D) [2]. Figure 1.1 shows the reduction in the coefficient of drag (C_D) as the wing sweep (Λ) increases and the Mach number (M) increases.

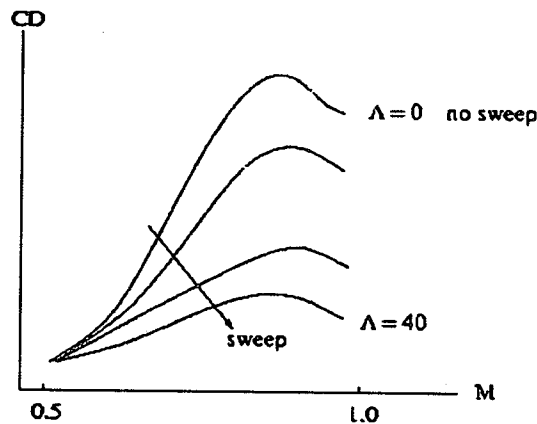


Figure 1.1: Coefficient of Drag vs Mach Number [1]

This capacity of aerodynamic improvement led to new ideas for shape change which provide even greater design efficiency and performance. Computer controlled camber, developed as part of the Mission Adaptive Wing (MAW) program,

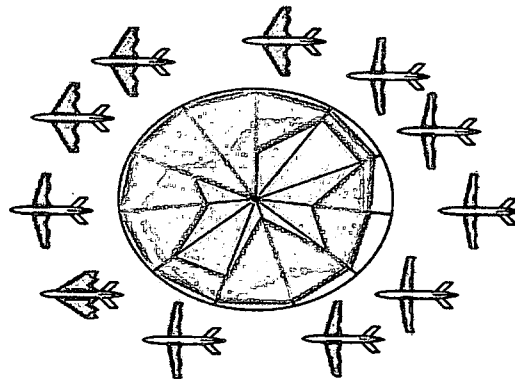
improved the aerodynamic efficiency of the F-111 via trailing and leading edge variable camber devices, which were covered with a flexible sliding fiberglass skin [3]. The fiberglass skin was required to allow for a smooth camber change of control surfaces. This program utilized computer controlled leading and trailing edge control surfaces on a wing to manipulate and optimize the camber of the wing. This provided, among other things, optimum lift-to-drag ratio (L/D) across the subsonic, transonic, and supersonic flight regimes.

Two programs, which utilized shape change enabled by a mechanized structural design and an elastomeric skin were the Smart Aircraft and Marine Project System demonstration (SAMPSON) and the Smart Wing program. The SAMPSON project utilized a smart inlet for a jet engine to optimize engine performance over different flight conditions. At low freestream velocities blunt inlet lips are more aerodynamically efficient, and at higher velocities sharper inlet lips produce less drag. To take advantage of aerodynamic efficiencies in both regimes, inlet lip shape change was enabled by a Shape Memory Alloy wire (SMA) with an elastomeric flexskin as the lip [4].

The Smart Wing program developed seamless conformal control surfaces, which improved the aeroelastic and aerodynamic performance [5]. This design enabled a continuous spanwise and chordwise distribution of pressure reducing premature flow separation. The conformal control surfaces were made with a honeycomb structure, rigid rod, and a flexible skin.

Morphing is the revolutionary next step in aircraft design, greatly increasing operational efficiency and allowing for effective operation at all points in the flight envelope. To understand the operational flight envelope more effectively, Figure 1.2 shows a spider plot detailing aerodynamic effectiveness at different configurations [6]. Each point on the circle represents a different facet of flight, i.e. takeoff,

landing, cruise. In Figure 1.2, the least efficient aircraft configuration is a fixed wing design shown as the smallest plot in pink. By sweeping the wing, the performance across the spectrum improves and is shown as the medium coverage plot in green within Figure 1.2. A notional morphing conceptual design illustrates how large changes in area can enable a robust performing vehicle over a broad range of flight conditions as detailed in Figure 1.2 using the largest plot in teal. Bowman, et. al. [7] have shown similar performance benefits for notional morphing aircraft.



© NextGen Aeronautics

Figure 1.2: Spider Plot Showing Aerodynamic Effectiveness in Different Flight Regimes [5]

Figure 1.2 demonstrates that continuous shape changes via large smooth rigid body motions are desired. An aerodynamic benefit of active shape change allows an aircraft to perform optimally at more than one regime in the flight envelope. Improvements in fuel efficiencies, loiter and dash capabilities, all within the same airframe, are some of the potential gains that could be acquired by active shape change. However, active shape change necessitates several pieces of technology. Required technologies include a mechanized wing structure, high powered actuators providing the appropriate movement while overcoming the aerodynamic loads

to deform the wing structure, and an aerodynamic surface, i.e. a flexible skin. The flexible skin is desired to supply minimal opposition to the required motion of the structure while withstanding the loads of the aerodynamic flight envelope.

Current materials technology provides the capacity for a material that would complete the full deformation with the structure, but would not be able to transfer the aerodynamic loads to the underlying wing structure. Some of these current skin solutions are scales, sliding panels, and elastomers. All of these solutions are effective in small deformation applications. For large deformations, with minimal pillowing of the skin, a new engineered material is required.

It is possible to combine two or more materials with different properties, that has been designed for a particular use to get an engineered composite material. An engineered composite utilizing a smart material such as Shape Memory Polymer (SMP), a controllable stiffness material, would make capable a large strain with a low modulus to enable in-plane deformation with minimal power. The SMP at low modulus requires reinforcement to minimize out-of-plane deflection.

In this research effort, the design of a flexible skin concept is proposed, and the basic design parameters are investigated. The research focused on minimizing the in-plane force required to achieve a target in-plane deformation while minimizing out-of-plane deflection. This concept will be examined utilizing a controllable stiffness material combined with a mechanized structure to enable large in-plane deformations with minimal out-of-plane deformations. The solution is based on a cellular structure design with a controllable stiffness material. Methods for activating the material are investigated via thermal imaging and finite difference analysis via a dual role fiber. A structural skin sandwich construction was evaluated utilizing the mechanics of honeycombs, the multi-functional fiber, and tensile testing.

Chapter 2

Background

This chapter discusses the previous research regarding flexible skin materials. A review of previous skin concepts including sliding skins, elastomers, and shape memory polymers is conducted. Additionally, structural skin concepts such as auxetic materials and tendon-actuated compliant cellular trusses are discussed. Prior research demonstrates the importance of a flexible skin, which has been emphasized continuously in recent attempts at structural control. The research reviewed here provided guidance throughout this project, in terms of concepts and ideas that were feasible to pursue within the allotted time frame and requirements as discussed in the next chapter.

2.1 Historical Skin Concepts

2.1.1 Sliding Skin

A nature inspired shape changing skin concept is sliding scales, i.e. fish scales. An early program that developed a sliding, flexible skin material was the Mission Adaptive Wing (MAW), completed in the early 1980s [3]. Figure 2.1(a) shows the MAW camber control deflected in flight. The system was controlled via a flight computer that utilized data from wind tunnel testing to determine optimal camber position. A schematic of the structure, which was required to complete

The control surfaces of the wing were covered with a fiberglass skin, which through bending of the skin and smoothly shaped control surfaces, enabled smoothly deforming skins in the chordwise direction. On the lower side, the skin was allowed to slide to prevent any local buckling; therefore, the skin is more accurately described as a flexible sliding skin. The skin completed small scale deformations and proved that bending deformation was possible with current day technology. This concept was applicable to minimize the weight and increase the wingloading of a given wing structure [3].

7

2.1.2 Elastomers

Another material that enables shape change that was utilized in previous research is an elastomer. An elastomer is defined as, "...a large class of polymers that can be stretched at room temperature to at least twice their original length and, after having been stretched and the stress removed, return with force to approximately their original length in a short time [8]." Therefore, the elastomer provides a large deformation with no permanent warping to the material itself. However, the large drawback to the elastomer is that to maintain the large deformation once it is induced requires a large amount of force, due to a build up of strain.

A recent attempt at using elastomers for controlled deformation was within the Smart Aircraft and Marine Project System demonstratiON (SAMPSON). The SAMPSON project investigated control of inlet geometry on jet engines [4]. The concept was to design a smart inlet that would change shape to optimize engine performance throughout a flight regime, as shown in Figure 2.2.

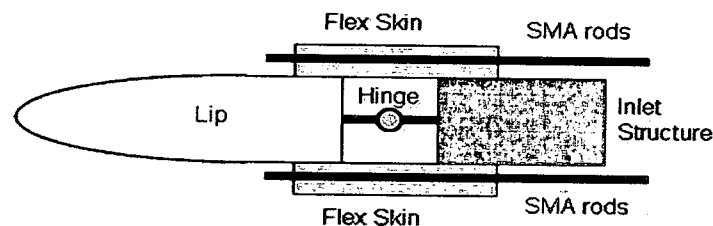


Figure 2.2: Diagram of the SAMPSON Inlet Geometry Control [3]

A reinforced elastomeric structure, called flexskin, was utilized as the deformable part of the structure by means of shape memory alloy (SMA) rods acting as the control mechanism. It was hoped that the construction method utilizing smart materials would avoid high life cycle costs. The flexskin was placed around the hinge point between the lip and inlet structure, providing a smooth cover to the

hinge line. The flexskin was successfully demonstrated during wind tunnel testing and under representative flight conditions [4].

Subsequently, the Smart Wing Program looked to develop control surfaces to optimize aerodynamic performance. The program objectives were to improve the overall pressure distribution along the wing and reduce the chances of premature flow separation, which was sometimes seen with the more conventional hinged control surfaces. Figure 2.3(a) shows a picture of the constructed control surface segment without its elastomer skin. Adjacent, Figure 2.3(b) displays a diagram of the cross-section of the control surface segment with its elastomer skin attached. It is shown that the segments utilized a honeycomb core to structurally support the silicone skin, which was adjacently attached to a center laminate with an aluminum tip.

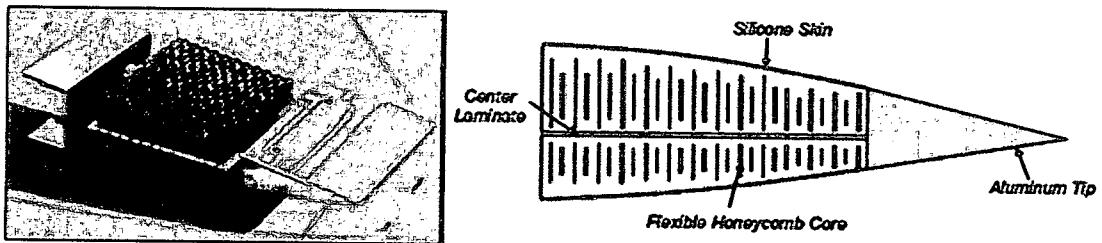


Figure 2.3: (a)Picture of conformal control surface without elastomer skin
(b)Drawing of cross section of Smart Wing construction with skin

A seamless, smooth elastomeric control surface was utilized, which was an evolution of the MAW technology, to provide the needed deformation for this project [9]. Figure 2.4(a) shows the test vehicle mounted in the wind tunnel with the smart wing and traditional control surfaces on opposing trailing edge surfaces. The conformal control surface consisted of 10 identical segments, manipulated into over 70 different shapes during testing. These 10 elastomeric conformal control sur-

faces were actuated via an ultrasonic piezoelectric motor. Two sample deflected configurations are shown in Figure 2.4(b).

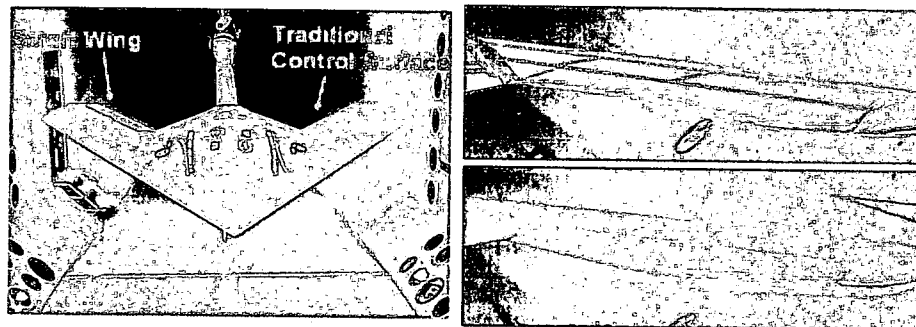


Figure 2.4: (a) Vehicle mounted in the Wind Tunnel (b) conformal control surface

The projects described above demonstrate the continuing desire to conduct shape change and the active role flexible skins have in enabling this technology. Additionally, recent efforts have addressed large scale area changes for aircraft structures made possible by flexible skins. Two representative morphing aircraft concepts which demand large controllable stiffness skins, are shown in Figure 2.5. The folding wing shown in Figure 2.5(a) remains unfolded for loiter or endurance flight, and folds its wings into a "Z" configuration for attack or dash flight. This representative aircraft completes its out-of-plane morphing via a bending motion, allowing for a 280% change in area. A flexible skin that could undergo large bending deformations was required for this case to maintain a clean aerodynamic surface at the hinge joints [10].

Another approach to achieving large area changes is a wing that would perform an in-plane morph via a large shearing deformation, such as that shown in Figure 2.5(b) [10]. This skin design is required to undergo large shearing deformations when it changes from its loiter to dash flight. During loiter or endurance

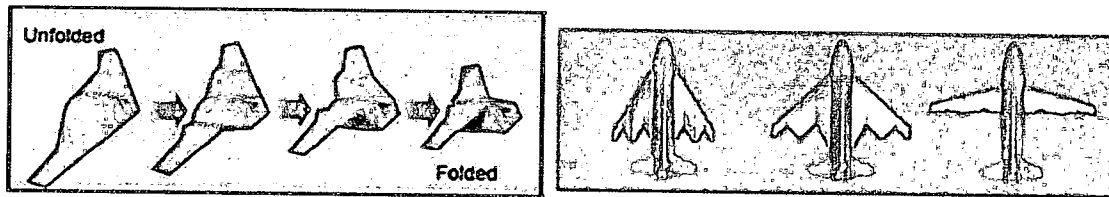


Figure 2.5: (a) Out-of-Plane Morphing aircraft concept, (b) In-Plane Morphing aircraft concept

flight, the wing is in its forward swept configuration providing a higher aspect ratio which is more aerodynamically efficient for those regimes. During the swept wing configuration, when the freestream airflow sees the airfoil as $1/3$ thinner reducing drag, where the aircraft would behave more effectively in attack or dash scenarios. These two different types of morphing motions present their own separate challenges in terms of boundary conditions, actuation, deformation rates, and in-plane and out-of-plane deformation.

The elastomeric skins discussed here provide effective solutions for these specific projects and their requirements. It is important to note that the elastomeric skins are required to undergo small deformations, while this project requires large deformations.

2.1.3 Shape Memory Polymers

To illustrate ranges over which some materials work, current monolithic materials are plotted in Figure 2.6. This figure shows monolithic materials, or currently available, non-engineered materials, in terms of their reversible strain versus their stiffness [11].

Elastomers are a passive material which can be elastically deformed via chain unfolding or bond stretching. Also, polymers are shown as materials which

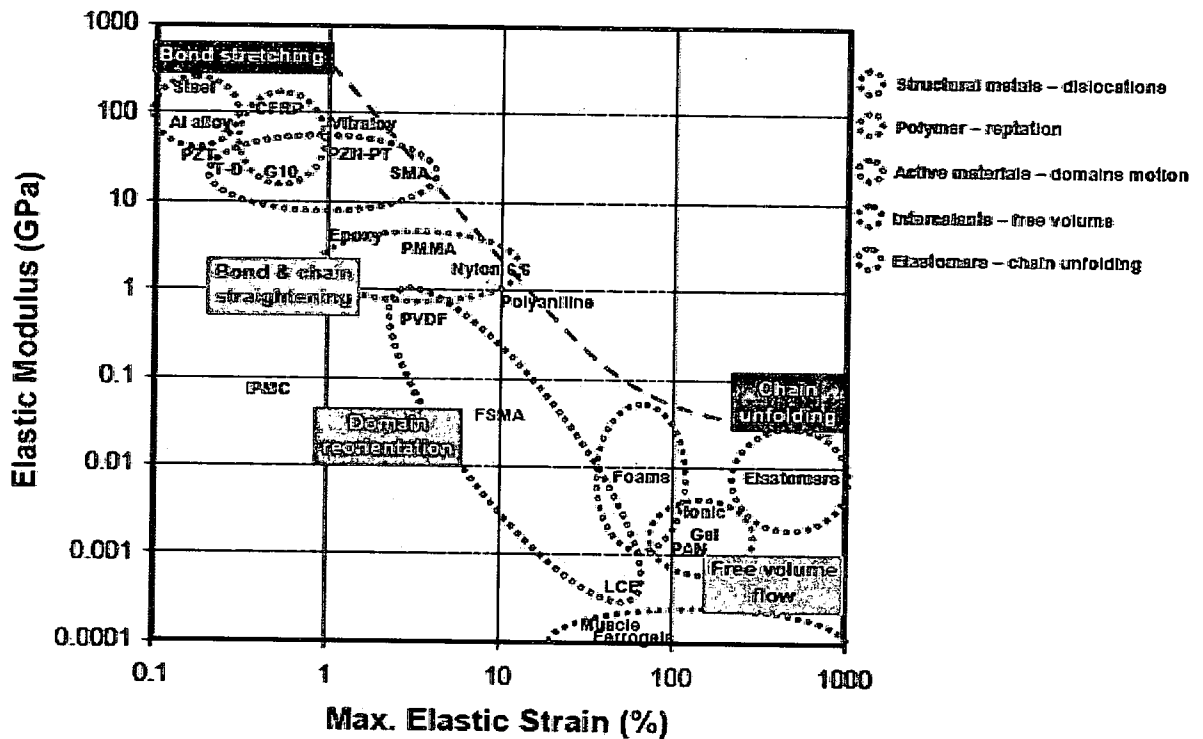


Figure 2.6: Modulus versus Strain Trade Space for Existing Materials [10]

deform via repetition or creeping. However, Figure 2.6 conveys that larger strains are only reasonably achieved utilizing polymers. Elastomers which are capable of complying with larger strains, suffer severe compromise in material properties such as poor toughness, increased temperature sensitivity, reduced durability, and low stiffness. Thereby making elastomers undesirable to use as a structural material [7].

Another material concept has emerged that could also be used for shape control is Shape Memory Polymer (SMP). This material is capable of large strains and requires no force to hold the deformation. SMP is an active material described, ... "where internal energies such as thermal, electric, or magnetic are coupled to the

mechanical energy and therefore provide a potential to manipulate the deformation mode [12]."

As a polymer there are two classes of SMP. Depending on the crosslinking within the polymer, SMPs are classified as a thermoset or a thermoplastic. Additionally SMPs are further divided up into polyurethane based SMP and polystyrene based SMP. Polyurethane based SMP is the most well known and researched polymer with shape memory behavior. Other types of polymers which exhibit a shape memory effect include a styrene-butadiene thermoplastic copolymer system, a class of stearyl acrylate and acrylic acid or methyl acrylate, and norborene or dimethaneoctahydro-naphthalene homopolymers or copolymers [13].

The modulus change of SMP can be thermally or non-thermally triggered. The material which can be non-thermally triggered is called light-activated shape memory polymer (LASMP). The LASMP has monomers which are crosslinked via a light source whereas the thermally activated SMP crosslinks via heating [14]. The LASMP was investigated with the intention of developing a method that allowed for a quicker response time or change in modulus. Currently, however, response times are about the same for the thermally activated and non-thermally activated SMP [14]. Therefore, a thermally activated SMP is investigated in this project because of its accessibility.

Thermally activated shape memory polymers exhibit a thermo-mechanical cycle. Figure 2.7 is a plotted representative cycle. At box 1 in the figure, the SMP starts in the rigid, plastic state. As the temperature is increased and surpasses its glass transition temperature, T_g , the material modulus decreases and enters the flexible, elastic state. The glass transition temperature (T_g) is defined as, "The temperature at which an amorphous polymer (or the amorphous regions in a partially crystalline polymer) changes from a hard and relatively brittle condition to a

viscous or rubbery condition [8].” While above the T_g , at box 2, within the elastic state, a force can be applied to the material, deforming it to a desired shape. Holding the deformation force, the material is then cooled to the plastic state. At box 3, the deformation force then can be removed and the SMP will maintain its shape. To return the material to its memorized or original shape, with no force applied, reheat the material back above the T_g . Once the material has returned itself back to the memorized shape, cooling the material below its T_g completes the thermo-mechanical cycle.

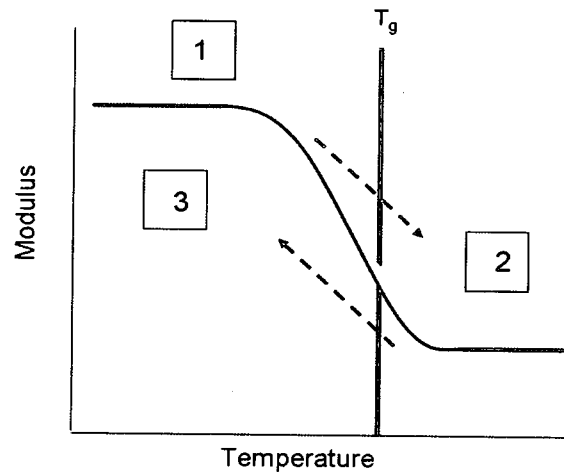


Figure 2.7: Diagram of the SMP Thermo-Mechanical Cycle

Some basic mechanical characterization was performed obtaining the shear properties for a representative SMP called Veriflex®. Table 2.1 shows the experimentally acquired SMP basic material material properties [6]. These results illustrate that the SMP behaves as a nonlinear viscoelastic material and that the properties are time and temperature dependent. It was also concluded that the power and force to active the SMP are similarly rate dependent. Additionally, a

finite element analysis was performed to confirm that the deformation seen during experimentation was material buckling [6]. Bortolin [6] reasoned that the SMP geometry greatly affects its out-of-plane and in-plane behavior.

Table 2.1: Basic Material Properties of an SMP

Shear Modulus, G , of bulk material at $203^{\circ}F$	25.8 +3.0/-3.5 psi
Shear Modulus, G , of pre-strained material - 28% pre-strain at $203^{\circ}F$	38.9 psi
Shear Modulus, G , of pre-strained material - 60% pre-strain at $203^{\circ}F$	28.8 psi
Shear Modulus, G , of bulk material at room temperature	17385 psi
Poisson's ratio from 60% pre-strain at $203^{\circ}F$	0.28
Extreme Positive Shear Load Limit to fracture with formed samples at room temperature	3855 psi

Some basic thermal activation research that has been performed including Veriflex® involves resistively heating imbedded 26AWG (0.0159in) and 36AWG (0.005in) nichrome wires. Both wire gauges were powered with 40 Watts in two separate tests [15]. The resulting heat distribution, shown in Figure 2.8, was acquired via liquid crystal thermography.

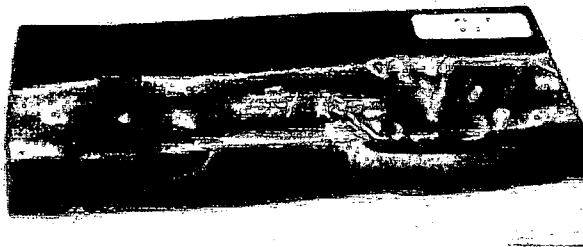


Figure 2.8: 26AWG (left) and 36AWG (right)

Additionally, research with a shape memory polymer with a targeted application of deployable space structures has been conducted. This SMP is utilized as the basis of elastic memory composites (EMC) which are fiber reinforced. To en-

able bend radii of 1.6 mm and recoverability of nearly 100%, the fiber architecture must be tailored to the tow spacing and resin system to avoid delamination and out-of-plane fiber buckling [16].

The controllable stiffness material, SMP, includes material attributes which are desired in a morphing wing skin. These characteristics include the capacity of deforming the SMP with a minimal force while in its soft state, and no large build up of strain when the material is deformed. Knowing that while SMP is in its soft state the material modulus is extremely low; a concept was sought to maintain out-of-plane stiffness while the the SMP is deforming in-plane.

2.2 Structural Concepts

In addition to monolithic material approaches to flexible skins, some structural design concepts have been proposed to control effective skin properties. Structural conceptual ideas that have been published include an extensive investigation of multi-role, kinematically active materials. The investigation divided up the materials technologies into categories of monolithic, composite, and engineered materials [17].

A fundamental material property, Poisson's ratio, is defined as, "...the ratio of the lateral contractile strain to the longitudinal tensile strain for a material undergoing tension in the longitudinal direction, i.e., it is a measure of how much a material becomes thinner when it is stretched [18]." Most materials have a positive Poisson's ratio, meaning that they contract when they are in tension, however, auxetic materials have a negative Poisson's ratio. A negative Poisson's ratio can be taken advantage of when an auxetic material is deformed in a uniaxial direction, thereby

exhibiting expansion instead of contraction transverse to the direction. Such a concept may be useful when pursuing an extensional based morphing mechanism.

Auxetic materials were reviewed in terms of naturally occurring and man-made materials. Naturally occurring auxetic materials include molecular auxetics, i.e., iron pyrites, cadmium, and arsenic, which are connected to the metal's work function, and microstructural biomaterials, i.e., cat skin and cow teat skin. Man-made auxetic materials include keyed brick structures, cellular materials, i.e., honeycombs and foams, microporous polymers, composites, ceramics, and molecular auxetics [12].

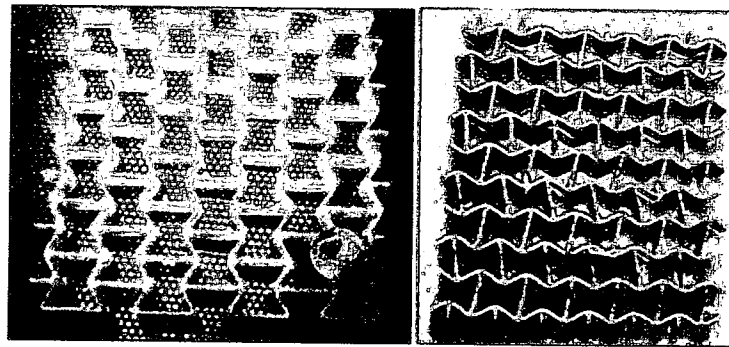


Figure 2.9: SMP auxetic cellular structure in neat resin and with carbon [16]

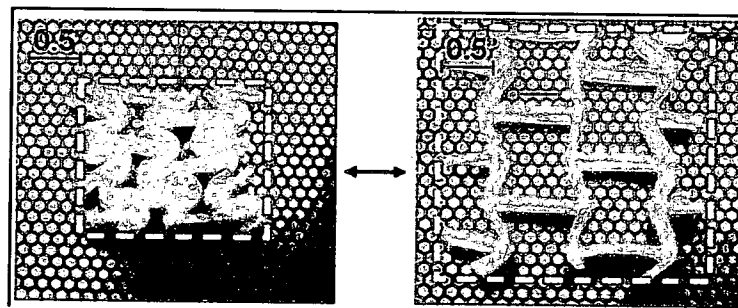


Figure 2.10: SMP auxetic effect [11]

Figure 2.9 shows an auxetic cell structure made out of the Veriflex® SMP [17]. The structure on the left is neat resin, resin with no additives, and the structure on the right is carbon fiber reinforced resin. To give an idea of the amount of deformation capable with SMP, Figure 2.10 shows a neat resin SMP auxetic cell structure compressed on the left, and expanded with over a 130% area change on the right [12].

McKnight and Henry [11] determined that several issues existed which need to be resolved to further cellular based reconfigurable materials. These issues included dependence upon the cell wall within the cellular structure behaving as the deformation mechanism, where a large loss of stiffness occurs. Additionally, the deformation was dependent on controlled large buckling effects. While, the motion to the return to the memorized configuration during compression, yielded terrible stability because of the low in-plane modulus [11].

Cellular structures provide a promising and effective concept to explore, however, consideration must be taken for the aerodynamic efficiency of the morphing wing skin and the overall concept integration. Therefore, sandwich construction is discussed in the next two sections in an effort to develop a fully integrated morphing wing skin system.

2.2.1 Origins of sandwich construction

A hybrid skin concept that allows for deformation while remaining aerodynamically smooth is needed to meet the requirements of this project, therefore sandwich construction was considered. The idea of sandwich construction dates back to 1849, however the concept was not used until World War II. In the United States, sandwich construction began with a lower density core inserted between

reinforced plastic faces. This progressed to a balsa-wood and glass-fabric honeycomb core sandwiched between fiberglass-reinforced polyester faces as part of the Vultee BT-15 fuselage, which was designed and fabricated in 1943 [19].

Early sandwich research concerning analysis and design methods, conducted post-World War II until the mid 1960s, was conducted predominately by the United States Forest Products Laboratory (USFPL). The USFPL published the MIL-HDBK-23, the Military Handbook on Structural Sandwich Composites, and continuously updates the document.

2.2.2 Uses of sandwich construction

Sandwich construction has been adapted for use in nearly everything in everyday life. The transportation industry, in particular, has benefitted from the weight savings sandwich construction provides. Specifically, the aircraft industry began using this construction method in the 1940s with the manufacture of the British Mosquito bomber. Today in the western world, every two or more engine aircraft, in both the commercial and military sectors, utilizes some form of honeycomb sandwich. An excellent example is Boeing's commercial airliners, with Nomex honeycomb sandwich construction use increasing with airliner size. While in the private aircraft industry, the Beech Starship was the first all sandwich aircraft using Nomex honeycomb with Kevlar or Graphite face sheets [19].

In the rail industry, sandwich construction has been adapted for manufacture of locomotives. Composite front cabs have been in use since 1980 in France, Australia, Sweden and Italy [19]. The use of composites, where steel and aluminum were originally used, has reduced the weight of individual locomotives by roughly 1000 kilograms.

The United States (US) Navy and the Royal Swedish Navy both use sandwich construction on their vessels. The US Navy utilizes this construction technique on bulkheads to reduce the weight of the ship above the water line. While, the Royal Swedish Navy utilizes sandwich construction on the hulls of their vessels. The graphite and fiberglass sandwich is designed to withstand debris and underwater explosions, which are the same conditions steel hulls must meet. Additionally, the composite hulls have the advantage of not attracting magnetic mines and canceling out salt water corrosion. Other vessel applications include ferry boats in the Pacific Rim and Scandinavian countries, sailing dinghies, and pleasure craft [19].

Sandwich construction is finding its way into civil engineering applications due to its excellent thermal performance. It's being used in infrastructure rehabilitation and as roof and wall cladding or covering. Additionally, honeycomb sandwich construction is also utilized in race cars, canoes, water and snow skis, kayaks, pool tables, and absorption of sound and mechanical energy [19].

2.3 Chapter Summary

In this chapter several material structural concepts for designing flexible skins have been reviewed. The sliding and elastomeric skin concepts, which were previously investigated, provided only a small amount of deformation. This fulfilled the requirements of the respective uses. Additionally, structural concepts capable of controlling effective skin properties were examined. Concepts and approaches to integrate the reviewed information into a single researchable concept is discussed in the next chapter.

Chapter 3

Conceptual Designs

3.1 Functional Requirements

This project was setup to gain a greater understanding of the competing requirements and their application to highly deformable morphing aircraft skins. The objectives were further broken down into the understanding of structural skin reinforcement to allow a desired motion, and the method to activate the smart material response.

3.2 Design Requirements

The design requirements for this project include that the skin concept must have the capability to meet the in-plane deformation requirements, including a 100% area change. Also, the skin concept must have stiffness to resist the out-of-plane deformation and pillowing from aerodynamic loading due to active flight conditions. The final requirement that must be met is that the skin concept should have the capacity to be effectively researched within the allotted amount of time.

3.3 Design Criteria

To effectively determine which concept should be investigated design criteria were set forth with corresponding weights. These design criteria weights are

assigned via the system of 10 being the most important and 1 the least important. The weights, shown in the list below in the parentheses, allow for numerical values to be assigned thereby providing a method for determining the most promising concept. Each concept is then assigned a rating for each design criteria. The rating is then multiplied by it's predetermined weight, and all of the criteria are summed. The design concept with the highest value is the most promising concept.

- Manufacturability (10) - There was a limited time frame on this project, therefore, the skin concept needs to be advanced to a point of proof of concept.
- Materials (10) - Accessibility and ease of manufacture with the controllable stiffness material must be considered.
- Weight (9) - Since the morphing skin will be part of an aircraft the weight must be as light as possible.
- Size (8) - Since this is a proof of concept the test size does not need to be large, however, practicality (i.e. power requirement, weight) in applying the concept to a full wing must be considered.
- Environment (7) - The controllable stiffness material will be affected by the natural environment under normal operation and must not pose a danger to workers during processing and manufacturing.
- Performance/Reliability (5) - The point was a proof of concept, therefore the concept needed to perform but did not need to be reliable.

The analysis that was completed utilizing the design criteria is shown later in the chapter.

3.4 Concepts

Utilizing the knowledge acquired from previous research, nature was looked to for inspiration. A unique animal found in the tropical forests of southeast Asia is the Flying Dragon [20], otherwise known scientifically as *Draco Volan*, shown in Figure 3.1. This particular lizard has the capability to expand and contract from the side of its body, folds of skin which are supported by ribs. These folds of skin are utilized as wings to glide when the lizard leaps from tree to tree with the capability to glide up to 30 feet.



Figure 3.1: Flying Dragon [19]

Nature also inspired the following earthworm concept considered for morphing skins, shown in Figure 3.2. Earthworms have layers of longitudinal and circular muscles which allow for the worm to become long and thin when the circular muscles are contracted. Correspondingly, when the longitudinal muscles are contracted the worm becomes short and fat.

This is a bi-axial deformation concept. The idea was to utilize a layering effect with long hollow tubular vessels which had a preset pressure of air or gas.

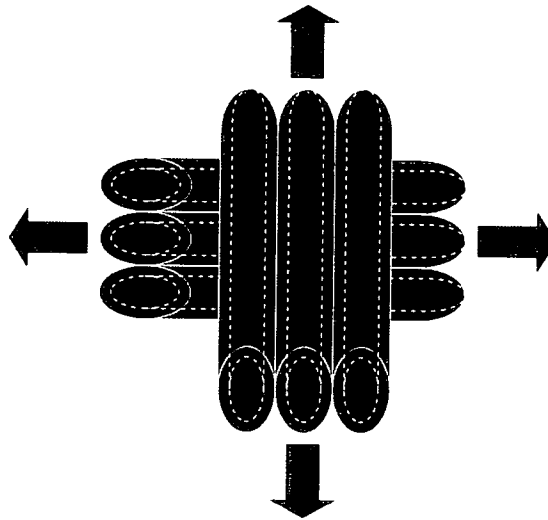


Figure 3.2: Earthworm concept

The tubular vessels would be made of SMP with a carbon fiber, Chinese finger trap type weave within the polymer. To lengthen the wing along the chord or span, the SMP is heated above its transition temperature and the pressure is reduced within the vessel below the wing loading pressure. Correspondingly, to contract the wing, the pressure within the vessels is increased above the wing loading pressure.

Another concept that was considered was the half baby gate mechanism shown in Figure 3.3. This is a uni-axial deformation concept. The concept would have utilized two engineered SMP materials with two different glass transition temperatures.

The SMP with the higher transition temperature would be placed at the hinge points thus providing a loading area while the rest of the material's modulus is too low to take the load. The concept was considered since it has less joints than a full baby gate mechanism, thereby providing fewer possible problem areas.

An idea which could utilize kinematics is shown in Figure 3.4(a), building off

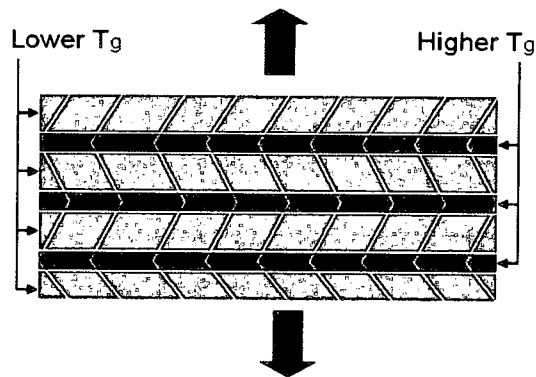


Figure 3.3: Half Baby Gate Mechanism Concept

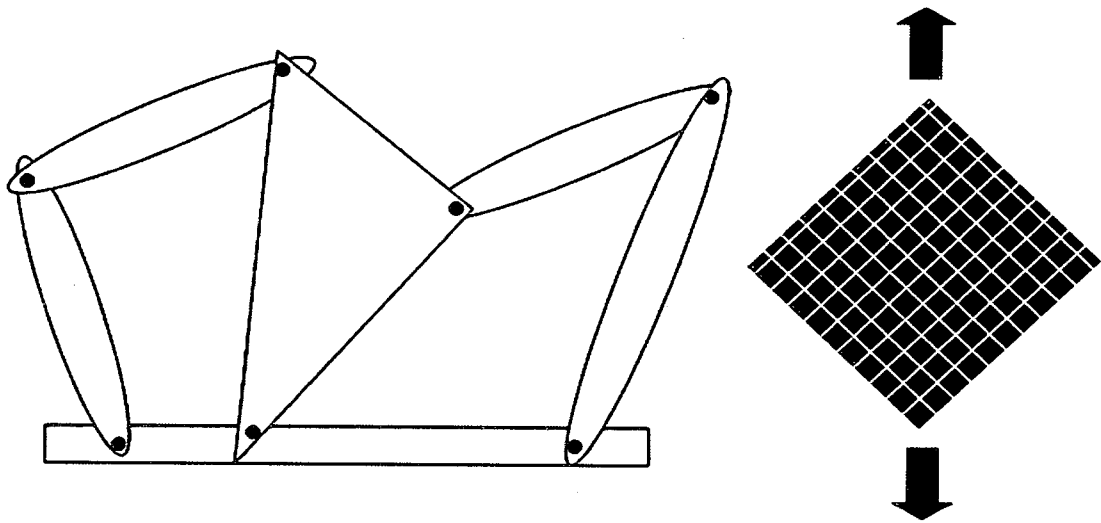


Figure 3.4: (a) Kinematic Chain reinforcement mechanism (b) Carbon Fiber integrated shear concept

of current construction configurations utilized today. This concept would attach kinematic bar mechanisms to the spar in the wing. However, this idea would be difficult to implement without specially designed wing structures being utilized to properly deform morphing wings. Figure 3.4(b) shows the carbon fiber integrated shear concept, meant to mimic the baby gate concept without the hinge points.

This shear deformation concept expanded upon work which was done previously with SMP characterization.

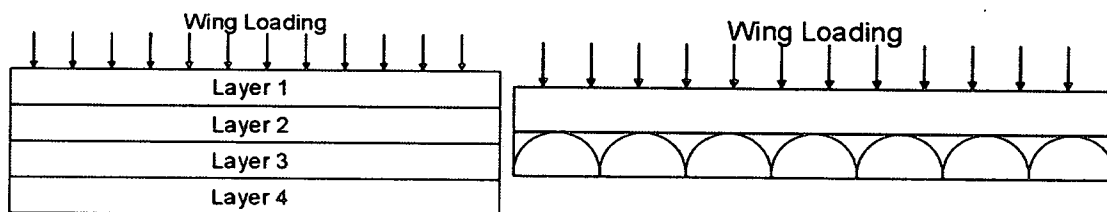


Figure 3.5: (a)Generic SMP layer concept (b)SMP layer concept with Arches

The most promising skin concepts involve layers or some form of sandwich structure. Figure 3.5(a) shows a generic SMP layer concept. An example of what these layers could consist of includes layer 1 as SMP with a higher T_g temperature, layer 2 designed as a morphing assist layer with heating elements, a phase change materials to act as a heat source and sink, and some support support structure. Layer 3 could then be the SMP with the lower T_g which would then actually transition and deform the overall skin, and layer 4 could be the underlying skin support structure and morphing wing structure attachment point. The idea behind this concept was to maintain wing loading with the top layer while still maintaining the capability to deform the skin. Figure 3.5(b) is a variation on part (a) of the figure that shows arches or some other form of kinematically movable structure which would maintain the wingloading during transition.

An idea that was considered at this point in the research included providing radiation shielding for the skin to maintain temperature and reduce effects from ambient heating or freezing at various altitudes. Additionally, other smart materials such as shape memory alloy (SMA) wires, ribbons, thin sheets or tubes were considered for integration into the concepts. Different structural configurations and

magneto-rheological (MR) fluid were also considered for integration into the concepts.

3.5 Decision Analysis

A decision analysis, shown in Table 3.1, was completed utilizing the design criteria and assigned weights as presented in the third section of the chapter.

Table 3.1: Decision Analysis

		EarthWorm Concept		Half Baby Gate Concept		Kinematic Chain Concept		Carbon Fiber Shear Concept		Sandwich Concept	
		Biaxial Deformation		Uniaxial Deformation		Uniaxial Deformation		Shear Deformation		Biaxial/ Uniaxial Deformation	
Design Criteria	Weight	Rating	Value	Rating	Value	Rating	Value	Rating	Value	Rating	Value
Manufacturing	10	4	40	6	60	7	70	8	80	9	90
Materials	10	4	40	6	60	7	70	8	80	9	90
Weight	9	8	72	7	63	6	54	8	72	8	72
Size	8	9	72	9	72	6	48	10	80	10	80
Environment	7	7	49	7	49	7	49	7	49	7	49
Performance /Reliability	5	8	40	8	40	8	40	10	50	10	50
		sum	363	sum	304	sum	331	sum	431	sum	441
Overall Rating		3		5		4		2		1	

Table 3.1 shows the ratings and values that were assigned to each concept. When completing this analysis, the concept with the most points would be chosen, the sandwich concept yielded the most points and thus, the investigation of this concept will be detailed in the subsequent chapters.

3.6 Chapter Summary

Approaches as inspired by nature and other ideas presented were discussed. The functional and design requirements were specified. The design criteria were detailed, weighted, and utilized in the decision analysis, yielding the sandwich concept as the concept to be investigated further.

Chapter 4

Activation Strategy

Building upon previous research, this project is seeking a skin which would allow large deformations and still provide a smooth aerodynamic surface. Therefore, SMPs will be investigated because they allow a large in plane deformation up to 200%, with the hot modulus. Utilizing the hot modulus allows for less power to be used to perform the in-plane deformation.

Progressive advances in material processing techniques, and design tools present the opportunity to design new classes of flexible skin materials. The research presented here, seeks to develop a flexible skin solution based on a controllable stiffness material. The representative SMP material was selected as a flexible skin solution because the material can be manipulated and cooled into a variety of shapes. This SMP material behaves such that a required input energy, external or internal, is applied sending the material to its transition temperature, and a state change is activated. The state change then stimulates the cross-link density to change causing the material stiffness to go from a rigid, plastic state to a flexible, elastic state. This flexible, elastic state as a homogeneous material does not have the required out of plane stiffness to effectively withstand the aerodynamic loads. Thereby, when the skin is reinforced with mechanized structures large in-plane changes are enabled while maintaining out of plane stiffness.

Heterogeneous material solutions for flexible skin optimizations were studied including the geometry of the reinforcements to allow the desired motion, activation of the basic material response, and validation of the topology optimization schemes. With desired material characteristics for the skin design, a detailed heat transfer analysis was conducted and compared to experiments to obtain a thorough understanding of the heat transfer parameters, power required to activate the material solution, and fiber spacing. Experiments were conducted on the proposed concept and compared to analytical solutions.

This chapter discusses, the processing procedure utilized to manufacture specimens and the validation of the material properties from the processing procedure via a Dynamic Mechanical Analysis (DMA). Additionally, an investigation into the approach taken to thermally activate the representative SMP. A thermal activation method utilizing an embedded resistive heating element was investigated. The effects of the heating element on the SMP was confirmed via infrared thermal imaging, and then further analytical validation was completed with a finite difference model.

4.1 Shape Memory Polymer (SMP)

The representative matrix material selected for this investigation was the Veriflex® Shape Memory Polymer (SMP). Veriflex® is a thermoset styrene-butadiene block copolymer [21]. A copolymer is defined as, "...a polymer composed of two or more different repeat units - the result of the simultaneous polymerization of two or more monomers [22]." As described by Patent No. 6,759,481 the, "...SMP is prepared from a reaction product of styrene, a vinyl compound other than styrene, a

multi-functional crosslinking agent and an initiator [13].” The shape memory effect can then be controlled by varying the reactivity ratio of the two monomers.

This SMP is a thermoset based monomeric styrene, which has the characteristic of allowing the material to be rigid and carry loads while at room temperature. This polymeric material crosslinks via two different methods which includes physical and covalent crosslinks. The physical crosslinks resemble knotted strings and the covalent crosslinks are like a loose net. When the material is thermally activated at the material glass transition temperature, T_g , the physical crosslinking is lowered allowing the "knots" to untangle while the "net" or the covalent crosslink remains intact. Therefore above the T_g temperature the material is soft enough and still crosslinked together to permit in-plane deformation with minimal actuation force.

For this research 10 plaques, 10 test specimens with resistive heating elements, and 2 specialized structural skin dogbones were manufactured. All of these specimens were made with the representative matrix material. The next section discusses the method utilized during the processing of the representative matrix material.

4.1.1 Processing of SMP

The manufacturing process involves three fundamental steps. These steps are mixing the resin, pouring the molds, and curing the resin within the molds. The manufacturer provides a process with their product, however, to ensure that the process was being performed correctly, several in-house plaques were made.

This process begins with utilizing acetone to clean everything prior to processing. Any remaining material on items that are used would contaminate the

SMP, thereby altering properties. Also, all of the molds are prepared in order to make the process easier prior to the mixing of the resin. For all molds, two pieces of appropriately sized glass were cleaned thoroughly with acetone. These pieces were placed on aluminum foil to minimize debris and coated with a mold release. Teflon, Monacoat and Freekote can also be utilized as a mold release with this thermosetting SMP. Figure 4.1 shows the mold release being applied. Three coats of mold release were applied to the glass plates, allowing appropriate drying time between each coat. It is important to note that excess mold release causes defects in the final product. Also defects can be caused if mold release is not applied at all to the glass, thereby enabling the SMP to outright adhere to the glass.



Figure 4.1: Mold Release being Applied to an Exterior Glass Plate

Once the coats of mold release dried, the mold was assembled. Initially a silicon rubber spacer was utilized, however, it was later replaced with Viton® rubber to minimize material interaction problems while working in conjunction with the SMP. For the simpler plaque mold, the glass and rubber spacer was then clamped

together with binder clips as shown in Figure 4.2. The open top area was used to pour the resin into the mold and then sealed with a strip of rubber to create a closed mold.

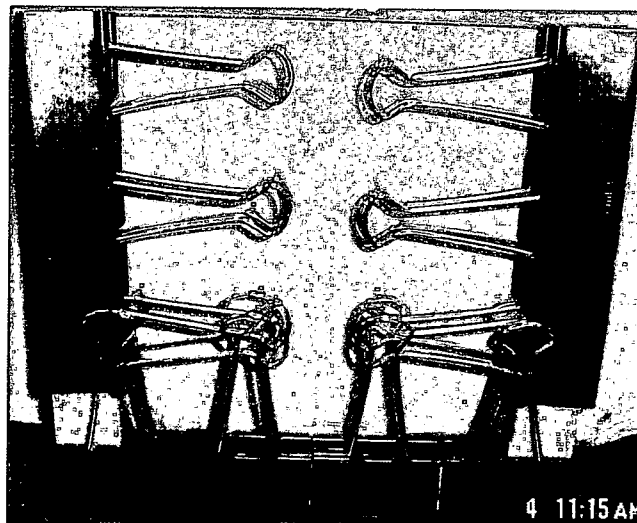


Figure 4.2: Assembled Mold

Once the resin was ready to be poured and mixed, a Pyrex® beaker was placed on a digital scale, zeroed, and the calculated volume of resin for the corresponding mold size was then added. For example, a plaque size of 7"x7"x1/8", requires 100.37 mL of resin. Utilizing the resin to hardener ratio provided with the product, which is 288 grams of resin to 12 grams of hardener, the appropriate amount of hardener was added to the resin within the beaker.

The resin and hardener were then poured together and placed into a mixer to incorporate them as homogeneously as possible. The resin was mixed in a FlackTek SpeedMixer DAC 150 FVZ-K utilizing a dual asymmetric centrifuge at 3500 RPM for 30 second pulses to prevent heating and premature cure of the

resin. The resin underwent four pulses totaling two minutes. This mixed resin was poured into the plaque as shown in Figure 4.3.



Figure 4.3: Pouring the Resin into the Mold

The poured plaques were cured via the cure cycle as detailed by the manufacturer on the Veriflex® resin can. The manufacturer cure cycle is as follows in Table 4.1.

Table 4.1: Veriflex® manufacturer cure cycle

Ramp	60min to 167°F
Hold	180min at 167°F
Ramp	180min to 194°F
Ramp	120min to 230°F

Iterations to the manufacturing process were made over the course of the research. A very important change that occurred during the research was that the entire pouring process was moved to the confines of a hood, due to Styrene exposure concerns. Additionally, due to flaws during cure, the cure cycle was

altered to an extended sequence as follows in Table 4.2. The refined process described above was the method used for subsequent specimen manufacturing.

Table 4.2: Veriflex® extended cure cycle

Start	72°F	1 hour
Ramp	167°F	2 hours
Hold	167°F	36 hours
Ramp	194°F	5 hours
Ramp	230°F	4 hours
Ramp	72°F	1 hour

Several specimens were made utilizing the manufacturing process described above including 10 plaques, 10 thermal activation specimens, and 2 specialized structural skin specimens. Initially, several neat resin plaques were made to develop an understanding of how to process the SMP. This was completed because the manufacturer had provided all prior test specimens as already cured sheets, hence, an effective method to process the resin was sought. The SMP processing was validated via Dynamic Mechanical Analysis, which will be described in greater detail in the next section. Next, 10 thermal specimens were manufactured with three separate resistive heating elements embedded within the SMP. These resistive heating elements were a carbon fiber tow, nichrome wire, and SMA wire. One of each resistive heating element was tested with the other spare specimens available in case the tested specimen was damaged or broken. Two additional, more complex specialized structural skin specimens were manufactured. These specimens are discussed in more detail in the following chapter. The manufacturing process showed that the SMP could be molded into any desired shape as long as a proper mold could be made to contain the resin during the curing process.

4.1.2 Dynamic Mechanical Analysis Testing

Dynamic Mechanical Analysis (DMA) is defined as, "A technique that employs a low-strain, oscillatory stress in order to quantify the viscoelastic behavior of materials [8]." DMA tests were conducted to validate the manufacturing process of the SMP specimens. The DMA machine determines the storage modulus or the elastic response, which is abbreviated as G' . The storage modulus is, "...the portion of the stress-strain response which is in phase with the applied stress...the polymer structure that fully recovers when an applied stress is removed [8]." Also, the testing detects the loss modulus or viscous response which is designated as, G'' . The loss modulus is, "...the portion of the stress-strain response which is out of phase with the applied stress...the polymer structure that undergoes viscous flow when a load is applied [8]." These values are determined as a function of temperature. Additionally the complex or dynamic modulus, G^* , is calculated via equation 4.1.

$$G^* = \sqrt{(G')^2 + (G'')^2} \quad (4.1)$$

The DMA test machine utilized is shown in Figure 4.4. The figure shows the test oven closed over the test specimen location. This particular test setup utilizes a torsion rectangular geometry test which controls temperature and strain.

The test specimens utilized for the DMA tests were rectangular in shape at 2in tall, 0.5in wide, and up to a thickness of 0.25in. The tests were conducted with an initial temperature of 27°C, a ramp rate of 2°C/min, and a final temperature of 177°C. A frequency of 100rad/sec with a strain rate of 0.05%, 0.1%, or 0.5% were used for all tests. However, the strain rate of 0.5% was too intense for the SMP and did not yield any valuable data. These test conditions were chosen based upon the

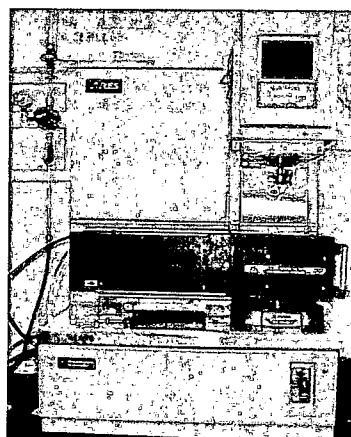


Figure 4.4: DMA test machine

manufacturers stated glass transition temperature, T_g , and previous experience. Sepe [8] defines the glass transition temperature, T_g , as, "the temperature at which an amorphous polymer changes from a hard and relatively brittle condition to a viscous or rubbery condition." Overall nine tests were completed is detailed in Table 4.3

Table 4.3: DMA Tests

Test Specimen Designation	Type of Specimen	Strain Rate
SMP072905-2-6x6x0.125-DMA1	Neat Resin	0.1%
SMP072905-2-6x6x0.125-DMA2	Neat Resin	0.1%
SMP072905-2-6x6x0.125-DMA3	Neat Resin	0.1%
SMP080505-2-6x6x0.125-DMA1	Neat Resin	0.1%
SMP080505-2-6x6x0.125-DMA2	Neat Resin	0.1%
SMP080505-2-6x6x0.125-DMA3	Neat Resin	0.1%
SMP080505-2-6x6x0.125-DMA4	Neat Resin	0.05%
SMP080505-2-6x6x0.125-DMA5	Neat Resin	0.5%
SMP090605-2-6x6x0.125-DMA1	Carbon Nanotubes	0.1%

Figure 4.5 shows a representative DMA data set acquired from testing that demonstrates how the moduli behaves as the result of a temperature increase.

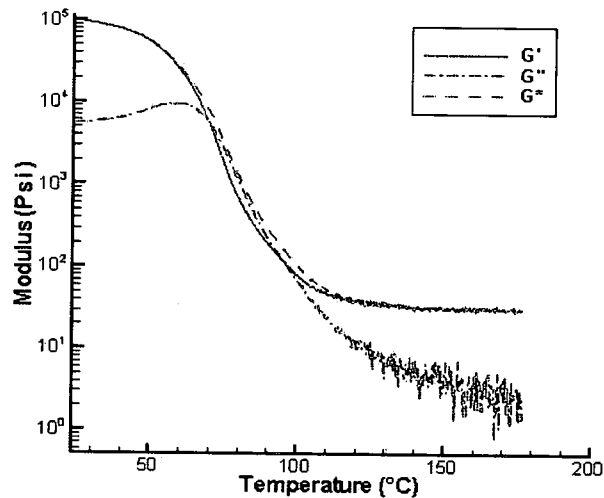


Figure 4.5: Representative DMA Test Results

Sepe [7] makes the point, which is seen in Figure 4.5 that the glass transition occurs over a series of temperatures, despite the fact that classically the loss modulus peak is generally recognized as the glass transition temperature. Figure 4.5 shows both the experimentally acquired loss and storage values, as well as the calculated values of the complex modulus. Therefore, in regards to the skin, if the temperature can be controlled, the modulus can correspondingly be managed providing for a more effective engineered skin solution. Appendix A contains the remainder of the test data acquired during DMA testing. DMA testing verified the processing method as well as validating the T_g .

4.2 Thermal Activation Method

Resistive heating is utilized in all kinds of common applications, such as an electric stove heating element and some potential aerospace applications involving shape memory alloys [4]. As part of this project, two heating methods were inves-

tigated. The first heating method utilized embedded carbon nanotubes, while the second heating method employed embedded wires. This research was interested in a multifunctional solution where the heating element may also be able to carry a load as well.

4.2.1 Nanotubes

Resistively heating via embedded carbon nanotubes was initially examined. A plaque of SMP was manufactured with 4% by weight Silver-plated carbon nanofibers added to the resin prior to cure [23]. A sample size, 5.5in long and 3in wide, was then cut from the nanofiber plaque, and a corresponding neat resin control sample from an already manufactured plaque. If the resistance is too large, not enough current will pass through the material to resistively heat the SMP. In contrast if the resistance is too low the current will not resistively produce an adequate amount of heat to reach the glass transition temperature. These samples were tested by Julius Brodbeck, within the Materials Directorate, via the ASTM D991 Standard Test Method for Volume Resistivity of Electrically Conductive and Antistatic Products.

The test included two five pound conductive probes, Teflon insulation disks, a jumper wire, and a garment plate. Figure 4.6 shows the test setup utilized to measure the electrical resistance of the two specimens. More specifically, Figure 4.6 (a) shows the setup that was used to acquire the resistance through the volume, while Figure 4.6 (b) shows the test setup that was utilized to test resistance top to top (R_{tt}) of the specimen. Testing was completed and the resistance top to top (R_{tt}) and through the thickness of the material (R_{vol}) were acquired. Table 4.4 shows the resistive test results of the test specimens for 120 and 1000 volts DC. The

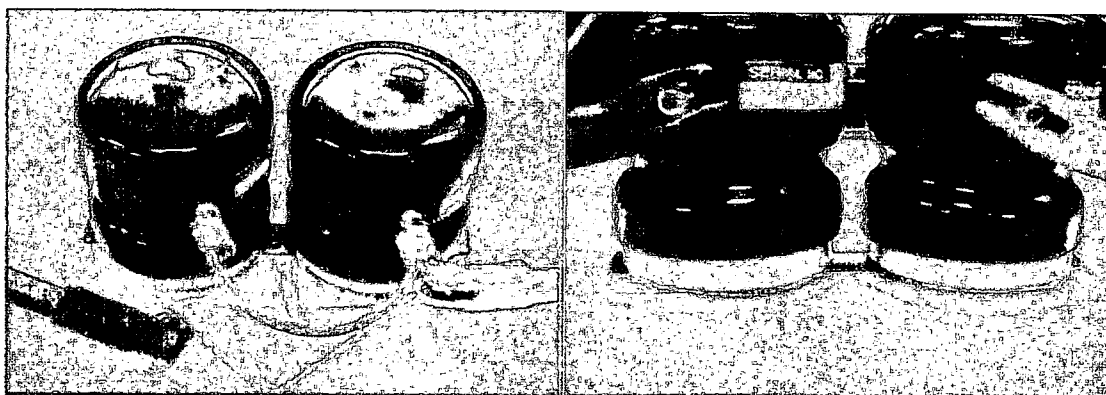


Figure 4.6: Rvol test setup (a) Rtt Test Setup (b)

carbon nanotube specimen did not provide the significant increase in conductivity desired, as shown by the same magnitude of values within Table 4.4. This lack of conductivity increase was due to an ineffective dispersion method, that caused the conductive components to not be accessible at the surface of the specimen to provide electrical contact.

Table 4.4: Rvol and Rtt Test Results

Test Method	Material	@120VDC	@1000VDC
Rtt	Nanotube Specimen	10^{14} ohms	10^{14} ohms
Rtt	Nanotube Specimen	10^{14} ohms	10^{14} ohms
Rvol	Nanotube Specimen	2.3×10^{13} ohms	2.0×10^{13} ohms
Rtt	Neat Specimen	3.8×10^{14} ohms	1.5×10^{14} ohms
Rtt	Neat Specimen	3.8×10^{14} ohms	3.8×10^{14} ohms
Rvol	Neat Specimen	3.7×10^{13} ohms	2.8×10^{13} ohms

4.2.2 Embedded Wires

To more effectively understand the ability to resistively heat the SMP, smaller specimens with a fiber or wire were manufactured. The test section is 1/2in tall by

1in wide and an 1/8in thick with a fiber embedded in the SMP. It was acceptable for the test specimen to be slightly larger, as long as the test section sizes were the same. Three types of resistive heating elements were investigated; Magnamite AS4 carbon fiber, Flexinol SMA wire, and nichrome wire.

4.2.2.1 Resistance Measurements

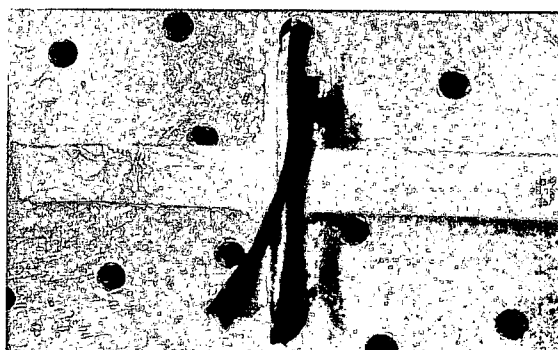


Figure 4.7: Infrared Carbon Fiber Test Specimen

The carbon fiber specimen that was tested is shown in Figure 4.7. This particular specimen was shaped a bit differently due to difficulty in manufacturing the specimen, however, it still maintained the acceptable test section. The carbon fiber that was utilized was a Hexcel Magnamite® AS4 6K tow. This particular fiber was employed because of its availability and tow size. Selected AS4 carbon fiber properties that were utilized during the activation strategy investigation are shown in Table 4.5.

Nichrome is a non-magnetic alloy of chromium and nickel. The material has a high melting point, is corrosion resistant, and has a relatively high resistivity. The nichrome wire specimen that was tested is shown in Figure 4.8 with the acceptable test section.

Table 4.5: Selected Hexcel Magnamite AS4 Carbon Fiber Properties

Typical Fiber Properties	U.S. Units
Density	0.0646 lb/in ³
Electrical Resistance, 12K	9.6 ohms/ft
Electrical Resistivity, 12K	5.03x10 ⁻⁵ ohm-ft
Yarn/Tow Characteristics	U.S. Units
Filament diameter	0.281 mil
Tow cross-sectional area, 6K	3.70x10 ⁻⁴ in ²

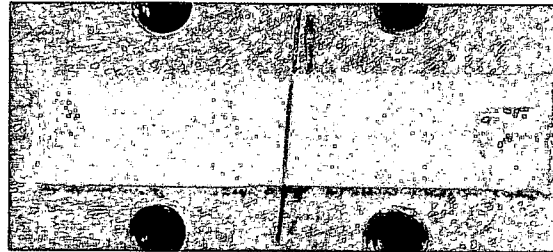


Figure 4.8: Infrared Nichrome wire Test Specimen

Shape memory alloys (SMA) were considered and tested because they have a high work to density ratio. SMAs behave similarly to the representative SMP that is being utilized throughout this work.

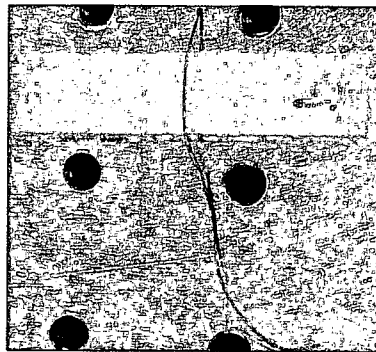


Figure 4.9: Infrared SMA Test Specimen

The tested SMA specimen is shown in Figure 4.9 with the acceptable test

section. The SMA wire that was embedded into the test specimen is a 0.015 inch diameter Dynalloy, Inc. Flexinol® [1] actuator wire. Manufacturer properties for the wire are given in Table 4.6.

Table 4.6: Dynalloy Flexinol® Manufacturer given Properties [1]

Diameter Size	0.015inches
Resistance	0.2(ohms/inch)
Maximum Pull Force	2000grams
Approximate Current at Room Temp	2750mA
Contraction Time	1second
Off Time 70°C	0.281 mil
Tow cross-sectional area, 6K	$3.70 \times 10^{-4} \text{ in}^2$

4.2.2.2 Thermal Imaging

The fiber embedded specimens were tested utilizing an infrared imaging system. The embedded fiber was electrically activated by controlling the power input, using a DC power supply. Data was acquired and utilized to compare with an analytical solution presented in the next section.

Temperature measurements of the SMP test specimen were made using a Mikron Thermo Tracker Type TS7302 Infrared Camera. The MikroScan7302 is capable of measuring temperatures from -40°C to 120°C , while maintaining an accuracy of 2%. Figure 4.10 shows the infrared imaging test setup including the MikroScan infrared camera, the placement of the test specimen behind the foam, and the laptop with the MikroSpec R/T Software.

The software packaged with the MikroScan Camera provides an effective method to acquire videos, images, line profile plots, time/temperature trends, and histograms. This system provides data that is comparable with the analytical ap-

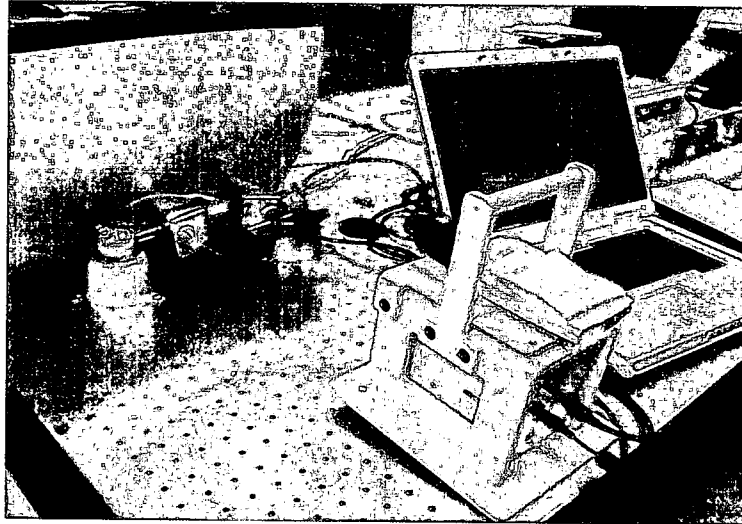


Figure 4.10: Infrared Imaging Test Setup

proach, thereby providing validation of the diameter in the SMP at which the fiber or wire, effectively heats the SMP to its transition temperature.

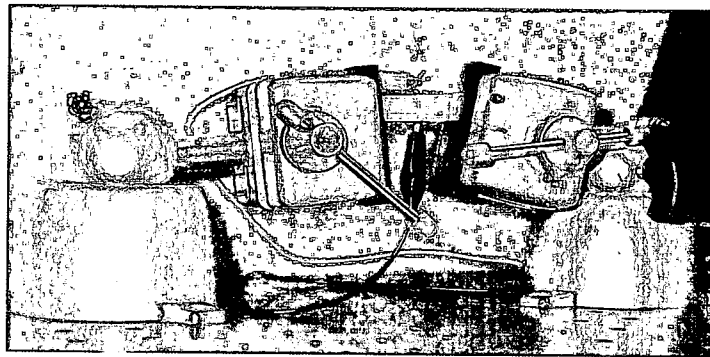


Figure 4.11: Infrared Imaging Test Specimen in Clamps

Experiments were conducted by first mounting the test specimen in the clamps as level as possible as shown in Figure 4.11. Wires from the DC power supply were connected to the wire leads and positioned so as not to interfere with experiment. The infrared camera and laptop were powered up and positioned. The MikroSpec

R/T software was opened and utilized to perform the camera calibration. The camera was repeatedly calibrated due to the increase of ambient temperature as the day progressed. Upon completion of camera calibration, the Regions of Interest (ROI) were defined. The ROIs are the points at which thermal data was acquired by the software program. The embedded fiber was electrically activated by controlling the power input via a DC power supply, monitored as a function of time, and plotted to provide a comparison between the analytical and experimental analyses.

A set of infrared imaging results are presented in Figure 4.12 utilizing a representative test case of a carbon fiber resistive heating element with a current of 0.5 Amps at 300 seconds. Figure 4.12 shows the heat distribution that was acquired from the test.

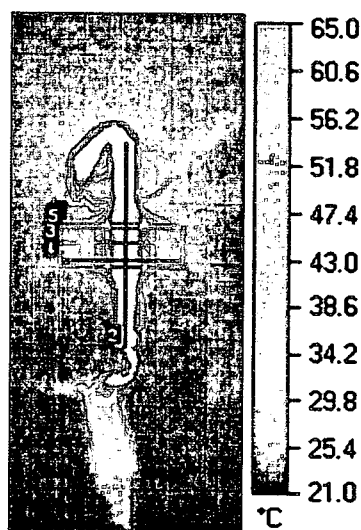


Figure 4.12: Infrared Image for the Carbon Fiber Specimen Resistively heated with 0.5 Amps

To evaluate the rate and efficiency at which a specimen was resistively heated, a test was recorded with a sample rate of thirty seconds. This data was compiled into a line profile comparison plot shown in Figure 4.13. Figure 4.14 shows the

maximum temperature data point that was recorded versus time for the chosen representative test.

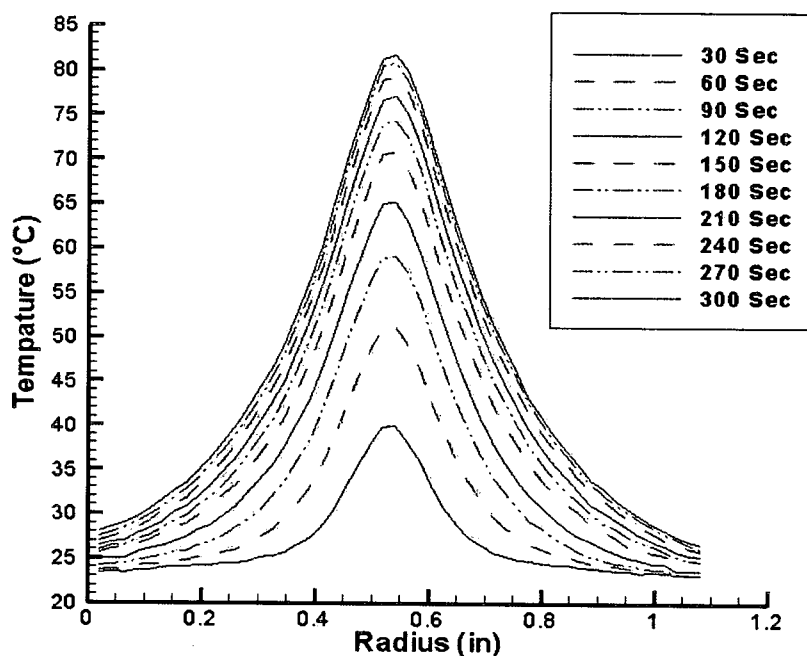


Figure 4.13: Carbon Fiber 0.5 Amp Line Profile Comparison Plot

The carbon fiber, nichrome wire, and SMA wire data is compared with regard to the time required to reach T_g and the temperature distribution provided by each resistive heating element. All heating elements were determined to be acceptable solutions, however, the carbon fiber was investigated further due to its minimal power input, acceptable heat up time with the most uniform heat distribution, low weight, and possession of the best capacity to behave as a multi-functional reinforcing fiber.

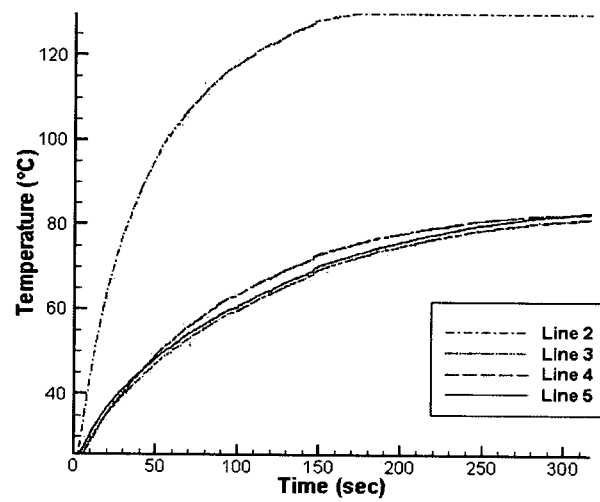


Figure 4.14: Carbon Fiber 0.5 Amp Maximum Data Point Time versus Temperature Plot

4.2.2.3 Finite Difference Model

To more effectively understand the behavior of the heat distribution within the SMP material, a finite difference model was completed. This section will cover the numerical method utilized in this analysis, the power inputs under which the analysis was run, and the data that was acquired from the analytical model. This analytical approach utilizes the finite difference method to represent a cross-sectional area of the heat distribution within the matrix material around a point source. The analysis was completed utilizing the transient two-dimensional transient heat conduction equation, shown in Equation 4.2.

$$\frac{\partial^2 T}{\partial x^2} + \frac{\partial^2 T}{\partial y^2} + \frac{\dot{q}}{k} = \frac{1}{\alpha} \frac{\partial T}{\partial t} \quad (4.2)$$

The finite difference method is a transient, explicit method which determines nodal temperatures based upon nodal temperatures from the previous time step. This model was utilized to determine the temperature of the SMP under predetermined conditions as shown in Figure 4.15. Figure 4.15 displays the cross-sectional area of a test specimen with convection, corner and symmetry boundary conditions. The heat generation point in the center of Figure 4.15 represents the resistive heating element, while the internal nodes are utilized to show how the heat distribution behaves.

A central difference representation of the second order spatial derivatives and forward difference representation of the first order time derivative are utilized to derive the explicit nodal temperature solution for the interior node with heat generation [24], as shown by equation 4.3.

$$T_{m,n}^{p+1} = Fo(T_{m+1,n}^p + T_{m-1,n}^p + T_{m,n+1}^p + T_{m,n-1}^p) + T_{m,n}^p(1 - 4Fo) + \frac{\dot{q}_{m,n}}{k} \Delta t \alpha \quad (4.3)$$

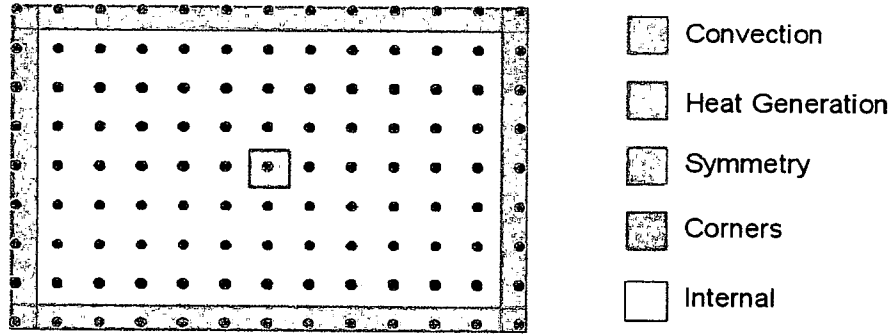


Figure 4.15: Diagram of the Finite Difference model

The point heat source is assumed to be equal to the resistive power generated by driving current through the fiber as shown in equation 4.4 [25].

$$\dot{q} = \frac{I^2 R}{V} = \frac{I^2 R}{dx dy} \quad (4.4)$$

By employing central difference and forward difference representations of the spatial and time derivatives respectively, all other interior node temperatures without heat generation were calculated utilizing equation 4.5.

$$T_{m,n}^{p+1} = Fo(T_{m+1,n}^p + T_{m-1,n}^p + T_{m,n+1}^p + T_{m,n-1}^p) + T_{m,n}^p(1 - 4Fo) \quad (4.5)$$

Since the explicit finite difference method is not unconditionally stable, evaluating the stability criterion was necessary. The Fourier number was defined by equation 4.6, while the stability criterion for the interior nodes was given via equation 4.7.

$$Fo = \frac{\alpha \Delta t}{(\Delta x)^2} \quad (4.6)$$

$$Fo \leq \frac{1}{4} \quad (4.7)$$

The convection boundary condition was calculated for the top and bottom surface of the finite difference model shown in Figure 4.15. The natural convection coefficients were calculated with properties of air at 303K including viscosity, thermal diffusivity, thermal conductivity, and an expansion coefficient. Equation 4.8 calculated the characteristic length of the plate utilizing the plate surface area, A_s , and the plate perimeter, P .

$$L = \frac{A_s}{P} \quad (4.8)$$

Using the characteristic length, the Rayleigh number was then determined via equation 4.9 [24].

$$Ra_L = \frac{g\beta(T_s - T_\infty)L^3}{\alpha\nu} \quad (4.9)$$

Utilizing equation 4.10, the surface of a heated plate Nusselt number was calculated. Both of these values were used to calculate the convection coefficient for the upper and lower surfaces as shown in equation 4.11 [24].

$$\overline{Nu}_L = 0.68 + \frac{0.67Ra_L^{\frac{1}{4}}}{[1 + (\frac{0.492}{Pr})^{\frac{9}{16}}]^{\frac{4}{9}}} \quad (4.10)$$

$$\bar{h} = \frac{k}{L}\overline{Nu}_L \quad (4.11)$$

The temperature of the nodes on the top and bottom were calculated utilizing equation 4.12, with the Biot number evaluated via equation 4.13, utilizing the natural convection coefficients determined above. Additionally, equation 4.14 shows a stability criterion for the top and bottom convection boundary conditions.

$$T_{m,n}^{p+1} = Fo(2T_{m,n-1}^p + T_{m+1,n}^p + T_{m-1,n}^p + 2BiT_{\infty}) + (1 - 4Fo - 2BiFo)T_{m,n}^p \quad (4.12)$$

$$Bi = \frac{h\Delta x}{k} \quad (4.13)$$

$$Fo(2 + Bi) \leq \frac{1}{2} \quad (4.14)$$

As shown in Figure 4.15, the corners were calculated separately using equation 4.15 to calculate the temperature for a node at an exterior corner with convection.

$$T_{m,n}^{p+1} = 2Fo(T_{m-1,n}^p + T_{m,n-1}^p + 2BiT_{\infty}) + (1 - 4Fo - 4BiFo)T_{m,n}^p \quad (4.15)$$

A Matlab file was used to calculate the finite difference solution for predetermined fiber or wire resistances and currents. Table 4.7 shows the resistance and current values that were employed. The currents were determined based on the correlating experimental currents which were already utilized.

Table 4.7: Predetermined Fiber or Wire resistances and currents

Fiber or Wire	Resistance	Current
Carbon Fiber	32 Ω /ft	0.4,0.5,0.6,0.7 Amps
Nichrome Wire	27.95 Ω /ft	1.4,1.845,1.885,2.255 Amps
SMA	94.4 Ω /ft	0.55,1.165,1.24,1.58,2.205 Amps

The results from this model yield a cross-sectional view of the resistively heated specimen. A representative analytical result is displayed in Figure 4.16, which shows the result via grid values utilized within equation 4.6 and 4.13 as the grid size in the x-direction, Δx . Additionally, Figure 4.16 shows how the center of

the specimen achieves a higher temperature compared to the convectively cooled top and bottom surfaces. The surface results from this model are extracted from the data and plotted to show the heat distribution of the surface assuming symmetry.

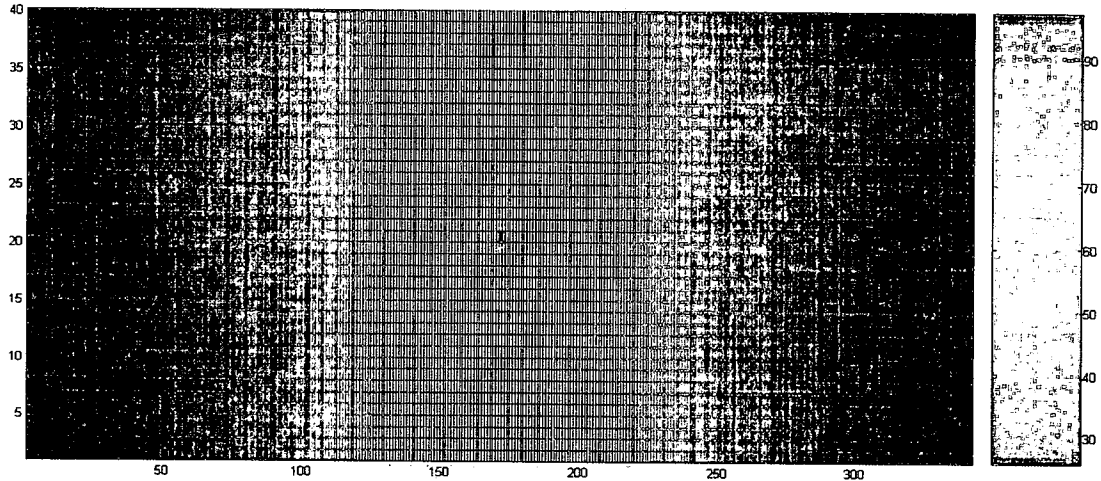


Figure 4.16: Representative Finite Difference Result; Carbon Fiber at 0.5 Amps $32\Omega/\text{m}$ for 300 seconds in Celsius

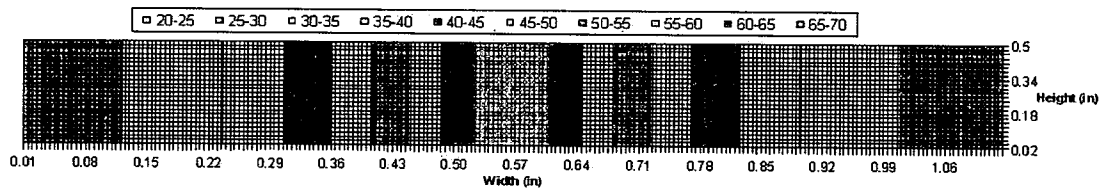


Figure 4.17: Surface Finite Difference Result; Carbon Fiber at 0.5 Amps $32\Omega/\text{m}$ for 300 seconds in Celsius

A representative plot of a finite difference solution is shown in Figure 4.17, which was converted from the grid values to inches to make it comparable with the infrared data that only provides surface temperature. This analytical data is compared with the corresponding experimental results in the next section.

4.2.3 Finite Difference Comparison to Thermal Imaging

This section examines the analytical finite difference data in comparison to the experimental thermal imaging data. To ensure that the specimen and model provide comparable results, the experimental data for the 300 second time step is plotted in Excel and placed next to the final time step of the finite difference data. Figure 4.18 shows the surface finite difference results at the top of the figure and the experimental data at the bottom of the figure. As part of Figure 4.18 a dash-dot line in the center represents the location of the resistive heating element, with dash lines on either side representing the diameter at which SMP reaches its transition temperature. Figure 4.18 shows, for a carbon fiber tow at 0.5 Amps, utilizing the experimental data and the finite difference model, that the approximate distance between the heating elements should be approximately 1/5 inch. For this representative case, the spacing achieves effective heating to provide glass transition for 1/8 inch thick SMP. For this particular case the spacing is optimal and the same procedure is utilized to determine optimal spacing for the remaining cases.

4.3 Chapter Summary

This chapter verified that the manufacturing process employed to create test specimens using the thermally activated SMP was valid. This was confirmed utilizing a DMA test setup at varying strain rates. A thermal activation method utilizing carbon nanotubes or resistive heating elements was investigated. This study included thermal imaging and a finite difference model conducted at several different power inputs. It was determined that the carbon nanotubes did not effectively help the SMP properties due to the SMPs inherent insulating properties. Utilizing the

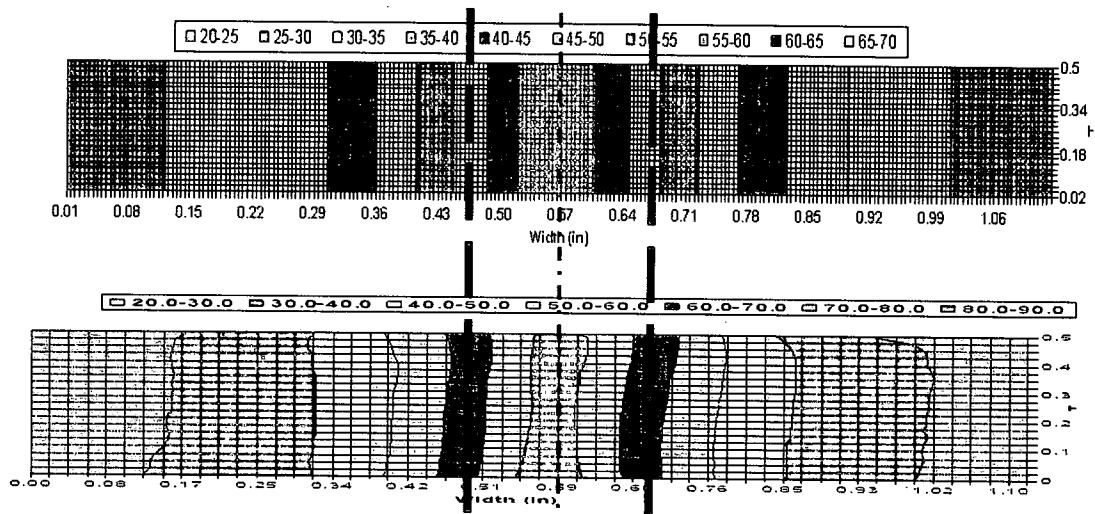


Figure 4.18: Comparison of Surface Temperature Distributions; Carbon Fiber at 0.5 Amps 32Ω/m for 300 seconds in Celsius

carbon fiber tow as a resistive heating element proved the most effective in terms of the amount of power that was required to resistively heat the SMP in an acceptable amount of time. Additionally, the carbon fiber tow effectively heated the largest diameter of SMP above its transition temperature.

Chapter 5

Structural Skin Concept

This chapter discusses the structural skin solution investigated in this research. The skin is based upon a sandwich structure utilizing the representative SMP. A discussion on structural modulus as part of the skin solution based upon the mechanics of cellular structures is given and how cellular structures are integrated into this project. Tensile testing with regard to the test specimen design, test setup and results are presented and discussed. Fiber distribution to thermally activate the SMP, in part of the tensile testing, was derived from the work presented in the previous chapter. Processing and testing results of skin solutions are presented and discussed.

5.1 Description and characteristics of sandwich

Approximately the same weight sandwich and monocoque construction concepts are compared. The basic sandwich concept consists of two faces and a core. Figure 5.1(a) shows a representative cross section per unit width of a sandwich construction. A structural sandwich has 2 faces, usually the same in thickness and material, and a core. Figure 5.1(b) shows a representative cross section per unit width of a monocoque construction. Monocoque describes a method of construction that utilizes the faces of the sandwich construction without the core to perform

a structural function. Comparing the sandwich and the monocoque constructions, while employing the same materials at approximately the same weight, yields that the sandwich construction has higher overall buckling loads, lower tangential deflections, and higher vibration natural frequencies [19]. In addition to having control of in-plane deformation, out-of-plane deformation can be managed as well.

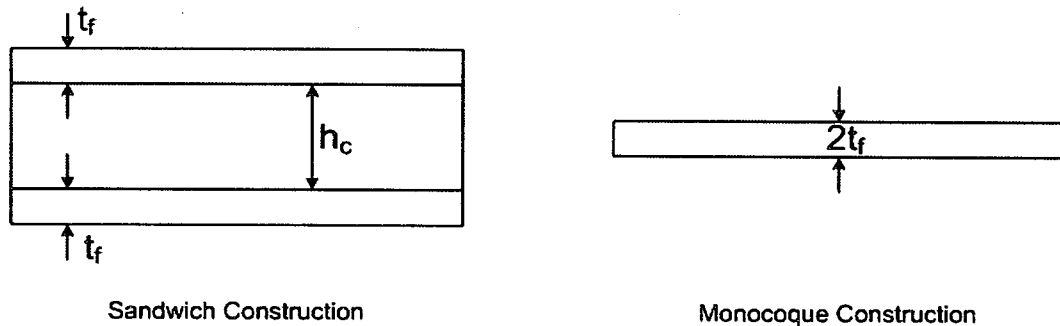


Figure 5.1: Cross Section of (a) Sandwich construction and (b) Monocoque construction

The basic sandwich concept provides for compression on the top face sheet, tension on the bottom face sheet, and shear throughout the honeycomb core in the middle. This concept allows for the different portions of the sandwich construction to be tailored to the loads. Therefore, while utilizing the SMP as the sandwich core is good for controllable stiffness allowing for the desired in-plane deformation, it has weak out-of-plane properties. Since, the primary concern was the deformation of the core this allows for other materials to be utilized as the sandwich face. However, due to processing issues, the entire test specimen was manufactured as one utilizing SMP at the sandwich face.

5.2 Mechanics of cellular structures

Cellular structures were utilized to facilitate in-plane deformation while minimizing the out of plane deformation. The basic idea of cellular structures was to capitalize on the idea of adding more structure to a sandwich construction, while minimizing the weight added. In this section, the basic behavior of the cellular structure was sought, including modulus and deformation values, and other changes that could be seen in experimentation.

A tailored structural solution was sought utilizing a cellular structure and a facesheet, to enable a more effective out-of-plane reinforcement while continuing to allow the minimal force required for in-plane deformation. In this study, identical prismatic cells, or honeycombs, were utilized since they have a regular geometry. Figure 5.2 shows a two-dimensional diagram of a hexagonal cell. The X_1 and X_2 directions are both utilized for the in-plane discussions, and the third dimension, X_3 , which is not shown is referenced for the out-of-plane discussions. Properties can be expressed and predicted via established mechanics principles. The in-plane strength and stiffness values of a hexagonal honeycomb are the lowest due to the bending of the hexagonal cell walls. These cell walls bend because of stresses, which are induced within this plane. Specifically, with regard to hexagonal honeycomb, the out-of-plane strength and stiffness values are much larger than the in-plane values, due to the requirement for compression or axial extension of the hexagonal cell walls to enable deformation [26].

When a uniaxial in-plane force is applied to a hexagonal honeycomb structure, the structure behaves in a linear-elastic manner, causing the cell walls to bend. Equations 5.1 and 5.2 are utilized to calculate the modulus of the hexagonal honeycomb structure in the X_1 and X_2 direction under uniaxial loading conditions.

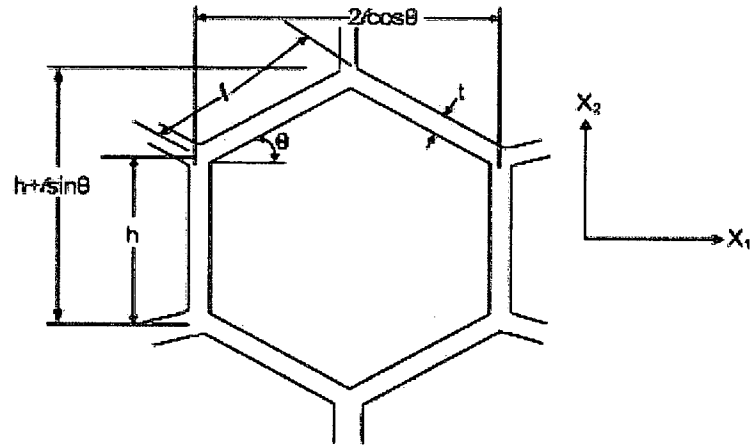


Figure 5.2: Diagram of the Undeformed Honeycomb

$$E_1 = \left(\frac{t}{l}\right)^3 \frac{\cos \Theta}{\left(\frac{h}{l} + \sin \Theta\right) \sin^2 \Theta} \quad (5.1)$$

$$E_2 = \left(\frac{t}{l}\right)^3 \frac{\left(\frac{h}{l} + \sin \Theta\right)}{\cos^3 \Theta} \quad (5.2)$$

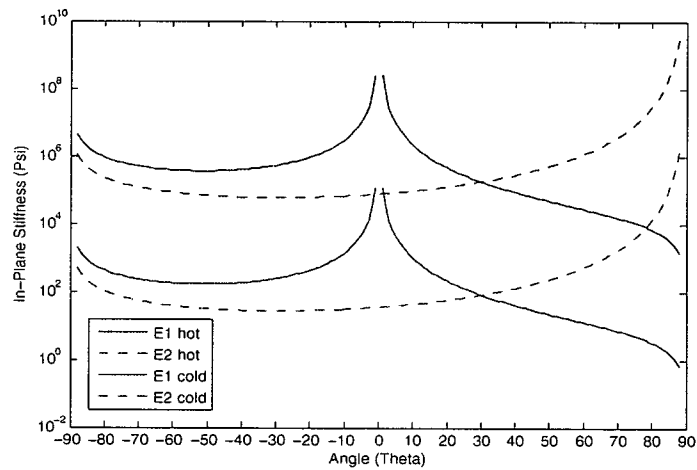


Figure 5.3: Plot of E1 and E2 for In-plane stiffness versus angle

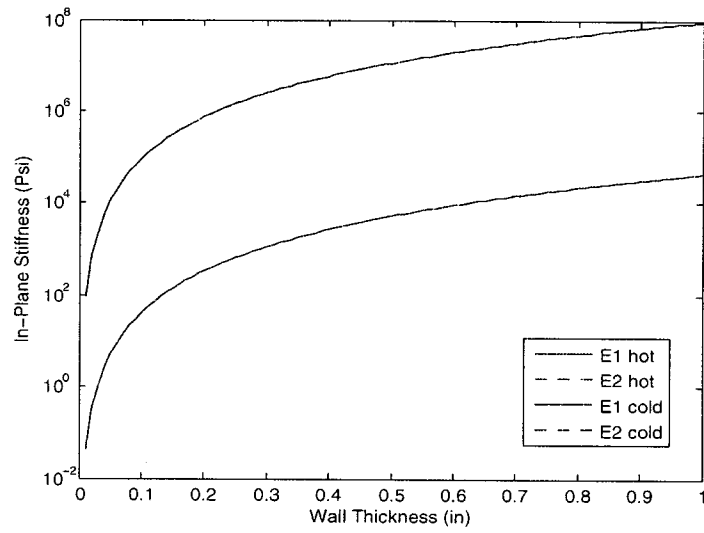


Figure 5.4: Plot of E1 and E2 for In-plane stiffness versus cell wall thickness

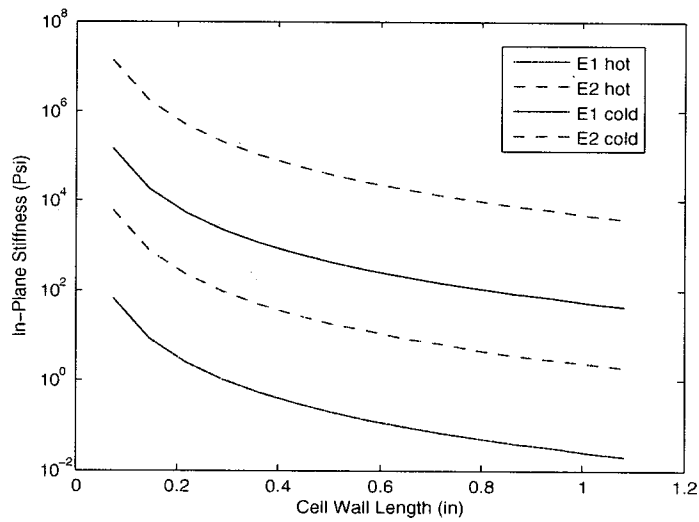


Figure 5.5: Plot of E1 and E2 for In-plane stiffness versus cell wall length

To understand the basic behavior of the honeycomb structures the modulus in the X_1 and X_2 direction was examined in relation to interior angle, cell wall thickness, and cell wall length. Average values of the experimental dynamic modulus of SMP were utilized in the calculations, and are detailed in the next section. Figure 5.3 shows how the X_1 and X_2 direction moduli behave as the interior cell angle varies. The negative cell angles indicate an auxetic cell structure while the positive cell angles indicate a hexagonal cell structure. Figure 5.4 shows how increasing the cell wall thickness increases the in-plane stiffness thus requiring greater power to deform the material. However, Figure 5.5 shows that as the cell wall length is increased, or the hexagonal cell is enlarged, the in-plane stiffness decreases requiring less power to deform the material.

5.3 In-Plane Stiffness Model

The previous section discusses the behavior of the cellular structure itself. This section investigates the behavior of the face sheet-cellular structure combination. As mentioned before, due to processing issues, only one face sheet is included. Utilizing the DMA data that was acquired and discussed previously, values of the dynamic modulus of the SMP were determined. The average of the dynamic modulus value in the stiff state is 120 ksi with experimental error of +43ksi/-20ksi and the average of the value in the soft state is 60ksi with experimental error of +10ksi/-30ksi. These values were plugged into Equations 5.1 and 5.2 and calculated in conjunction with equation 5.3.

$$E_{\text{total}} = V_{\text{face}}E_{\text{face}} + V_{\text{honeycomb}}E_{\text{honeycomb}} \quad (5.3)$$

The modulus which was utilized in the model was determined using a rule of mixtures as shown in equation 5.3. Therefore, using the volumes previously calculated, a percentage was determined for the facesheet and the honeycomb. The modulus values were acquired from the DMA data for the facesheet and the value of equation 5.1 for the cellular structure under uniaxial loading.

Three plots yielding the in-plane stiffness versus angle, the in-plane stiffness versus cell wall thickness, and the length change versus angle change were completed. The latter two plots change with the hexagonal size, while the first plot changes with cell wall thickness, which varied within the equation. A representative set of results is shown for a neat resin face sheet-honeycomb specimen of 1/4 inch hexagonal cells with 1/8 inch cell walls in the following three figures. Figure 5.6 shows how the in-plane stiffness changes versus the angle in the soft and stiff moduli. Figure 5.7 displays how the in-plane modulus of the specimen is affected as the cell wall thickness increases. Additionally, Figure 5.8 gives a basic idea of how the length and angle change as the specimen is uniaxially deformed. This representative specimen of 1/4 inch hexagonal cells with 1/8 inch cell walls was manufactured and tested and will be discussed in later sections.

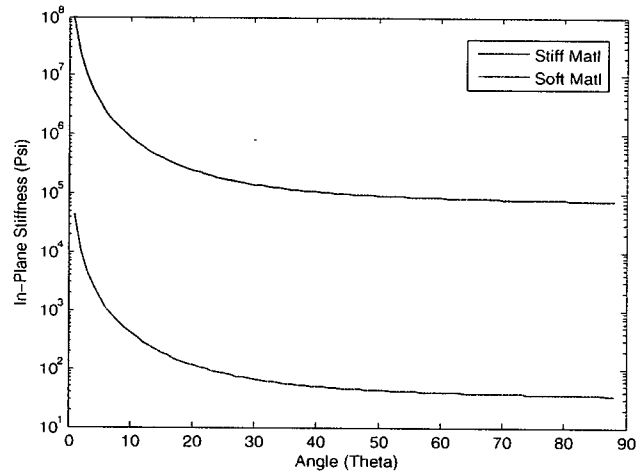


Figure 5.6: Plot of the 1/4 inch hexagonal cell with 1/8 inch cell walls In-Plane Stiffness versus Cell Angle

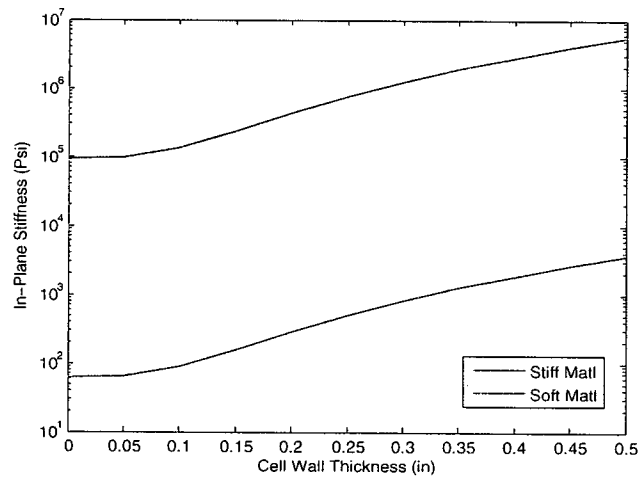


Figure 5.7: Plot of the 1/4 inch hexagonal cell In-Plane Stiffness versus Cell Wall Thickness

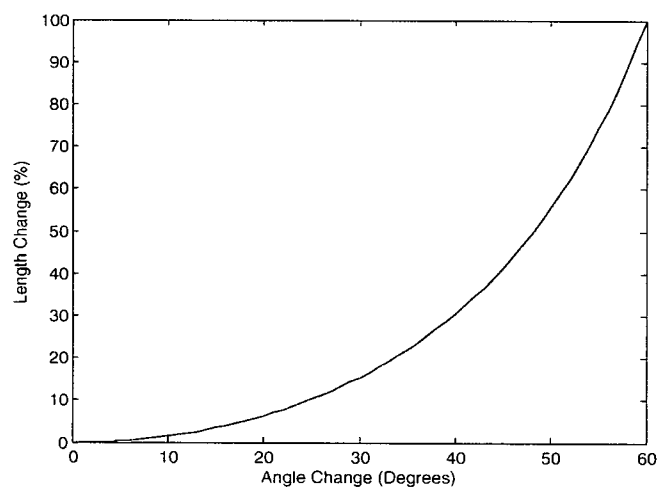


Figure 5.8: Plot of the 1/4 inch hexagonal cell Length Change versus Cell Angle Change

5.4 Specimen Design, Processing, and Testing

This section describes the tensile test specimen design that was utilized as detailed by an ASTM Test Standard, the manufacturing of these specialized test specimens and the test procedure. The purpose of this testing was to complete a resistively heated proof of concept for the structural skin concept.

5.4.1 Test Specimen Design

The test standard called out specimen dimensions based on test specimen total thickness of 0.28 inch to 0.55 inch [27]. The information from the test standard was used to set ratios based on the width of the narrow section. Figure 5.9 shows the drawn tensile specimen with 1/4 inch hexagonal cells and 1/8 inch cell walls. The tensile specimens were tested with the ASTM Standard Test Method for Tensile Properties of Plastics (D638-03). Per the standard, the test specimens were designed as Type III, which was determined based upon the expected thickness of 0.375 inch. Specimen dimensions were further driven by the availability of six point sockets to assist in the manufacturing of the mold and the width needed to contain a minimum of four hexes within the specimen. These drawings were completed to enable the placement of the hexes during manufacture of the mold.

Once the specimen size was determined, a mold corresponding to a specific tensile specimen was made. The representative size that was fabricated is the specimen which had 1/4 inch hexes with 1/8 inch cell walls shown. To effectively manufacture the honeycomb structure within the mold, Figure 5.9 was printed on clear translucent sheets. The translucent sheets were more durable than paper and provided the ability to cut out any part of the drawing with an Exacto knife if deemed necessary. When printed to size, the drawing came out as shown in

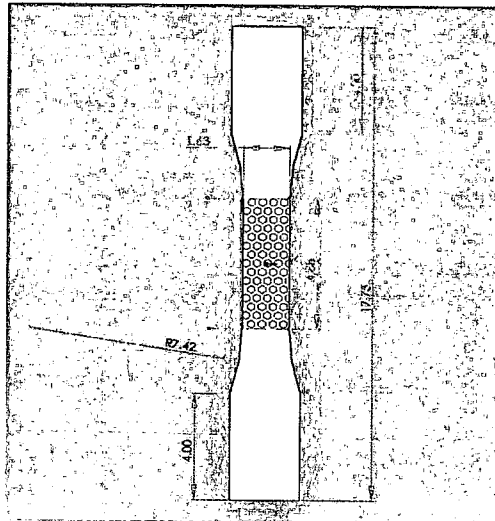


Figure 5.9: Diagram of the 1/4 inch hexagonal cells with 1/8 inch walls Tensile Specimen

Figure 5.10. Despite the ends of the specimen being cut off, their rectangular nature allowed for the template to still be used.

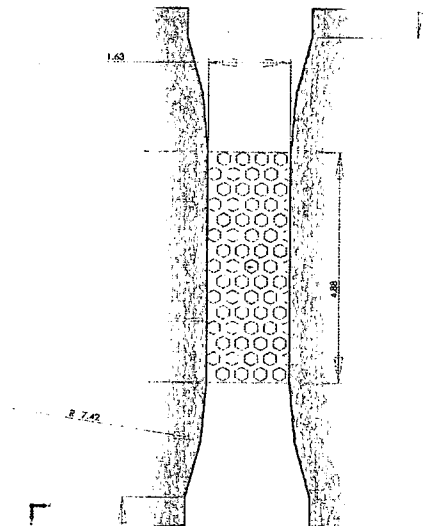


Figure 5.10: Printed template of the 1/4 inch cell with 1/8 inch walls Tensile Specimen

The printed translucent sheet was trimmed along the outer edge of the drawing providing most of the dogbone shape. This template was laid onto a 4 inch by 24 inch, 1/8 inch thick sheet of Viton® rubber. The dogbone shape was cut out of the Viton, thus providing the form to enclose the resin during cure as shown in Figure 5.11. The dogbone shape can be seen in the center of Figure 5.11, with a resin reservoir at each end to minimize defects during processing. Additionally, the placement of the carbon fiber tow seen in Figure 5.11 will be discussed later in this chapter.

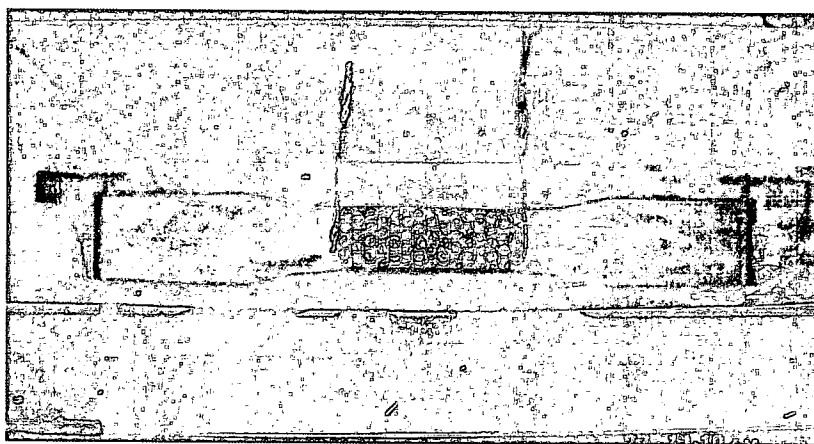


Figure 5.11: Carbon hex mold under construction

Figure 5.12 shows a closer view of the gauge length area of the mold within the dogbone test specimen. Hexes were then cut from Viton® rubber pieces 1/8 inch thick via dyes created with 6 point sockets machined down to provide a sharp edge. A uniform pressure was applied to the top of the sockets to cut as uniform a hex as possible. The hexes were then placed as accurately as possible onto the translucent sheet with rubber cement holding them in place. Initially, Viton® caulk was used to adhere the hexes in place in the mold. It was discovered, post cure, that the excess caulk reacted with the SMP resin during the cure cycle causing

excess voids across the gauge section of the specimen. Therefore, an alternate solution of stapling the hexes into the mold was utilized. The cross bar from the staples was removed and the finished product is shown in Figure 5.12. It is shown that the metal posts holding the hexes in place provide no impediment to the specimen.

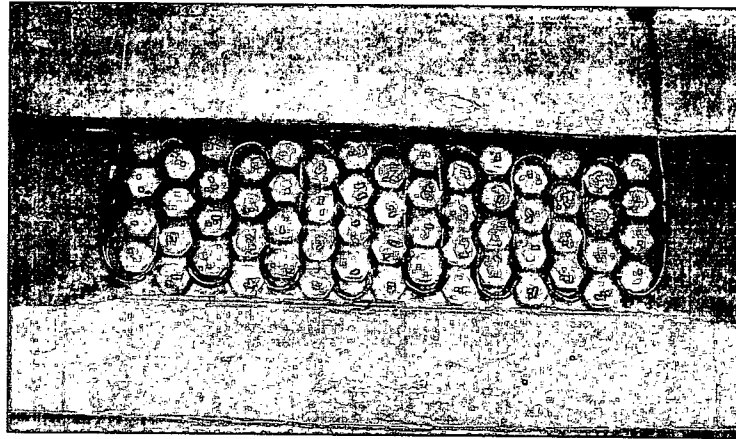


Figure 5.12: Carbon hex mold with Carbon Fiber tow weaved into the mold

Additionally, Figure 5.12 shows a carbon fiber tow already weaved between the hexes. For this particular specimen, via an understanding from the thermal analysis, weaving the carbon fiber tow between the hexes was determined appropriate because the diameter of resin resistively heated would overlap each other. It is important to note, that when the neat resin specimen was manufactured, the carbon fiber tow was not present. Once the dogbone mold was completely assembled, it was placed on a 24 in by 12 in plate of glass to maintain a flat surface as seen in Figure 5.11. Like the previous plaque molds, a second sheet of glass was placed on top of the mold and clamped into place. A channel that was previously cut into the end of the mold was utilized with a funnel to pour the SMP resin into the mold. Once full of resin, the channel was then sealed with the corresponding piece of Viton® rubber that was removed and clamped shut. The mold was then tipped

on its side and placed in an oven to be cured. The cured neat resin specimen is shown in Figure 5.13.

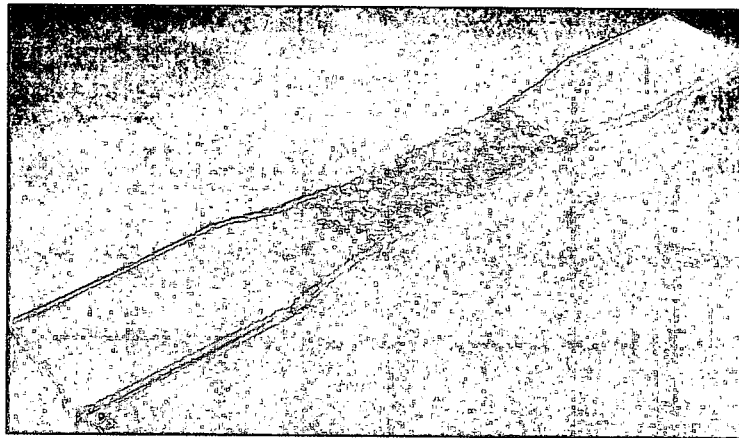


Figure 5.13: Neat resin 1/4 inch hex with 1/8 inch cell walls

An identical process was used to manufacture the dogbone test specimen with the carbon fiber embedded resistive heating element. The only alteration was prior to the pouring of the resin, a carbon fiber tow is secured in the mold. Figure 5.14 shows the cured resistive heating element test specimen with 1/4 inch hexagons.

5.4.2 Experimental Setup

To characterize the SMP sandwich structure, two different specimens were tested. The first specimen was referred to as the neat resin specimen, which had no resistive heating elements. This specimen was placed in an oven to obtain the desired higher than transition temperature yielding the low modulus. The second specimen was referred to as the carbon fiber specimen, which contained a single 6K carbon fiber tow weaved into the resin, thereby, providing an internal resistive

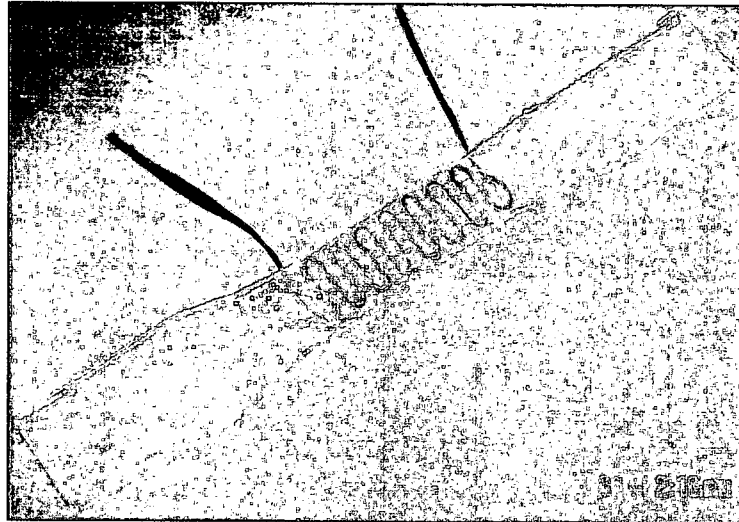


Figure 5.14: Carbon Fiber resistive heating elements woven into resin with 1/4 inch hex with 1/8 cell walls

heating element to obtain the desired higher than transition temperature yielding the low modulus.

Figure 5.15 shows the test setup which was used. The figure shows the oven, with a maximum reachable temperature of 1600°F, to the center left of the picture, which was utilized to heat the neat resin specimen. Figure 5.15 also shows the DC power supply, near the center of the picture, which was used to supply power to the resistive heating element during the second test. Additionally, Figure 5.15 visualizes the thermocouple and its placement, the laser extensometer, MTS machine, controller, and the computer that were utilized to acquire data. The electro-mechanical MTS brand Alliance RT/10 machine utilized was screw driven with a 2.2 kip load cell, hand controller, and data acquiring computer software. Electronic Instrument Research Model LE-05 laser extensometer provided precision strain measurement up to five inches. The laser extensometer required two reflective

tabs on the specimen to measure strictly linear displacement. A better view of the placement of these tabs can be seen in the next section in Figure 5.20.



Figure 5.15: Tensile Test Setup

The test procedure that was utilized to perform the tensile tests is shown below.

- (1) At room temperature, displace the test specimen to 0.03 in at a rate of 0.3 in/min per the ASTM standard D638-03 and returned to zero displacement. This acquires the undeformed cold modulus.
- (2) Heated the specimen to 75°C and displace 0.03 in at a rate of 0.3 in/min again and returned to zero displacement. This acquires the undeformed heated modulus.
- (3) Displace the test specimen 2 inches at a rate of 2 in/min, stop and hold. Cool at the elongated state to room temperature. This acquires the heated modulus versus Theta (Interior Hex Angle) data set.

- (4) At room temperature, displace the test specimen to 0.03 in at a rate of 0.3 in/min. This acquires the deformed cold modulus.
- (5) Ungrip one end of the test specimen (no load), and heat to 75°C allowing the specimen to return to it's original shape.

5.4.3 Results

Stress versus strain acquired from the tensile test is plotted utilizing the calculated cross sectional area of the specimen and the initial extensometer gauge length. Figure 5.16 shows a representative set of data points taken utilizing the Neat Resin tensile specimen during Part 2 of the test. Appendix D gives the full stress versus strain data.

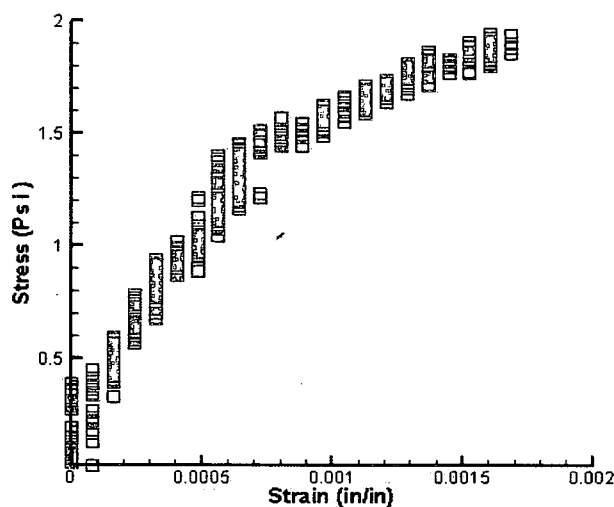


Figure 5.16: Part 2 Stress versus Strain Response of Neat Resin Test Specimen above T_g

Figure 5.17 shows the results of the full test procedure that was run to acquire the data. The two higher modulus points at approximately 10^5 Psi were acquired

while the test specimen was in the stiff state. These data points are acquired from a linear curve produced when displacing the test specimen 0.03 in at a rate of 0.2 in/min. The remaining data points in Figure 5.17 are from testing while the specimen was in the soft state.

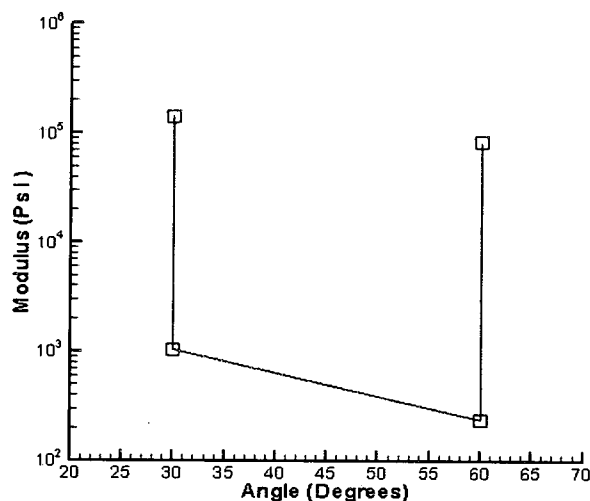


Figure 5.17: Tensile Test Data of the Neat Resin Specimen

To get an idea of how the test specimen behaves, Figure 5.18 shows the experimental data points overlaid on the analytical data. It is seen that the analytical and experimental values for the specimen in the stiff state matches well, however, the values for the specimen in the soft state are off by approximately an order of magnitude. To further understand the behavior of the specimen, Figure 5.19 shows the neat resin test specimen post-completion. As can be seen in the figure, a temperature gradient was created due to the design of the test setup. Therefore, the test was completed while the top half of the test area was transitioned above the glass transition temperature and the bottom half was not. This test provided a baseline for future in-plane sandwich structure tests.

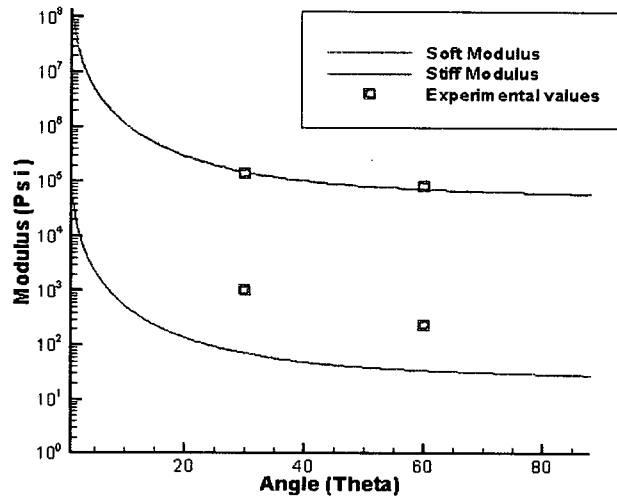


Figure 5.18: Neat Resin Test Specimen with Experimental and Analytical Data Points

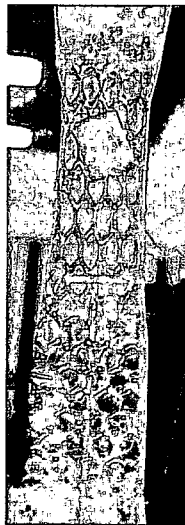


Figure 5.19: Neat Resin Test Specimen Post-Test

A second test specimen with a carbon fiber tow, to be used as a resistive heating element, weaved among the hexes was tested. A power input of 0.5 Amps

and 33.3 Volts was placed across the carbon fiber which took seven minutes to reach the 65°C glass transition temperature. The specimen was allowed to stabilize at 71.6°C prior to running the test. Limited data was acquired during this test due to stoppage at the end of the 3rd step of the test procedure. The test was stopped because a tear occurred at part of the tow at the surface of the facesheet, as seen in Figure 5.20.

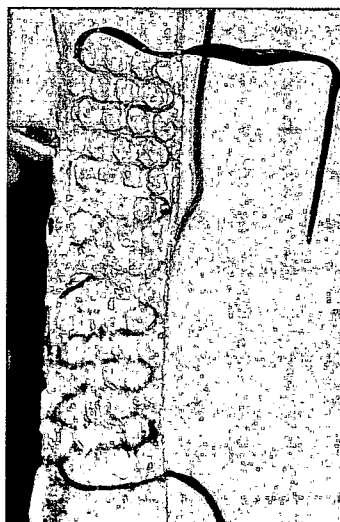


Figure 5.20: Carbon Fiber Heating Element Tensile Test Specimen Post-Test

The behavior of the material during deformation was also considered. Figure 5.20 shows the uniform deformation that occurred in comparison to the neat resin specimen, meaning that the SMP around the grips did not transition providing anchoring points while the gauge length, which included the hexes, transitioned more uniformly due to the resistive heating elements embedded in the resin. Recall, in comparison, Figure 5.19 shows that the top half of the gauge length deformed. Figure 5.20 also shows that a tear at the face of the specimen occurred. It is seen

that the tear developed and propagated along a carbon fiber tow near the surface of the sandwich face.

Figure 5.21 shows the stress versus strain response of the specimen that was resistively heated with a carbon fiber tow. However, noticing that the stress begins below 0 Psi indicates that something went wrong with this particular test, since the load was zeroed prior to any testing performed.

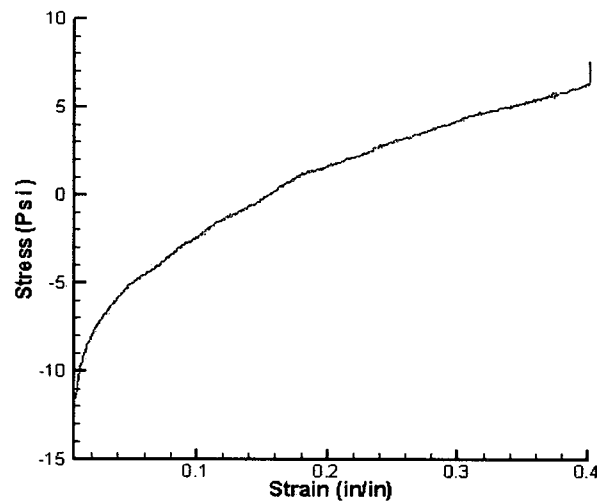


Figure 5.21: Part 3 Stress versus Strain Response of Carbon Fiber Test Specimen above T_g

The moduli at angles of 30 degrees and 60 degrees are calculated with the acquired experimental data shown in Figure 5.22. Figure 5.22 also shows the discrepancy in testing in that the moduli are an order of magnitude lower than the neat resin specimen. However, despite the manufacturing issues for the carbon fiber specimen that manifested themselves during testing, this tensile test demonstrated that a SMP sandwich structure is capable of being resistively heated and deformed.

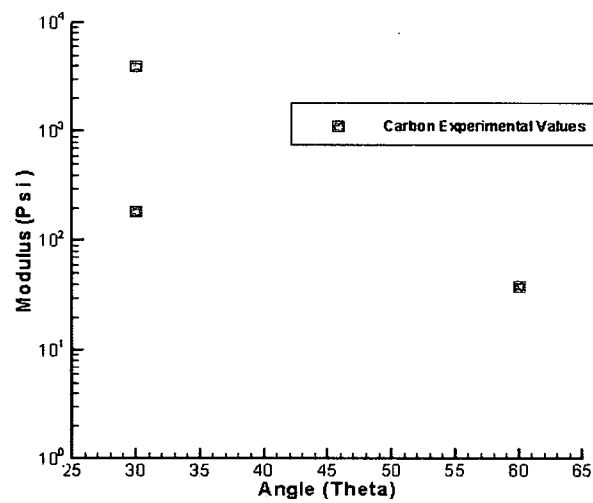


Figure 5.22: Carbon Fiber Test Specimen Experiment Data Points

5.5 Chapter Summary

This chapter discussed the development and testing of the flexible structural skin concept. Sandwich construction was determined to be beneficial and utilized within the solution. This particular sandwich construction was completed via a honeycomb cellular structure that was examined in terms of its mechanics. The minimal fiber distribution determined in the previous chapter was utilized in the test specimen construction. Test specimens were designed to determine the effect a cellular structure has on the force required to perform in-plane deformations. Specimen fabrication consisted of all SMP due to manufacturing issues and potential facesheet bonding issues with the use of other materials. The mechanics of cellular structures was understood from an experimental and analytical perspective.

Chapter 6

Summary and Conclusions

6.1 Thesis Summary

This project investigated some morphing wing skin alternatives that would allow large deformation of aircraft structures in a highly controllable fashion. This investigation targeted the development of flexible materials that, when combined with mechanized structures, can enable large rigid body deformations of aircraft structures while maintaining its aerodynamic shape. The research focused on maximizing in-plane deformation, and minimizing in-plane force required to deform the material, while minimizing out-of-plane deflection. A representative SMP was investigated with a sandwich concept involving many challenges including processing, material testing, thermal activation, sandwich processing, and testing. The SMP material was selected as a flexible skin solution because the material can be manipulated and cooled into a variety of shapes. This SMP material behaves such that a required input energy, external or internal, is applied sending the material to its transition temperature, and a modulus change is activated. Thereby, when the skin is reinforced with mechanized structures this enables large in-plane changes while maintaining out of plane stiffness.

A concept utilizing an embedded reinforcing fiber within the SMP was investigated. This multi-functional fiber serves as a reinforcing element in addition to

providing the means to activate the material response via resistive heating. The manufacturing process was developed to create test specimens using the thermally activated SMP. This process was confirmed utilizing a DMA test setup at varying strain rates. Several material activation methods were investigated utilizing thermal imaging and finite difference modeling to determine the resistive heating effectiveness and minimum spacing requirement of a heating element. A carbon fiber tow proved the most effective solution, based upon the amount of power that was required to resistively heat the SMP and the effective area heated. To improve upon the design, cellular structures were investigated in terms of an out-of-plane reinforcement, thereby providing a sandwich construction.

The structural skin concept integrates a two layer solution consisting of a cellular structure and a smooth continuous layer. To resistively heat the SMP, carbon fiber tows were embedded in the structural skin solution, thereby thermally activating the material and decreasing the modulus providing large deformations for morphing aircraft skins. The cellular structure provided the desired minimal increase in in-plane force required for deformation. Thus, this solution meets some of the basic multi-functional skin criteria and is deemed as a realistic approach.

6.2 Future Work

Recommended future work includes additional building, testing, and characterization of the cellular skin concept utilizing different configurations. One of the configurations suggested to include in retesting is the specimen with a carbon fiber tow utilized as the resistive heating element. Additionally, future mechanical test setups should integrate the capacity to apply an out-of-plane load utilizing distributed pressure via an air bladder with a simulated wing structure underneath the

skin specimen, providing a more accurate representation of how the skin would behave under flight conditions. Other alternatives to explore during future work are an auxetic cell structure, which offers a negative Poisson's ratio during deformation, and a deeper honeycomb structure thereby providing more stiffness to the construction.

Another concept to consider in future work is a triaxial weave carbon fiber fabric [28] to utilize as the resistive heating element. This fabric would provide a multi-functional fiber element supplying a more distributed out-of-plane reinforcement and make available a more uniformly distributed resistive heating element. Additionally, a phase change material could be examined in the future with the aim of utilizing the material as a heat sink and source, thereby requiring less power to repetitively transition the skin. These improvements and alterations would make a SMP skin concept a more feasible and effective solution for large deformation morphing aircraft skins.

Bibliography

- [1] Inc Dynalloy. Flexinol® technical data. <http://www.dynalloy.com/TechnicalData.html>.
- [2] Jr. John D. Anderson. Fundamentals of Aerodynamics. McGraw-Hill Higher Education, 4th edition, 2007.
- [3] Richard Hardy Ronald W. DeCamp and Douglas K. Gould. Mission adaptive wing. In SAE International Pacific Air and Space Technology Conference, Melbourne, Australia, 1987.
- [4] E. White J. Dunne, D. Pitt and E. Garcia. Ground demonstration of the smart inlet. In AIAA 41st Structures, Structural Dynamics, and Materials Conference, Atlanta, Georgia, April 2000.
- [5] J. N. Kudva. Overview of the darpa smart wing project. Journal of Intelligent Material Systems and Structures, 15:261–267, April 2004.
- [6] Robert Sebastian Bortolin. Characterization of shape memory polymers for use as a morphing aircraft skin material. Master's thesis, University of Dayton, Dayton, OH, August 2005.
- [7] Brian Sanders Jason Bowman and Terrance Weisshaar. Identification of military morphing aircraft missions and morphing technology assessment. In Smart Structures and Integrated Systems, San Diego, CA, 2002. Proceedings from the SPIE Smart Materials and Structures Conference.
- [8] M.P. Sepe. Dynamic Mechanical Analysis for Plastics Engineering. William Andrew Publishing/Plastics Design Library, online version edition, 1998.
- [9] J.N. Kudva. Overview of the darpa/afri/nasa smart wing phase 2 program. Journal of Intelligent Material Systems and Structures, 15:261–267, 2004.
- [10] P.A. Toensmeier. Morphing aircraft could bring multi-role capability to next generation aircraft. Aviation Week, May 2005.

- [11] C. Henry and G. McKnight. Cellular variable stiffness materials for ultra-large reversible deformations in reconfigurable structures. In William D. Armstrong, editor, Smart Structures and Materials 2006: Active Materials: Behavior and Mechanics, volume 6170. SPIE, 2006.
- [12] Dr. Geoffrey McKnight. Multi-role, kinematically active materials for reconfigurable structures. Final technical report, HRL Laboratories, LLC, 3011 Malibu Canyon Road, Malibu, CA 90265, August 19 2005.
- [13] Tat Hung Tong. Shape memory styrene copolymer. United States Patent, July 6 2004. Patent No. 6,759,481.
- [14] Emily A. Snyder Ernie Havens and Tat Hung Tong. Light-activated shape memory polymers and associated applications. In Edward V. White, editor, Smart Structures and Materials 2005: Industrial and Commercial Applications of Smart Structures Technologies, volume 5762, pages 48–55, Bellingham, WA, 2005. SPIE.
- [15] Jr. David A. Perkins, John L. Reed and Ernie Havens. Morphing wing structures for loitering air vehicles. Cornerstone Research Group, Inc., 2750 Indian Ripple Road, Dayton, OH 45440, April 19-22 2004. AIAA/ASME/AHS/ASC Structures, Structural Dynamics & Materials Conference.
- [16] Naseem A. Munshi Fred Beavers Ken Gall, Martin Mikulas and Michael Tupper. Carbon fiber reinforced shape memory polymer composites. Journal of Intelligent Material Systems and Structures, 11, November 2000.
- [17] Dr. Geoffrey McKnight. Research in multi-role, kinematically active materials for reconfigurable structures. Final report, HRL Laboratories, LLC, 3011 Malibu Canyon Road, Malibu, CA 90265, September 2005.
- [18] Kenneth E. Evans and Andrew Alderson. Auxetic materials: Functional materials and structures from lateral thinking! Advanced Materials, 12(9):617–628, 2000.
- [19] P.E. Jack R. Vinson, Ph.D. The Behavior of Sandwich Structures of Isotropic and Composite Materials. Technomic Publishing Company, Inc., Lancaster, PA, 1999.
- [20] Flying dragon. *http : //en.wikipedia.org/wiki/Flying_dragon*, November 7 2006.
- [21] Tim R. Roberts Sean P. Cullen and Tat H. Tong. Studies of shape memory behavior of styrene based network copolymers. In Proceedings of the First World Congress on Biomimetics, Albuquerque, New Mexico, December 9-11 2002. Proceedings of the First World Congress on Biomimetics.

- [22] Brian S. Mitchell. An Introduction to Materials Engineering and Science: For Chemical and Materials Engineers. John Wiley & Sons, Inc., New York, 2004.
- [23] William Ragland Edward M. Silverman Hsiao-hu Peng Karla L. Strong Thao Gibson, Brian Rice and David Moon. Formulation and evaluations of carbon nanofiber-based conductive adhesives. Technical report, Air Force Research Labs, Materials and Manufacturing Directorate, Wright-Patterson AFB, OH.
- [24] Frank P. Incropera and David P. DeWitt. Fundamentals of Heat and Mass Transfer. John Wiley & Sons, New Jersey, 2002.
- [25] Alvin Hudson and Rex Nelson. University Physics. Harcourt Brace Jovanovich, Inc., New York, 1982.
- [26] Lorna J. Gibson and Michael F. Ashby. Cellular Solids: Structure and Properties. Cambridge University Press, Cambridge, 2nd edition, 1997.
- [27] D638-03: Standard test method for tensile properties of plastics. ASTM International, 2003.
- [28] Omer Soykasap Ahmad Kueh and Sergio Pellegrino. Thermo-mechanical behaviour of single-ply triaxial weave carbon fibre reinforced plastic. In Karen Fletcher, editor, ESA SP-581: Spacecraft Structures, Materials and Mechanical Testing 2005, Noordwijk, The Netherlands, May 10-12 2005. Department of Engineering, University of Cambridge, Trumpington Street, Cambridge, CB2 1PZ, U.K.
- [29] Robert M. Jones. Mechanics of Composite Materials. Hemisphere Publishing Corporation, New York, 1975.
- [30] James M. Whitney. Structural Analysis of Laminated Anisotropic Plates. Technomic Publishing Co., Inc., Lancaster, PA, 1987.
- [31] Erwin Kreyszig. Advanced Engineering Mathematics. John Wiley & Sons, New York, 5th edition, 1983.
- [32] Robert J. Schilling and Sandra L. Harris. Applied Numerical Methods for Engineers: Using Matlab and C. Brooks/Cole: Thomson Learning, Pacific Grove, CA, 2000.
- [33] J. C. Halpin. Revised Primer on Composite Materials: Analysis. Technomic Publishing Company, Inc., Lancaster, PA, 1984.
- [34] Dale A. Anderson John C. Tannehill and Richard H. Pletcher. Computational Fluid Mechanics and Heat Transfer. Taylor & Francis, Philadelphia, PA, 2nd edition, 1997.

- [35] Gerald W. Recktenwald. Numerical Methods with Matlab: Implementations and Applications. Prentice Hall, New Jersey, 2000.
- [36] Anthony Kelly Ramesh Talreja, Jan-Anders E. Manson and Carl Zweben, editors. Polymer Matrix Composites. Elsevier Science Ltd., New York, 2001.
- [37] Frederik J. Plantema. Sandwich Construction: The Bending and Buckling of Sandwich Beams, Plates, and Shells. John Wiley & Sons, Inc., New York, 1966.
- [38] Ronald F. Gibson. Principles of Composite Material Mechanics. McGraw Hill Custom Publishing, Boston, 1994.
- [39] M. Necati Özisik. Heat Conduction. John Wiley & Sons, Inc., New York, 2nd edition, 1993.
- [40] Jr. Theodore L. Brown, H. Eugene LeMay and Bruce E. Bursten. Chemistry: The Central Science. Prentice Hall, New Jersey, 8th edition, 2000.
- [41] Naseem A. Munshi Erik R. Abrahamson, Mark S. Lake and Ken Gall. Shape memory mechanics of an elastic memory composite resin. Journal of Intelligent Material Systems and Structures, 14, October 2003.
- [42] Norihito Ohsako Takeru Ohki, Qing-Qing Ni and Masaharu Iwamoto. Mechanical and shape memory behavior of composites with shape memory polymer. Composites Part A: applied science and manufacturing, pages 1065–1073, 2004.
- [43] Hexcel Composites. Magnamite®as4 carbon fiber: Product data. *http : //www.hexcel.com/NR/rdonlyres/5659C134 - 6C31 - 463F - B86B - 4B62DA0930EB/0/Magnamite_A_S4.pdf*, October 2005.
- [44] Flying dragon. *www.encyclopedia.com/doc/1E1 - flyingdr.html*, 2006.
- [45] Chris Martin Brian Sanders and Dave Cowan. Aerodynamic and aeroelastic characteristics of the darpa smart wing phase ii wind tunnel model. In Anna-Maria R. McGowan, editor, Smart Structures and Materials 2001: Industrial and Commerical Applications of Smart Structures, volume 4332, pages 390–398. SPIE, 2001.
- [46] Mary Frecker Deepak S. Ramrakhyani, George A. Lesieutre and Smita Bharti. Aircraft structural morphing using tendon-actuated compliant cellular trusses. Journal of Aircraft, 42(6):1615–1621, November-December 2005.
- [47] R. Sandström Z.G. Wei and S. Miyazaki. Review: Shape memory materials and hybrid composites for smart systems. Journal of Materials Science, 33:3763–3783, 1998.

- [48] Oliver Jünger Andreas Lendlein, Hongyan Jiang and Robert Langer. Light-induced shape-memory polymers. Nature, 434:879–882, April 14 2005.
- [49] Brian Sanders Jason Bowman and Terrance Weisshaar. Evaluating the impact of morphing technologies on aircraft performance. In 43rd AIAA/ASME/ASCE/AHS/ASC Structures, Structural Dynamics, and Materials Conference, Denver, Colorado, April 22-25 2002.
- [50] George Lesieutre Smita Bharti, Mary Frecker and Deepak Ramrakhyani. Optimal design of tendon-actuated morphing structures: Nonlinear analysis and parallel algorithm. In Ralph C. Smith, editor, Smart Structures and Materials 2005: Modeling, Signal Processing, and Control, volume 5757, pages 132–143, Bellingham, WA, 2005. SPIE.
- [51] Michael Thomas Kikuta. Mechanical properties of candidate materials for morphing wings. Master of science in mechanical engineering, Virginia Polytechnic Institute and State University, December 2003.

Appendix A

DMA Test Data

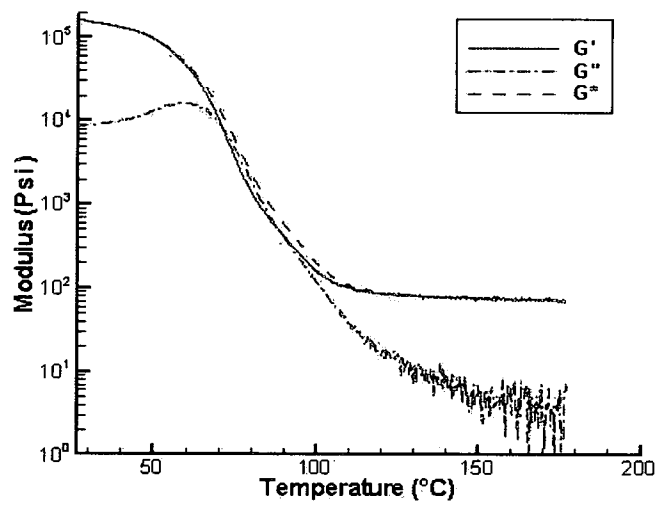


Figure A.1: Test specimen *SMP072905 - 2 - 6x6x0.125 - DMA1*

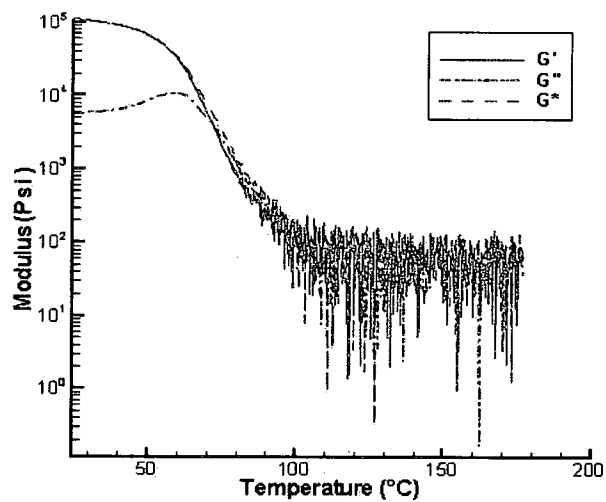


Figure A.2: Test specimen *SMP072905 - 2 - 6x6x0.125 - DMA2*

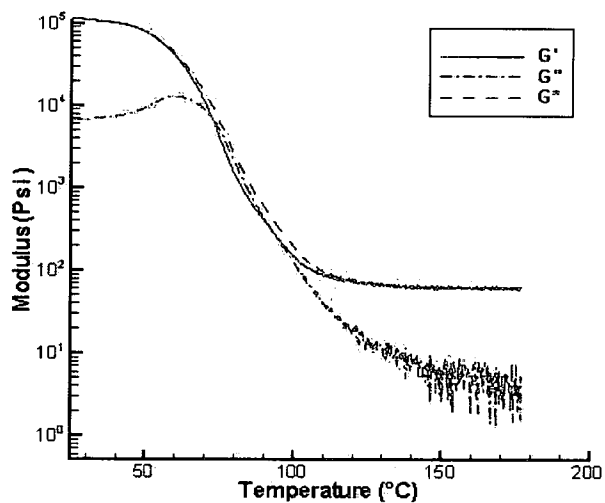


Figure A.3: Test specimen *SMP072905 - 2 - 6x6x0.125 - DMA3*

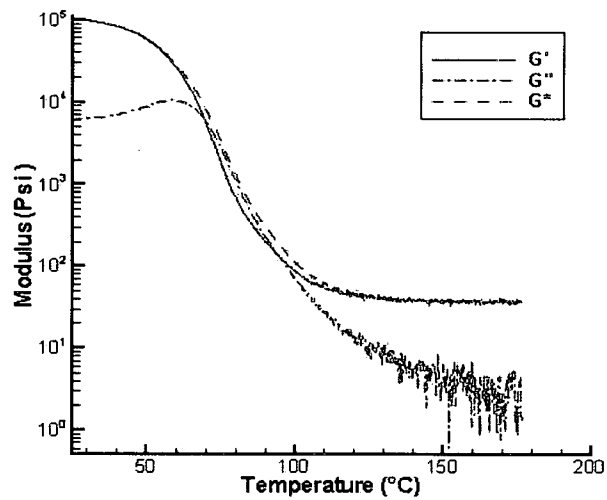


Figure A.4: Test specimen *SMP080505 - 2 - 6x6x0.125 - DMA1*

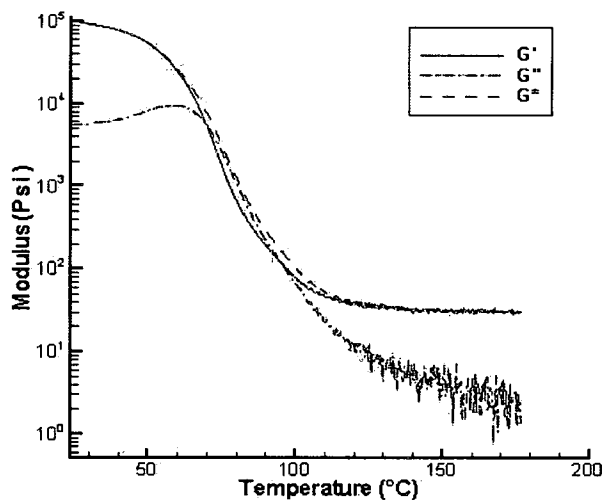


Figure A.5: Test specimen *SMP080505 - 2 - 6x6x0.125 - DMA2*

Appendix B

Finite Difference Figures

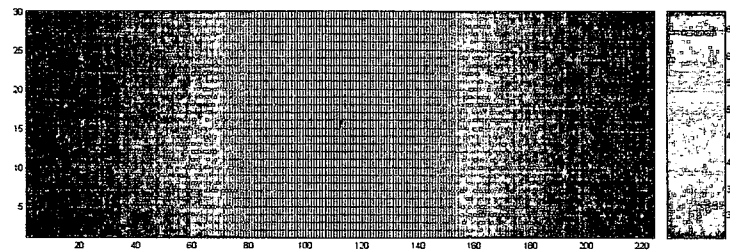


Figure B.1: Carbon Fiber at $0.4 \text{ Amps } 32\Omega/m$ for 300 seconds

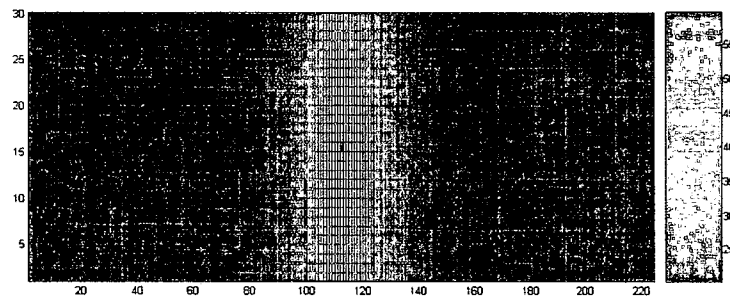


Figure B.2: Carbon Fiber at $0.5 \text{ Amps } 32\Omega/m$ for 30 seconds

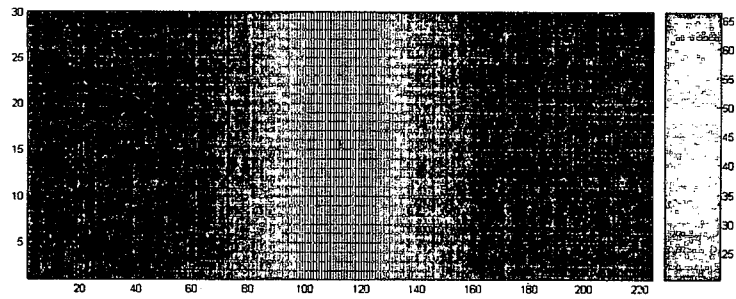


Figure B.3: Carbon Fiber at 0.5Amps $32\Omega/m$ for 60 seconds

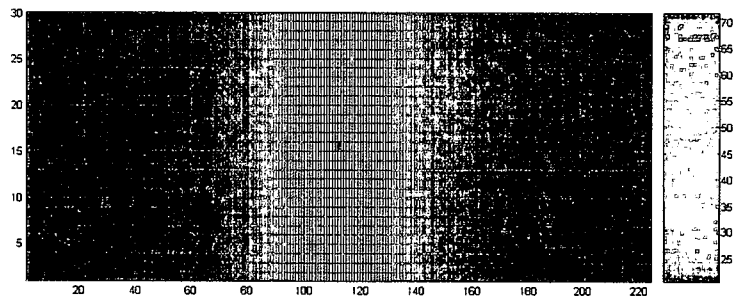


Figure B.4: Carbon Fiber at 0.5Amps $32\Omega/m$ for 90 seconds

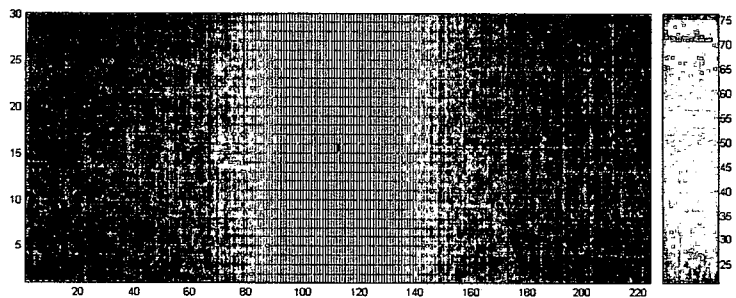


Figure B.5: Carbon Fiber at 0.5Amps $32\Omega/m$ for 120 seconds

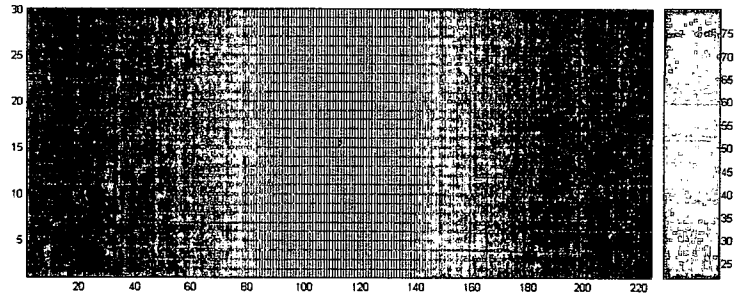


Figure B.6: Carbon Fiber at 0.5 *Amps* 32 Ω/m for 150 seconds

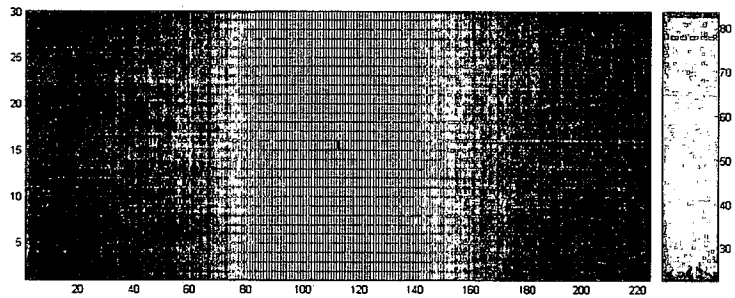


Figure B.7: Carbon Fiber at 0.5 *Amps* 32 Ω/m for 180 seconds

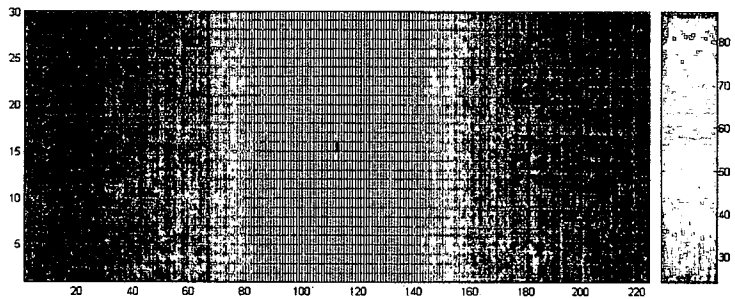


Figure B.8: Carbon Fiber at 0.5 *Amps* 32 Ω/m for 210 seconds

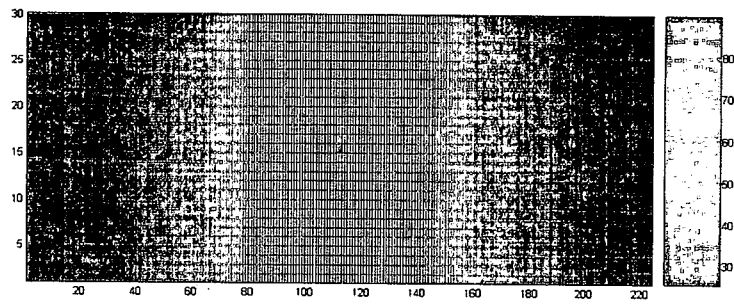


Figure B.9: Carbon Fiber at 0.5 *Amps* 32Ω/*m* for 240 seconds

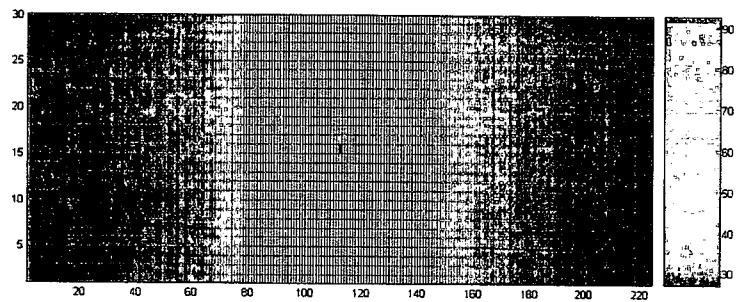


Figure B.10: Carbon Fiber at 0.5 *Amps* 32Ω/*m* for 270 seconds

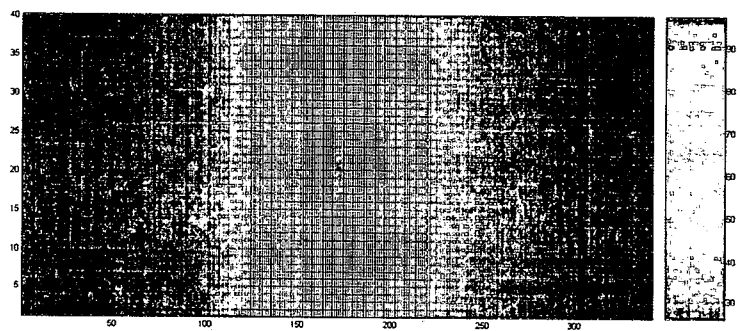


Figure B.11: Carbon Fiber at 0.5 *Amps* 32Ω/*m* for 300 seconds

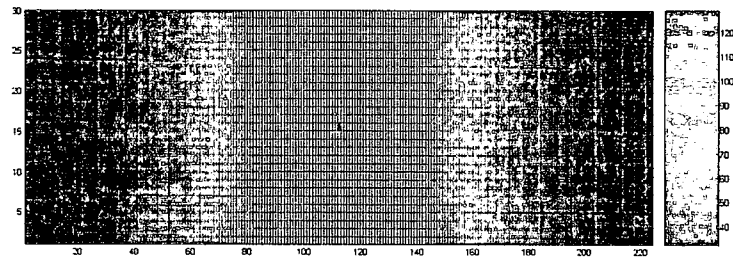


Figure B.12: Carbon Fiber at 0.6Amps $32\Omega/m$ for 300 seconds

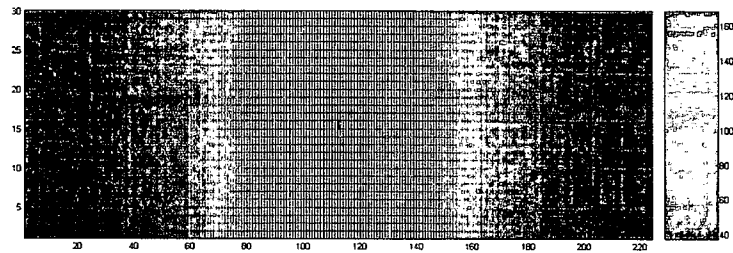


Figure B.13: Carbon Fiber at 0.7Amps $32\Omega/m$ for 300 seconds

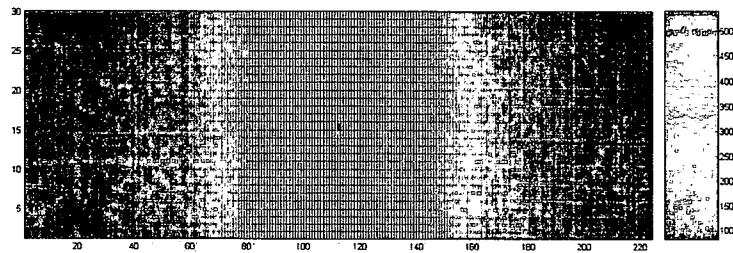


Figure B.14: Nichrome wire at 1.4Amps $27.95\Omega/m$ for 300 seconds

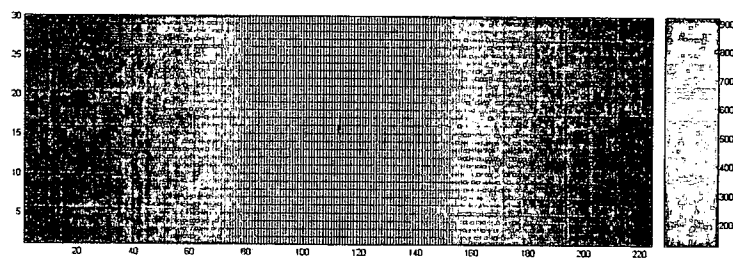


Figure B.15: Nichrome wire at 1.845Amps $27.95\Omega/m$ for 300 seconds

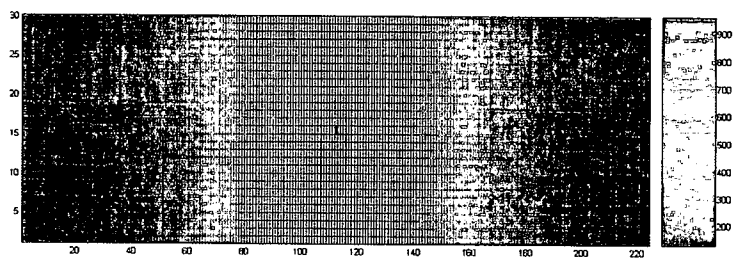


Figure B.16: Carbon Fiber at 1.885Amps $27.95\Omega/m$ for 300 seconds

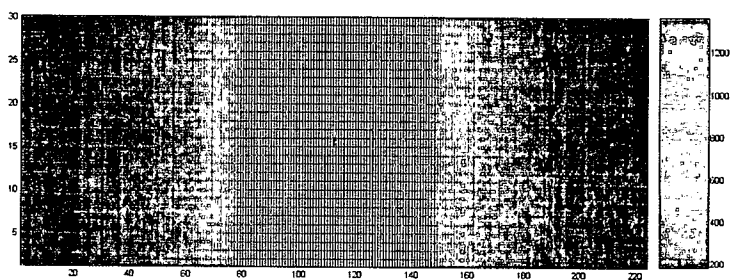


Figure B.17: Carbon Fiber at 2.255Amps $27.95\Omega/m$ for 300 seconds

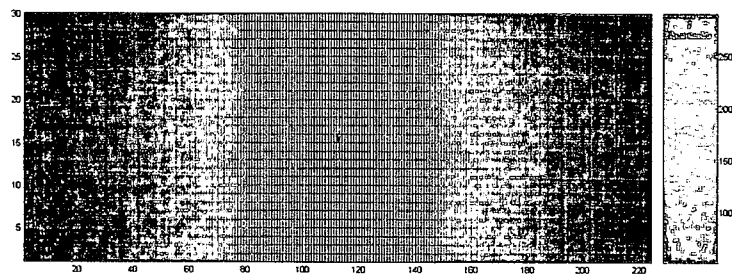


Figure B.18: SMA wire at 0.55 *Amps* $94.4\Omega/m$ for 300 seconds

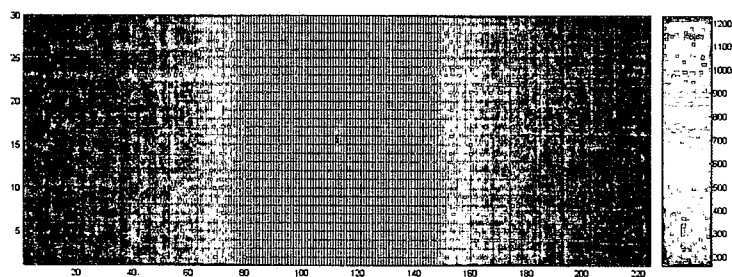


Figure B.19: SMA wire at 1.165 *Amps* $94.4\Omega/m$ for 300 seconds

Appendix C

Thermal Imaging Results

C.1 Infrared Images

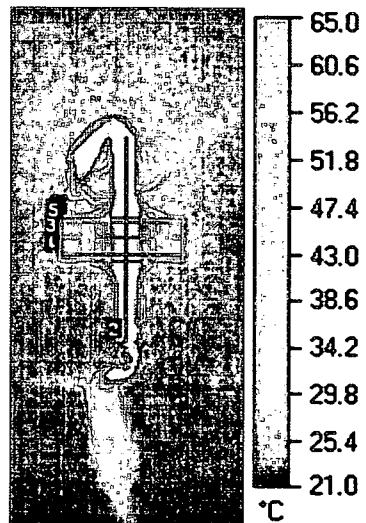


Figure C.1: Test 3 Short Carbon 1 0.5Amps

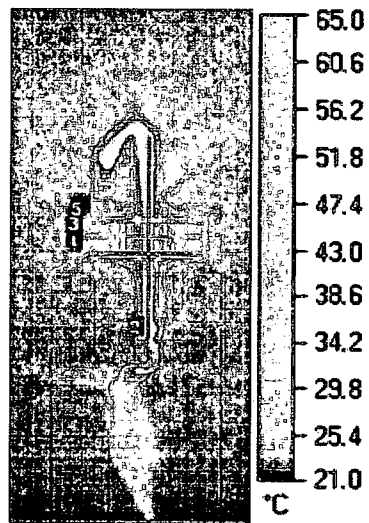


Figure C.2: Test 4 Short Carbon 1 0.4Amps

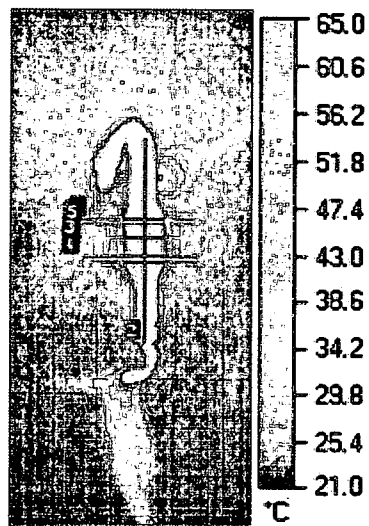


Figure C.3: Test 5 Short Carbon 1 0.6Amps

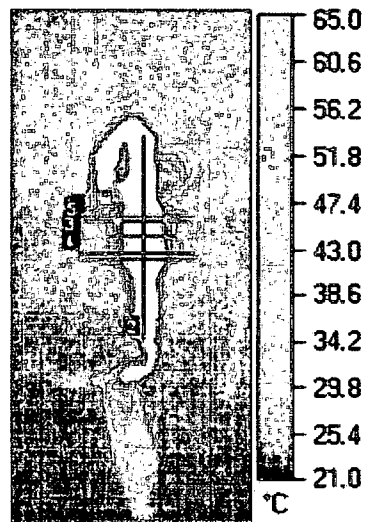


Figure C.4: Test 6 Short Carbon 1 0.7Amps

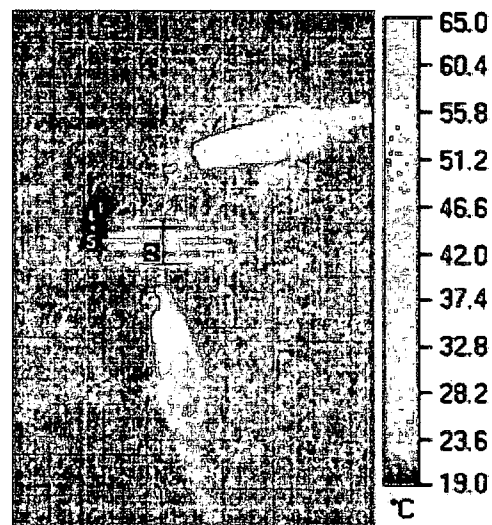


Figure C.5: Test1 SMA3 2Volts

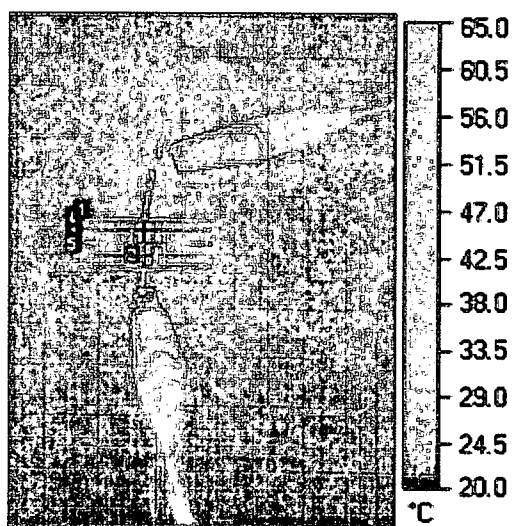


Figure C.6: Test1 SMA3 2.3Volts

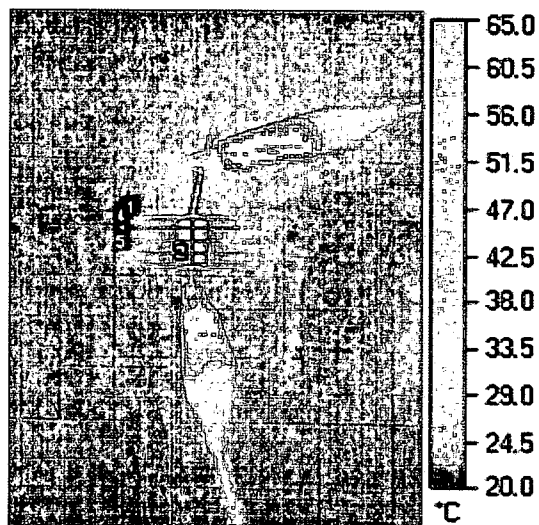


Figure C.7: Test1 SMA3 2.5Volts

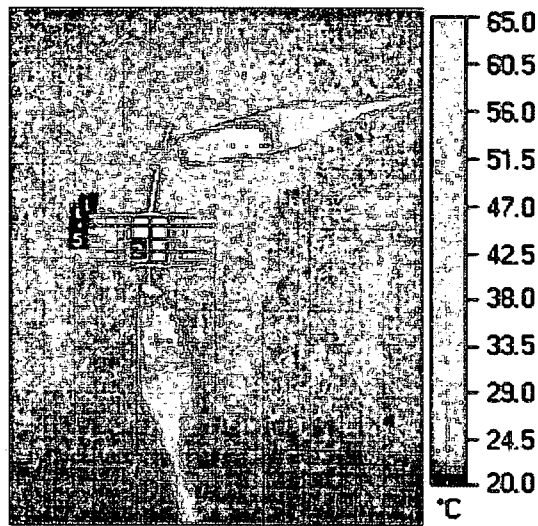


Figure C.8: Test1 SMA3 2.7Volts

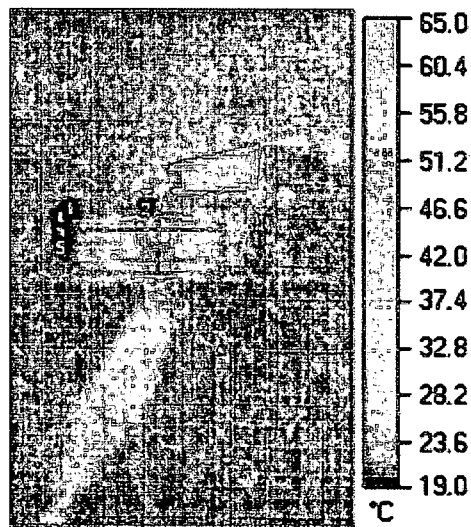


Figure C.9: Test1 Nichrome Specimen 2 2.0Volts

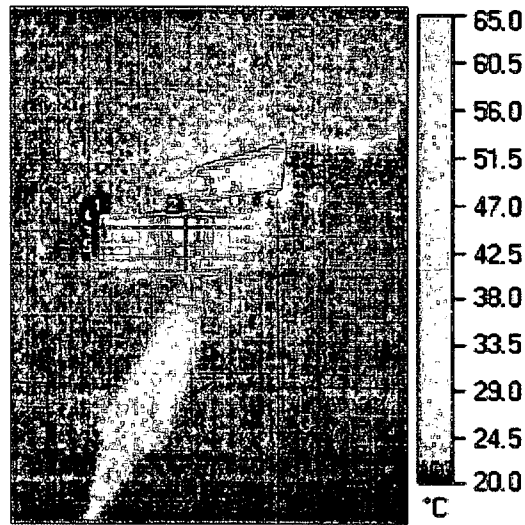


Figure C.10: Test3 Nichrome Specimen 2 2.3Volts

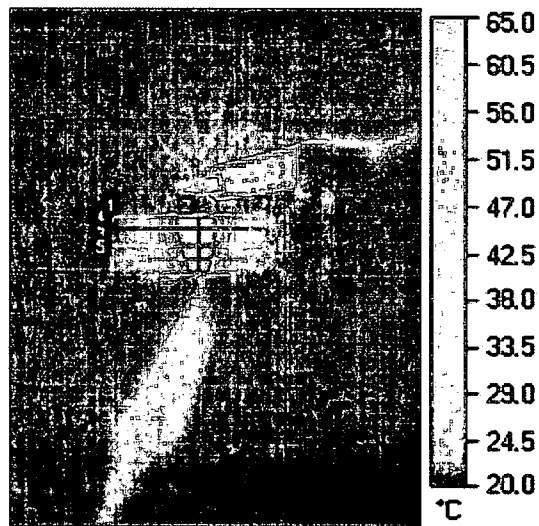


Figure C.11: Test2 Nichrome Specimen 2 2.5Volts

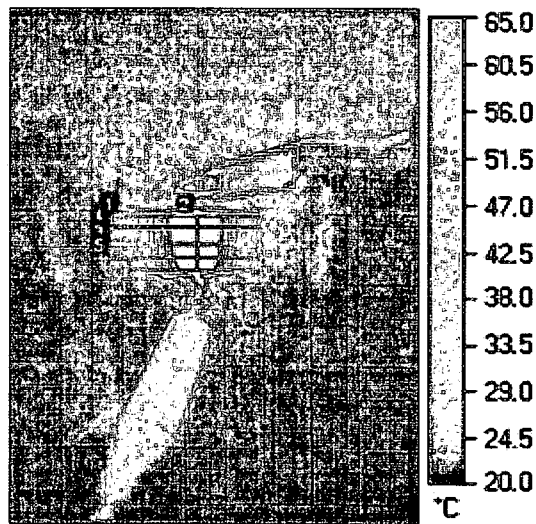


Figure C.12: Test4 Nichrome Specimen 2 2.7Volts

C.2 Time versus Temperature

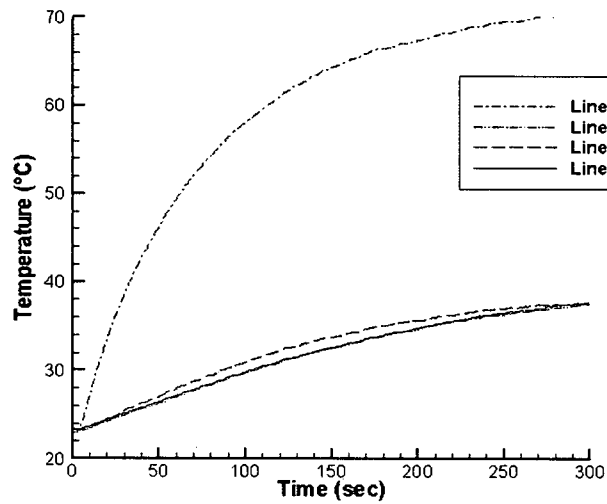


Figure C.13: Test 4 Short Carbon 1 0.4Amps Average Temperature Plot

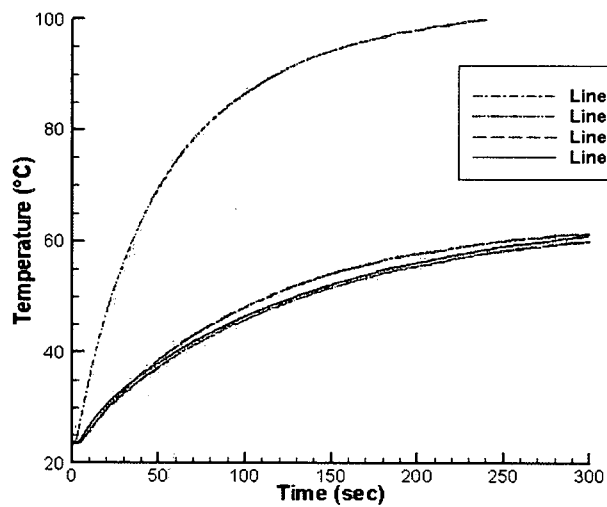


Figure C.14: Test 4 Short Carbon 1 0.4Amps Maximum Temperature Plot

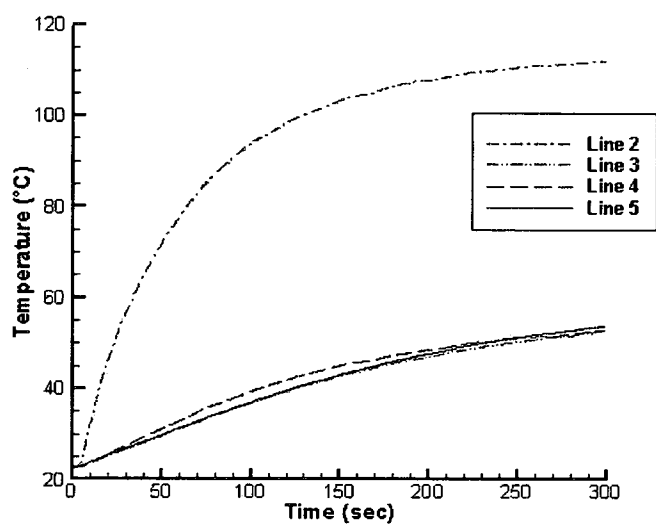


Figure C.15: Test 5 Short Carbon 1 0.6Amps Average Temperature Plot

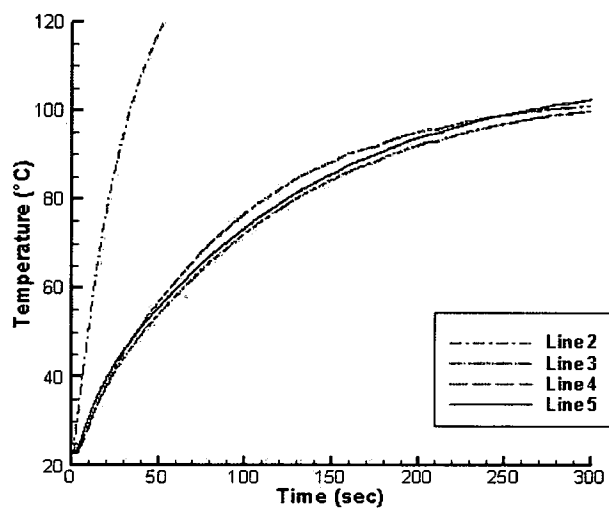


Figure C.16: Test 5 Short Carbon 1 0.6Amps Maximum Temperature Plot

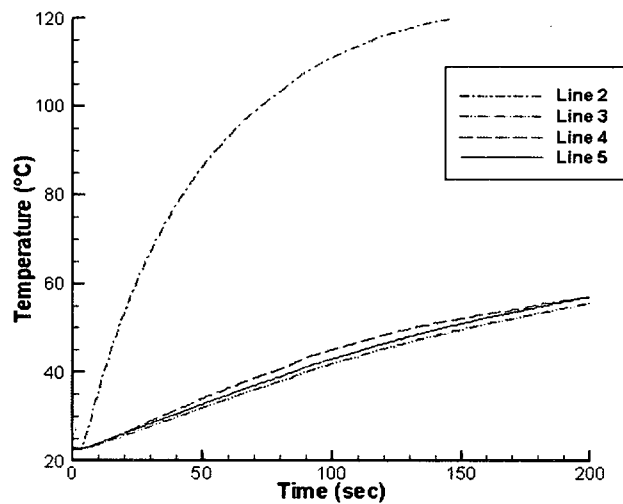


Figure C.17: Test 6 Short Carbon 1 0.7Amps Average Temperature Plot

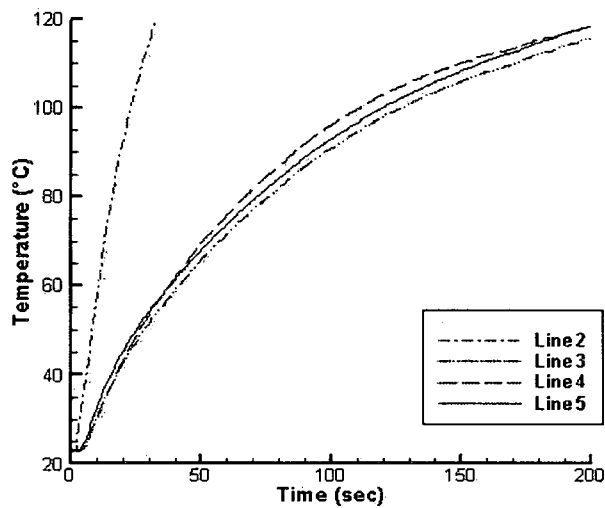


Figure C.18: Test 6 Short Carbon 1 0.7Amps Maximum Temperature Plot

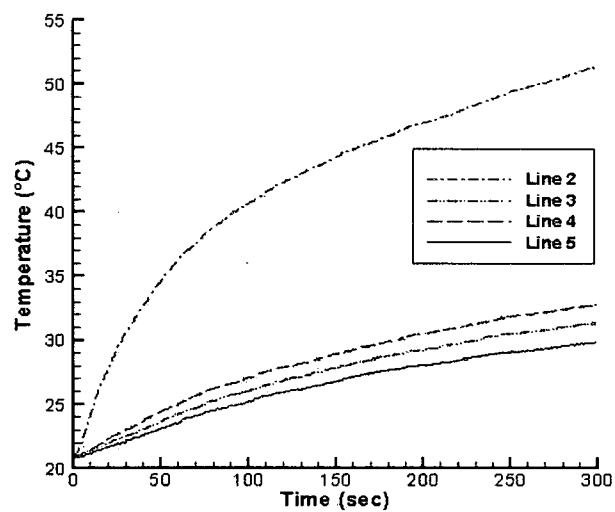


Figure C.19: Nichrome 2 2.0Volts Average Temperature Plot

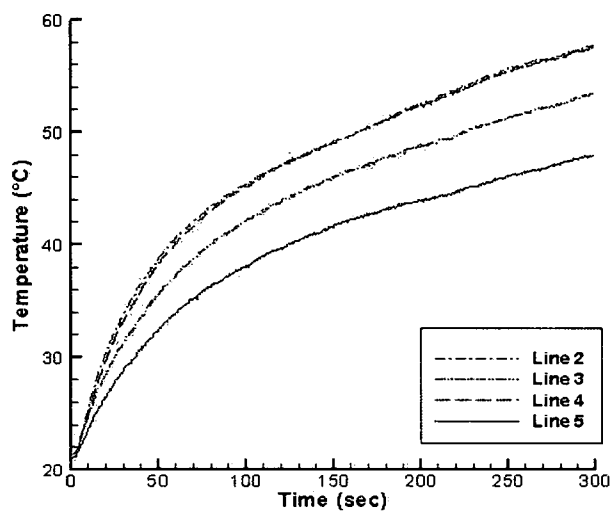


Figure C.20: Nichrome 2 2.0Volts Maximum Temperature Plot

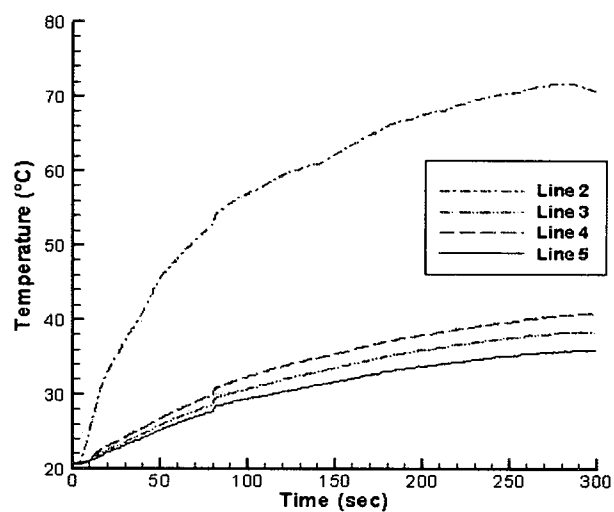


Figure C.21: Nichrome 2 2.3Volts Average Temperature Plot

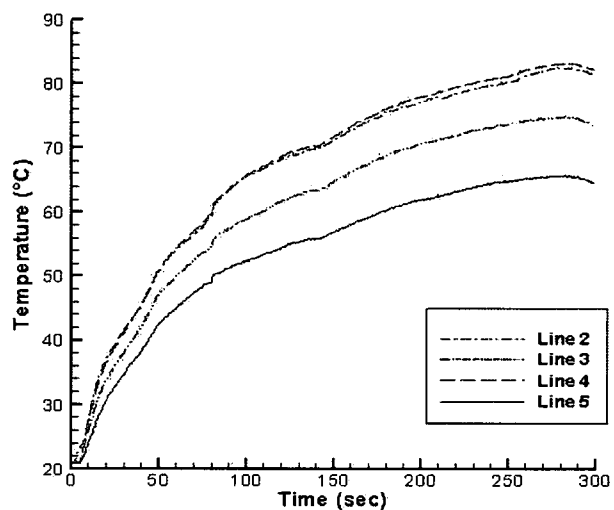


Figure C.22: Nichrome 2 2.3Volts Maximum Temperature Plot

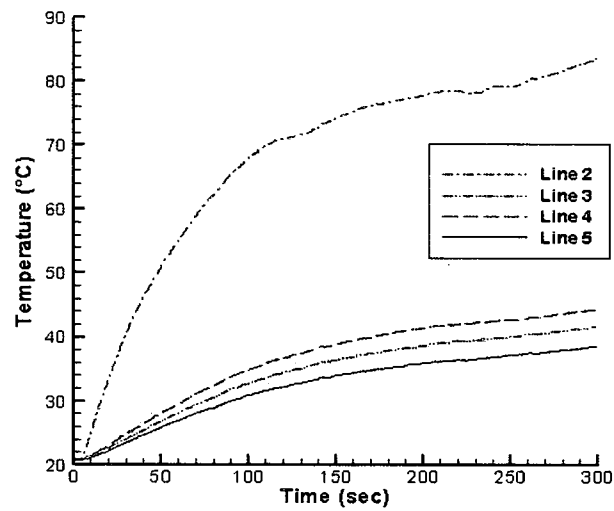


Figure C.23: Nichrome 2 2.5Volts Average Temperature Plot

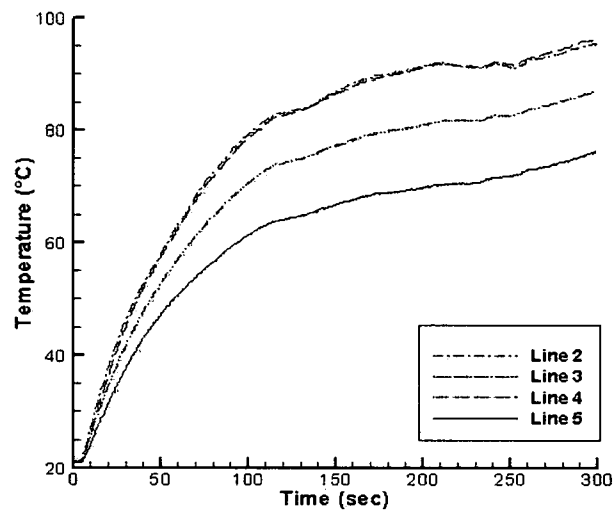


Figure C.24: Nichrome 2 2.5Volts Maximum Temperature Plot

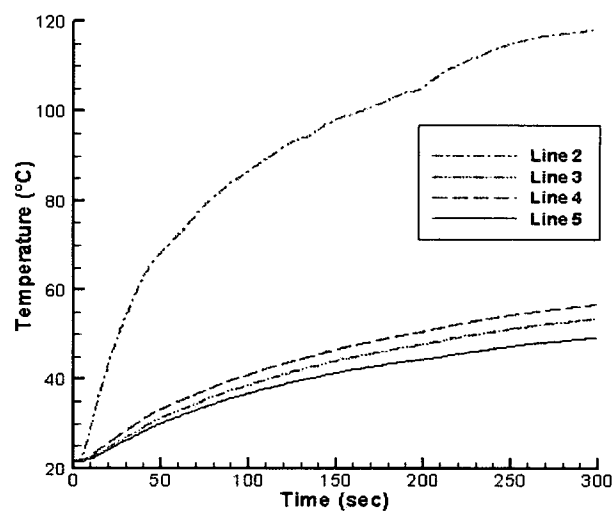


Figure C.25: Nichrome 2 2.7Volts Average Temperature Plot

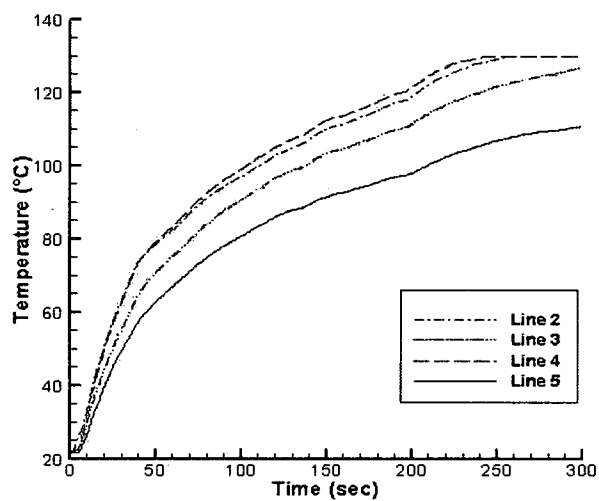


Figure C.26: Nichrome 2 2.7Volts Maximum Temperature Plot

C.3 Line Profile Plots

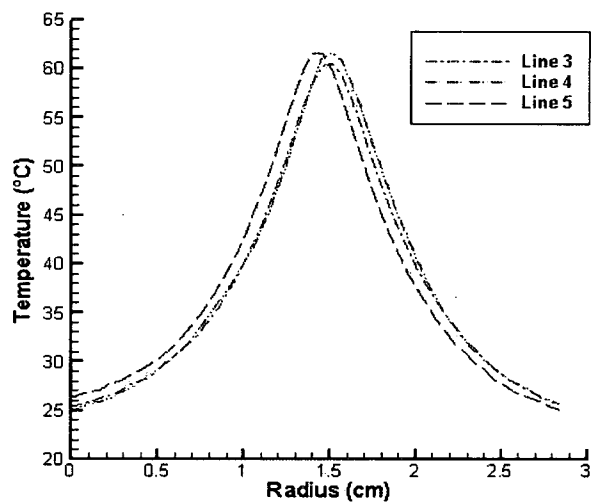


Figure C.27: Test 4 Short Carbon 1 0.4Amps Line Profile Plot

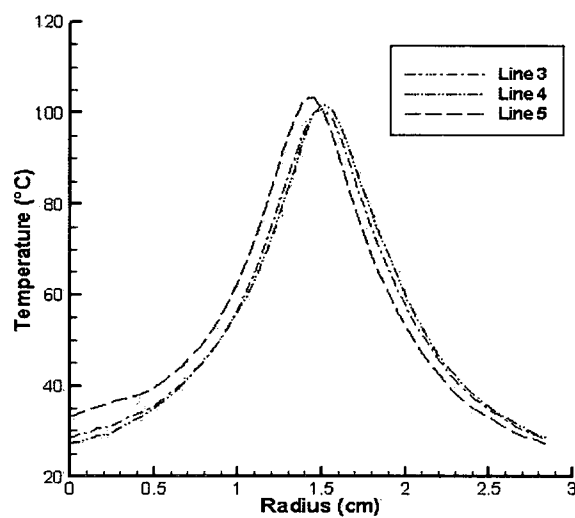


Figure C.28: Test 5 Short Carbon 1 0.6Amps Line Profile Plot

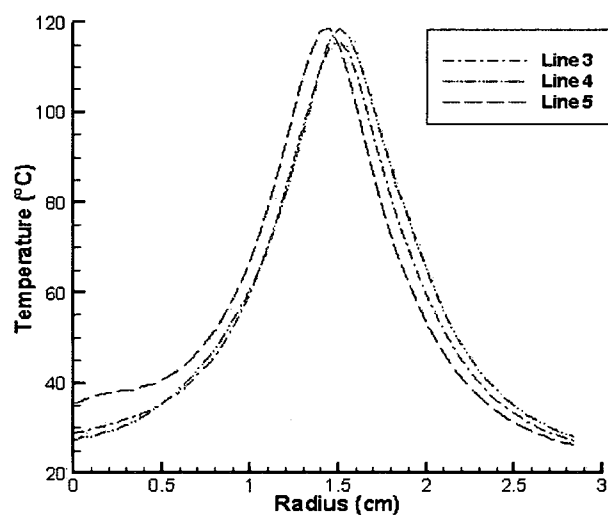


Figure C.29: Test 6 Short Carbon 1 0.7Amps Line Profile Plot

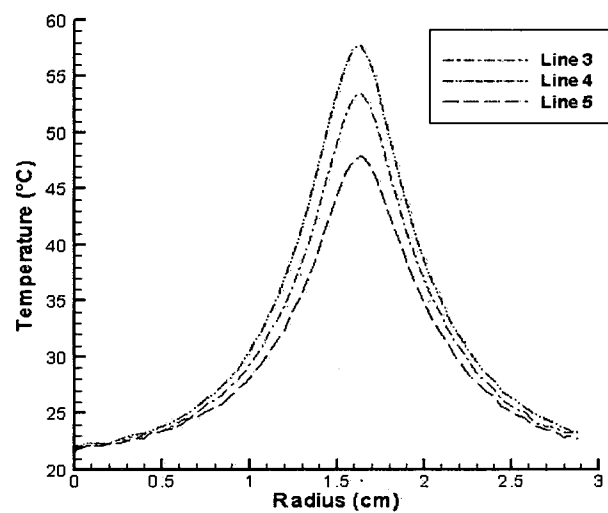


Figure C.30: Nichrome 2 2.0volts Line Profile Plot

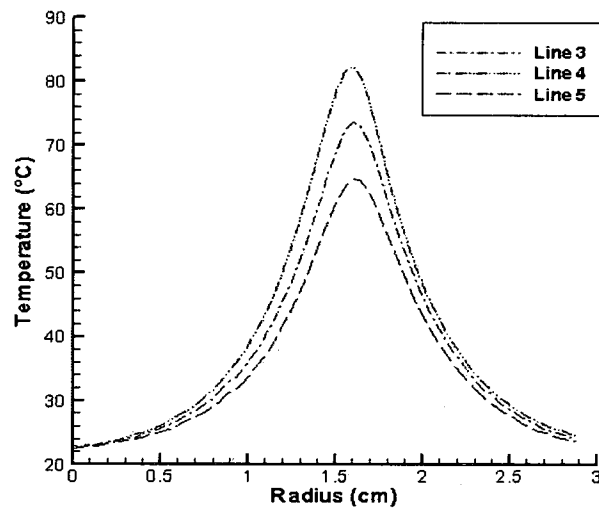


Figure C.31: Nichrome 2 2.3volts Line Profile Plot

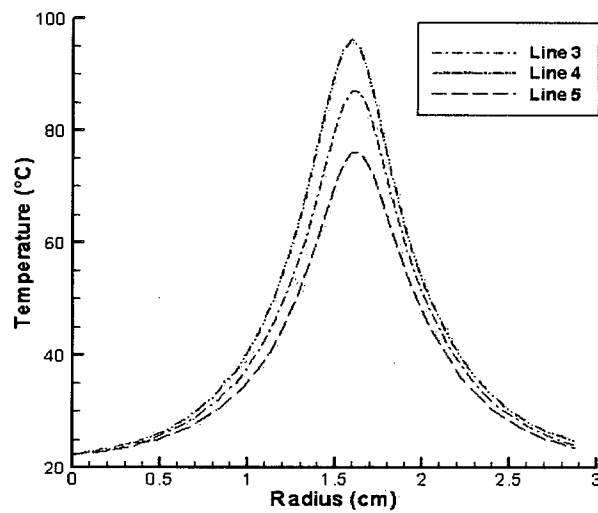


Figure C.32: Nichrome 2 2.5volts Line Profile Plot

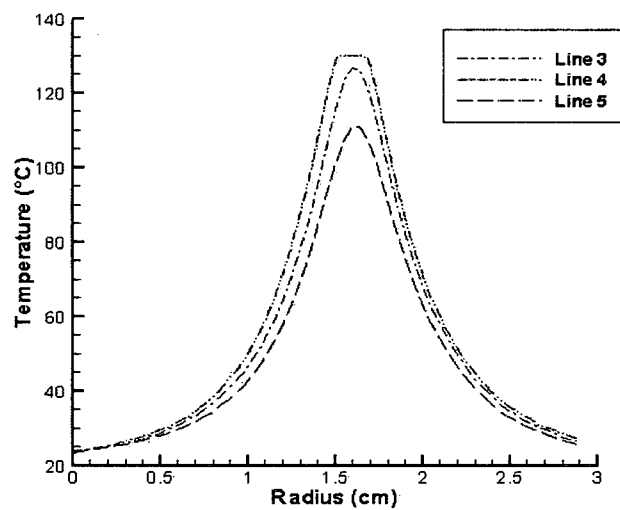


Figure C.33: Nichrome 2 2.7volts Line Profile Plot

Appendix D

Structural Skin Concept

D.1 In-Plane Stiffness Model Plots

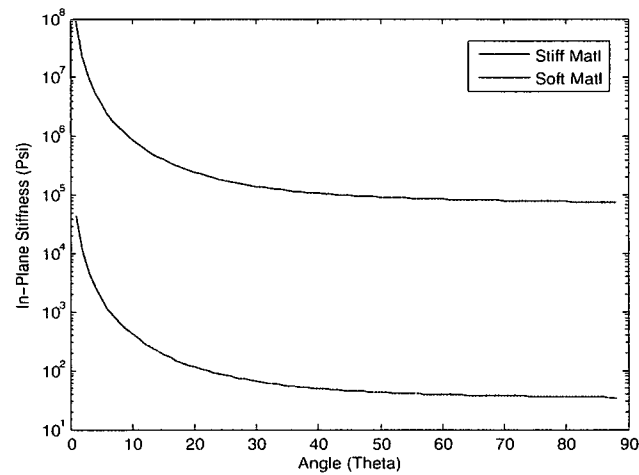


Figure D.1: Plot of the 1/4 hexagonal cell with 1/8 cell walls In-Plane Stiffness versus Cell Angle

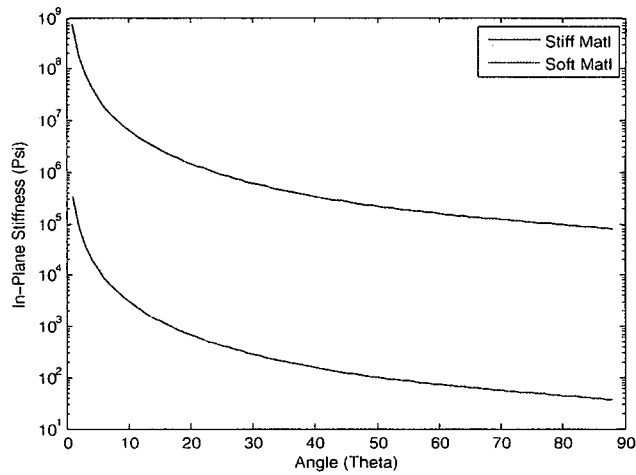


Figure D.2: Plot of the 1/4 hexagonal cell with 1/4 cell walls In-Plane Stiffness versus Cell Angle

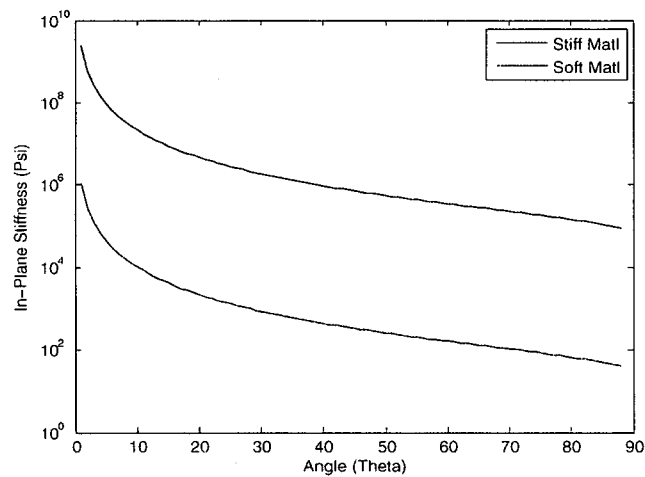


Figure D.3: Plot of the 1/4 hexagonal cell with 3/8 cell walls In-Plane Stiffness versus Cell Angle

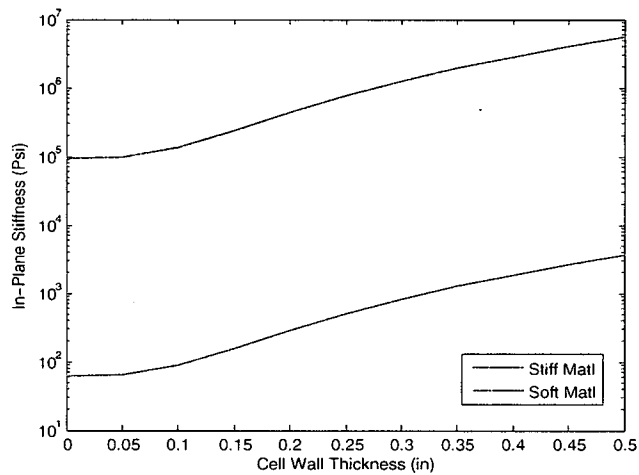


Figure D.4: Plot of the 1/4 hexagonal cell In-Plane Stiffness versus Cell Wall Thickness

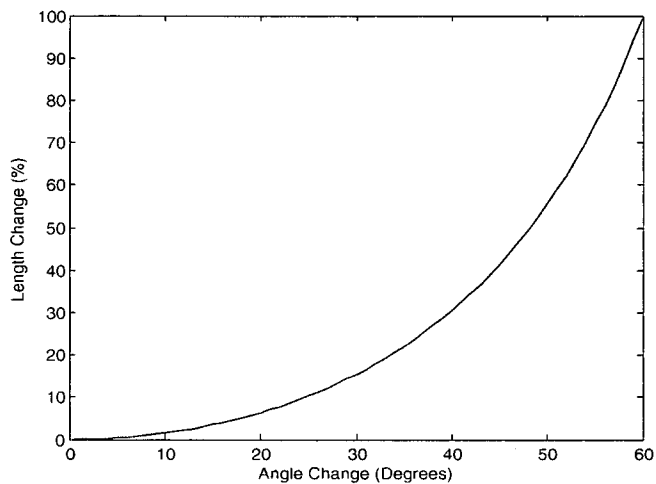


Figure D.5: Plot of the 1/4 hexagonal cell Length Change versus Cell Angle Change

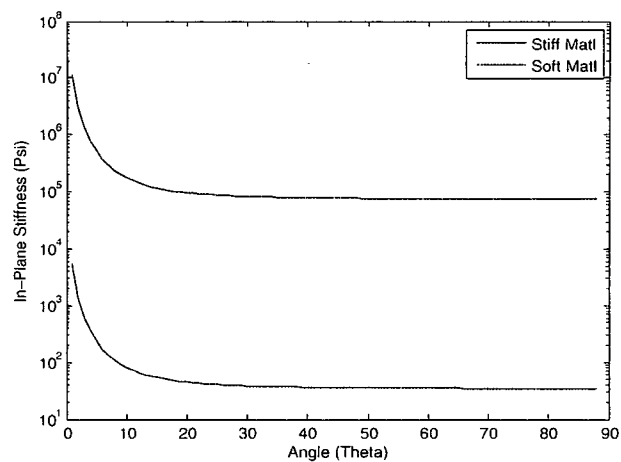


Figure D.6: Plot of the 1/2 hexagonal cell with 1/8 cell walls In-Plane Stiffness versus Cell Angle

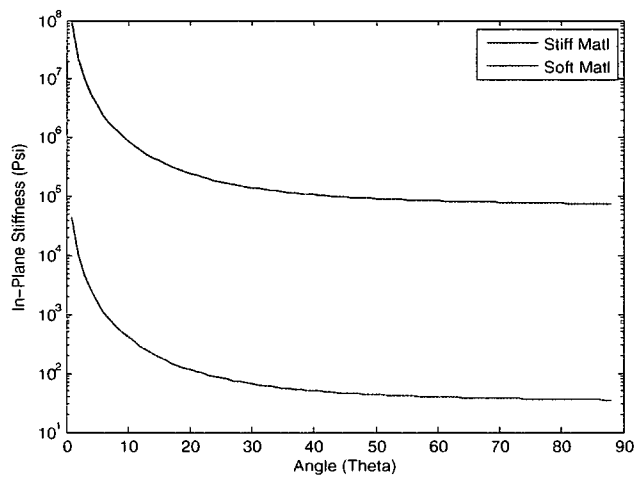


Figure D.7: Plot of the 1/2 hexagonal cell with 1/4 cell walls In-Plane Stiffness versus Cell Angle

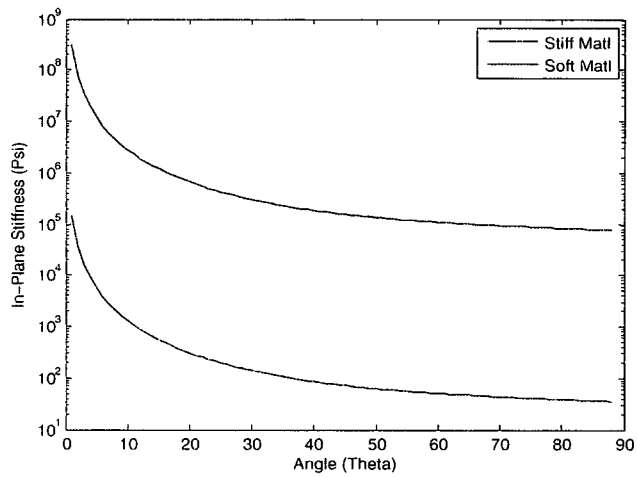


Figure D.8: Plot of the 1/2 hexagonal cell with 3/8 cell walls In-Plane Stiffness versus Cell Angle

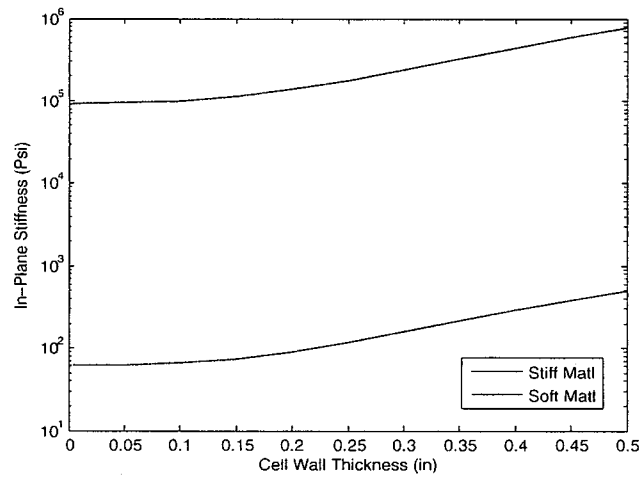


Figure D.9: Plot of the 1/2 hexagonal cell In-Plane Stiffness versus Cell Wall Thickness

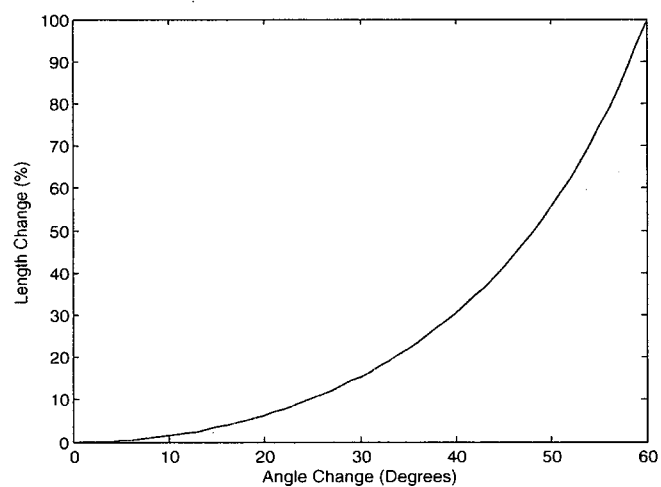


Figure D.10: Plot of the 1/2 hexagonal cell Length Change versus Cell Angle Change

D.2 Tensile Test Data

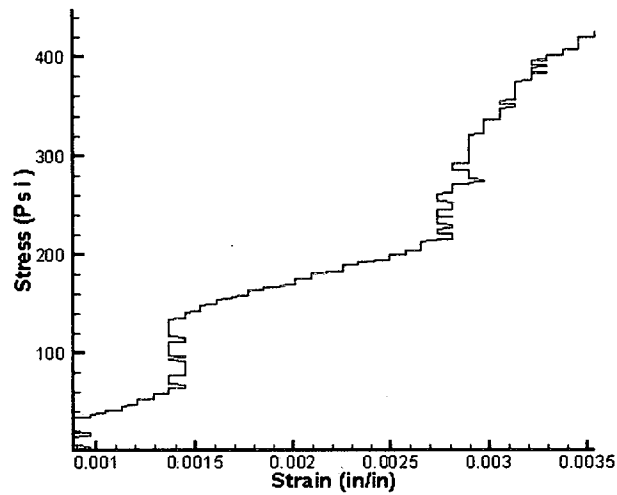


Figure D.11: Part 1 Stress versus Strain Plot of Neat Resin Test Specimen at Room Temperature

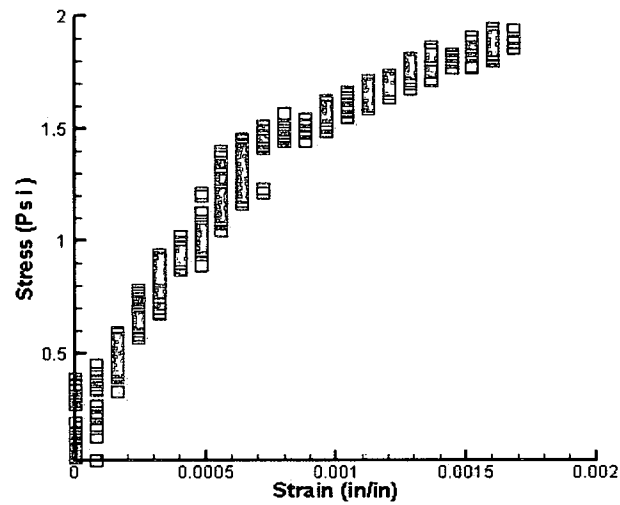


Figure D.12: Part 2 Stress versus Strain Plot of Neat Resin Test Specimen above Glass Transition Temperature

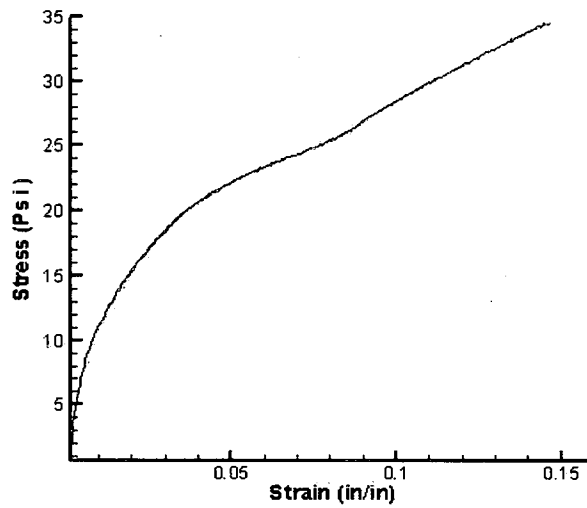


Figure D.13: Part 3 Stress versus Strain Plot of Neat Resin Test Specimen above Glass Transition Temperature

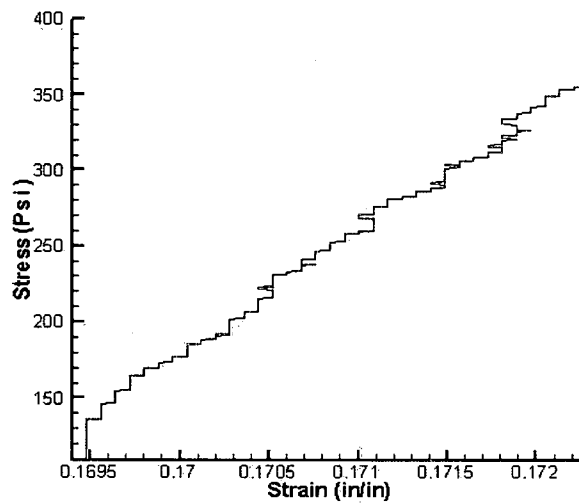


Figure D.14: Part 4 Stress versus Strain Plot of Neat Resin Test Specimen at Room Temperature

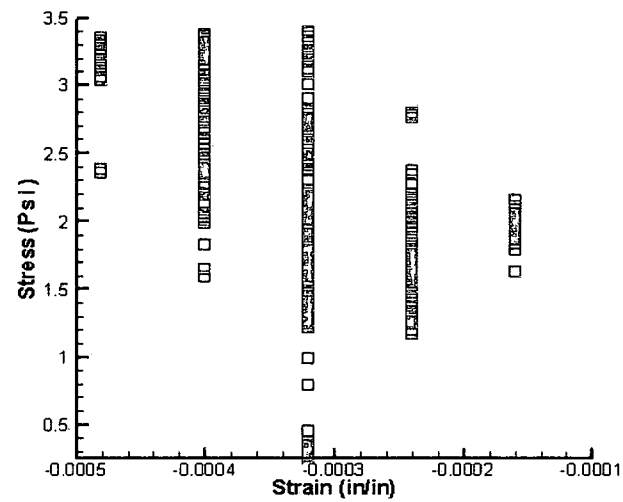


Figure D.15: Part 1 Stress versus Strain Plot of Carbon Fiber Test Specimen at Room Temperature

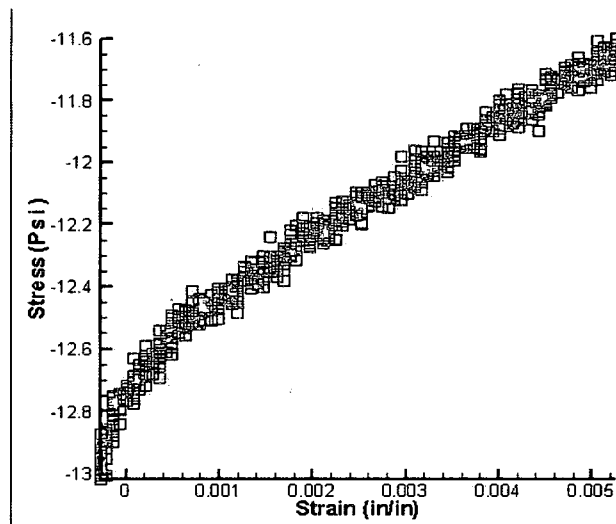


Figure D.16: Part 2 Stress versus Strain Plot of Carbon Fiber Test Specimen above Glass Transition Temperature

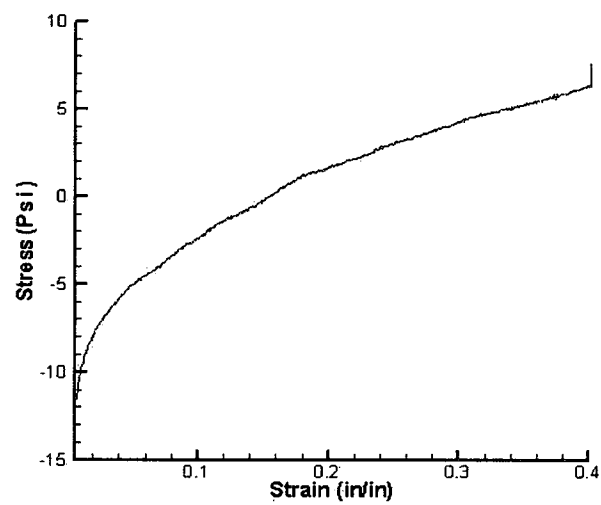


Figure D.17: Part 3 Stress versus Strain Plot of Carbon Fiber Test Specimen above Glass Transition Temperature

R002593101